2016

ULTRA-LOW POWER STRAINTRONIC NANOMAGNETIC COMPUTING WITH SAW WAVES: AN EXPERIMENTAL STUDY OF SAW INDUCED MAGNETIZATION SWITCHING AND PROPERTIES OF MAGNETIC NANOSTRUCTURES

Vimal G. Sampath
Virginia Commonwealth University

ULTRA–LOW POWER STRAINTRONIC NANOMAGNETIC COMPUTING WITH SAW WAVES: AN EXPERIMENTAL STUDY OF SAW INDUCED MAGNETIZATION SWITCHING AND PROPERTIES OF MAGNETIC NANOSTRUCTURES.

A Dissertation submitted in partial fulfillment of the requirements for the degree of Doctor of Philosophy in Engineering at Virginia Commonwealth University.

By

VIMAL GANAPATHY SAMPATH
Master of Technology in Aerospace Engineering, Indian Institute of Technology Kharagpur, India, 2011
Bachelor of Technology in Aerospace Engineering, Indian Institute of technology Kharagpur, India, 2010

Director: Jayasimha Atulasimha, Ph.D.
Qimonda Associate Professor, Department of Mechanical and Nuclear Engineering

Virginia Commonwealth University
Richmond, Virginia
December 2016

Acknowledgement

I would like to express my heartiest gratitude to my PhD. supervisor Prof. Jayasimha Atulasimha without whose continuous support I doubt that I would be writing this thesis. Spending all these years under his supervision, I have learnt a lot about conducting a fruitful research. His profound knowledge on Spintronics, surface acoustic waves and nanomagnetism has helped me to understand many complex research topics. I feel extremely privileged to get an opportunity to work under a scholar like him. I am also thankful to him not only to supervise me in my research projects but also in finding the right directions while evolving as a researcher. Without his invaluable help, precious comments, and careful guidance this journey of pursuing graduate study would not be so successful today. I would also like to express my gratitude to Prof. Supriyo Bandyopadhyay for being my co-advisor in all my research projects and for playing a highly significant role in both academic and professional development.

I am thankful to my peers who have been my companions during this endeavor and with whom I have worked and shared the ideas with, namely, Dhritiman Bhattacharya Md. Mamun Al-Rashid, Pallabi Sutradhar, Md. Iftekhar Hossain, Ayan Biswas. I want to particularly mention Dr. Noel D'Souza and Dr. Hasnain Ahmad who were kind enough to share their experimental knowledge with me. I would also like to show my gratitude to Prof. Gary M. Atkinson for being a committee member. Without his profound experience and insights in wafer processing technology, I wouldn't have been able to overcome important hurdles. I would also like to thank

Dr. Hooman V. Tafreshi and Dr. Arun Subramanian for being a part of my PhD committee and for their significant comments on my research project.

I also offer my thanks to the staffs of the Mechanical and Nuclear Engineering department, the Wright Virginia Microelectronics Center, and Dr. Dmitry Pestov in Nanomaterials Characterization Center who helped me train on the characterization equipment. , as well as Shopan Hafiz and Prof. Umit Ozgur for assisting with the initial operation of the pulse generator. I also acknowledge the use of the CNST facility at NIST, Gaithersburg, Maryland, USA for some of the nanofabrication work.

Last but definitely not the least I'd like to thank Dr. Dan Gopman from NIST Gaithersburg to agree to be on my committee and carry out important experiments related to FMR and help with his insights interpreting the data.

I would finally want to thank my mother, Ms. Usharani Sampath and my brother Shashi Sampath for their love, support and motivation towards achieving the success in both academic and personal lives.

Table of contents

List of Figures

List of Tables

Abstract

ULTRA–LOW POWER STRAINTRONIC NANOMAGNETIC COMPUTING WITH SAW WAVES: AN EXPERIMENTAL STUDY OF SAW INDUCED MAGNETIZATION SWITCHING AND PROPERTIES OF MAGNETIC NANOSTRUCTURES.

By Vimal Ganapathy Sampath

A Dissertation submitted in partial fulfillment of the requirements for the degree of Doctor of Philosophy in Engineering at Virginia Commonwealth University.

Virginia Commonwealth University, 2016

Director: Jayasimha Atulasimha, Ph.D.

Qimonda Associate Professor, Department of Mechanical and Nuclear Engineering

A recent International Technology Roadmap for Semiconductors (ITRS) report (2.0, 2015 edition) has shown that Moore's law is unlikely to hold beyond 2028. There is a need for alternate devices to replace CMOS based devices, if further miniaturization and high energy efficiency is desired. The goal of this dissertation is to experimentally demonstrate the feasibility of nanomagnetic memory and logic devices that can be clocked with acoustic waves in an extremely energy efficient manner. While clocking nanomagnetic logic by stressing the magnetostrictive layer of a multiferroic logic element with with an electric field applied across the piezoelectric layer is known to be an extremely energy-efficient clocking scheme, stressing every nanomagnet separately requires individual contacts to each one of them that would necessitate cumbersome lithography. On the other hand, if all nanomagnets are stressed simultaneously with a global

voltage, it will eliminate the need for individual contacts, but such a global clock makes the architecture non-pipelined (the next input bit cannot be written till the previous bit has completely propagated through the chain) and therefore, unacceptably slow and error prone. Use of global acoustic wave, that has *in-built granularity*, would offer the best of both worlds. As the crest and the trough propagate in space with a velocity, nanomagnets that find themselves at a crest are stressed in tension while those in the trough are compressed. All other magnets are relaxed (no stress). Thus, all magnets are *not* stressed simultaneously but are clocked in a sequentially manner, even though the clocking agent is global.

Finally, the acoustic wave energy is distributed over billions of nanomagnets it clocks, which results in an extremely small energy cost per bit per nanomagnet. In summary, acoustic clocking of nanomagnets can lead to extremely energy efficient nanomagnetic computing devices while also eliminating the need for complex lithography. The dissertation work focuses on the following two topics:

1. Acoustic Waves, generated by IDTs fabricated on a piezoelectric lithium niobate substrate, can be utilized to manipulate the magnetization states in elliptical Co nanomagnets. The magnetization switches from its initial single-domain state to a vortex state after SAW stress cycles propagate through the nanomagnets. The vortex states are stable and the magnetization remains in this state until it is 'reset' by an external magnetic field.

2. Acoustic Waves can also be utilized to induce 180^0 magnetization switching in dipole coupled elliptical Co nanomagnets. The magnetization switches from its initial single-domain 'up' state to a single-domain 'down' state after SAW tensile/compressive stress cycles propagate through the nanomagnets. The switched state is stable and non-volatile. These results show the effective implementation of a Boolean NOT gate.

Ultimately, the advantage of this technology is that it could also perform higher order information processing (not discussed here) while consuming extremely low power.

Finally, while we have demonstrated acoustically clocked nanomagnetic memory and logic schemes with Co nanomagnets, materials with higher magnetostriction (such as FeGa) may

ultimately improve the switching reliability of such devices. With this in mind we prepared and studied FeGa films using a ferromagnetic resonance (FMR) technique to extract properties of importance to magnetization dynamics in such materials that could have higher magneto elastic coupling than either Co or Ni.

Chapter 1: Introduction

1.1 Background

1.1.1 Moore's Law and scaling issues

Transistors were considered one of the most important inventions of the 20th century. There was a rapid increase in number of transistors per unit area, which was predicted by Moore's law which states that, "the numbers of transistors on integrated circuits (IC) would double in every two years."
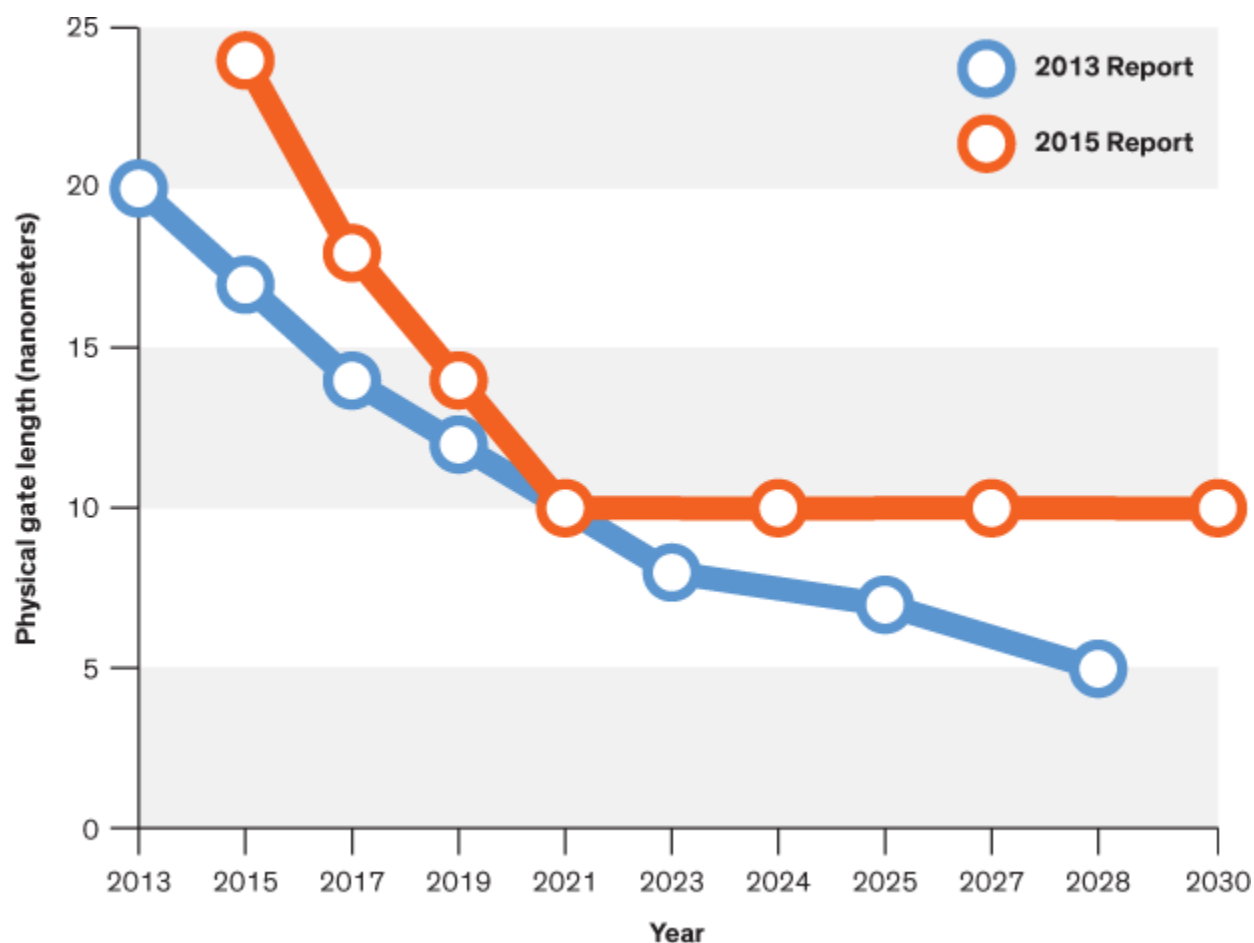
Fig. 1.1: ITRS had previously predicted that the physical gate length of transistors would shrink until at least 2028 (see blue line). The last ITRS report shows this feature size going flat in the coming years. [Image source: http://spectrum.ieee.org/semiconductors/devices/transistors-could-stop-shrinking-in-2021]

Scaling down of transistors meant faster operation, low energy dissipation and low cost of manufacturing. This scaling down of transistors in ICs today has led to gate lengths nearing 14 nm. However as predicted by the recent report on ITRS (Figure 1.1), further down scaling of Complementary Metal Oxide Semiconductors (CMOS) is severely challenged by high circuit power densities and energy dissipation of the basic switching element.

1.1.2 Need for replacing CMOS technology and specific applications

The apparent disadvantages that limit further scaling down of CMOS based IC technology is the strong motivation for developing alternate ultra-low power computing devices. Such extremely energy efficient computing devices can be potentially used in embedded applications such as medically implemented processors and distributed sensing/monitoring systems where energy is at a premium. As a result, the semiconductor industry is looking for new computing devices with unprecedented energy efficiency to replace the transistor. In order to realize such a device, researchers have been working on several novel device concepts and computational paradigms that are able to replace CMOS transistors (charge based devices) with other physical quantities such as spin (magnetism). One such device concept employs a bi-stable single domain nanomagnet whose magnetization orientation encodes a bit of information that can be manipulated to implement logic devices (Cowburn *et. al.*, 2000, Csaba *et. al.*, 2002). Due to the shape of the nanomagnet (as shown in Fig 1.2) the magnetizations favors the major axis, also known as easy axis. There is an energy penalty for the magnetization to align along the minor axis-also known as the hard axis. The shape of the nanomagnet prevents the magnetization from spontaneously switching between the two stable states along the major axis due to thermal noise. One of the two bi-stable   magnetization states (pointing up) can represent the bit "1" while the other

magnetization state (pointing down), can represent the bit "0". Such a nanomagnetic element is "non-volatile" as no power is required to store its logic state.

A detailed description of using various methods to switch nanomagnets starting with STT (Slonczewski, 1996) to the use of strain (Atulasimha and Bandyopadhyay, 2011; D'Souza N.., 2015) and acoustic waves (Biswas *et al.*, 2012; Sampath *et al.*, 2016) is discussed in section 1.3.3.

Bit 0   **Bit 1**
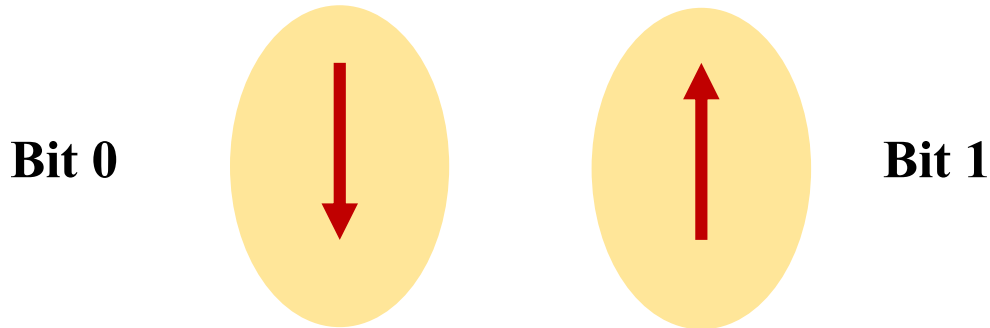
Fig. 1.2: Encoding bits in the magnetization of single domain nanomagnets.

1.2 Magnetic domains and nanomagnetism

This section gives an overview of magnetic materials (in particular ferromagnetic materials) and explains what leads to the formation of domains in magnetic micro and macro-scale materials.It then explains how nanomagnetic structures have a strong tendency to exhibit single domain behavior and how this can be exploited to encode a logic state or a bit of information.

1.2.1 Paramagnetic and ferromagnetic behavior: Role of exchange coupling

In some materials that have net magnetic moment, the moments locally tend to align with an applied magnetic field. Thus the magnetization produced in the material is proportional and is in the direction of the applied magnetic field. This is known as paramagnetism. In certain solids,

such as iron, nickel and cobalt, the moments in neighboring atoms are strongly coupled (due to exchange coupling) and tend to align with each other at room temperature. Thus, even in the absence of magnetic fields there is spontaneous magnetization in the material, this is typical of ferromagnetic materials. At sufficiently high temperature, the thermal energy exceeds the exchange coupling energy between spins and breaks this alignment, leading to a paramagnetic state. The temperature at which this transition from ferromagnetic to paramagnetic state or vice versa occurs is known as the Curie temperature (Chikazumi, 1964).

1.2.2 Domains in ferromagnetic materials: Illustrating the effects of exchange coupling energy, magnetocrystalline anisotropy energy and magnetostatic energy

It was left to Landau and Lifshitz in 1935 to show that the existence of domains is a consequence of energy minimization. A single domain specimen has associated with it a large magnetostatic energy, but the breakup of magnetism into localized regions (domains), providing for flux closure at the ends of the specimen, reduces magnetostatic energy. Providing that the decrease in magnetostatic energy is greater than the energy needed to form magnetic domain walls, then multi domain specimens will arise (Jiles, 2016).

Two scenarios can emerge (at zero applied field) depending on the magnitude of the magnetocrystalline anisotropy (this energy is minimized when the magnetization (spins) point along preferred crystallographic directions):

(i) <u>Closed flux path or vortex states (see Fig 1.3 a)</u>: The magnetic moments would prefer to arrange themselves to form a closed flux path as shown in Figure 1.3a. However, this pattern is energetically feasible only if the magnetocrystalline anisotropy is extremely low.

NOTE: The expense of exchange coupling is small in this case, as the difference in orientation between two neighboring moments is small. However, some moments would have to assume orientations which result in large magnetocrystalline anisotropy energy so this is possible only when the material has low magnetocrystalline anisotropy.

(ii) <u>Discrete domains that form a closed flux path (for example, see Fig 1.3b)</u>: For materials with cubic anisotropy this typically results in a domain pattern, such as the one seen in Figure 1.3b. The moments are oriented along the easy <100> directions leading to small magnetocrystalline anisotropy energy with some expense in exchange coupling energy at the domain boundaries.
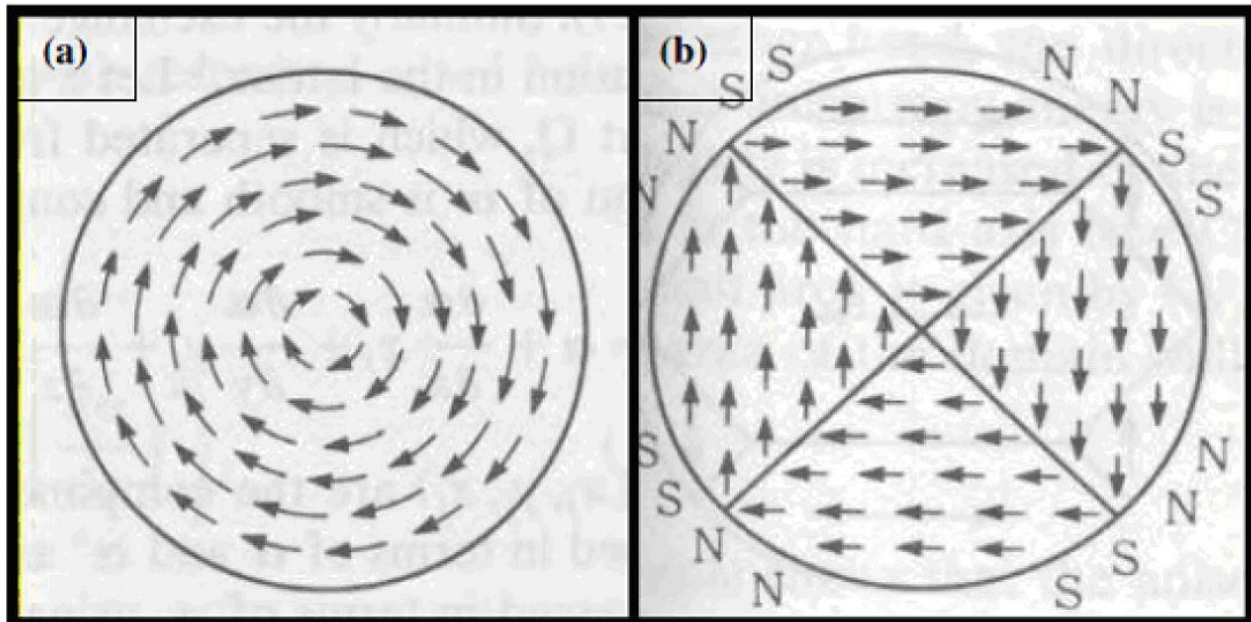
Fig. 1.3: Domain patterns in discs under different criterion. (a) Zero magnetocrystalline anisotropy. (b) Cubic magnetocrysalline anisotropy. (Chikazumi, 1964; Atulasimha, 2006) [Image source: Chikazumi, 1964]

1.3 Nanomagnetic Technology

It can be shown that the *minimum* energy dissipated in switching a transistor at a temperature T is $NkTln(1/p)$, where N is the number of information carriers (electrons) in the transistor, k is the Boltzmann constant, and p is the bit error probability. This is independent of the switching speed. While, the minimum energy dissipated to switch a *single domain* magnet's magnetization is $\sim kTln(1/p)$. This is because the *exchange interaction* between many spins makes all of them behave collectively like a giant single classical spin (Salahuddin and Datta, 2007; Atulasimha and Bandyopadhyay, 2010) and rotate together to switch the magnetization (Salahuddin and Datta, 2007). Thus, for the same number of information carriers in a transistor and in a single domain nanomagnet, for the same bit error probability, the ratio of the minimum energy dissipated to switch a magnet to that dissipated to switch a transistor will be $\sim 1/N \ll 1$. This energy advantage makes a nanomagnet intrinsically much more energy-efficient than the transistor as a logic switch. Note that it is the mutual interaction between spins (exchange interaction) gives the magnet this advantage. It's not an inherent advantage of spin over charge.

Thus, nanomagnet-based computing has two advantages over traditional transistor based electronics. The primary reasons are: (i) magnets are intrinsically more energy-efficient than transistors, and (ii) magnets suffer from no leakage and hence have no standby power dissipation in contrast to transistors that do have a lower leakage current in the "off" state.

Due to this inherent advantage, nanomagnet-based computing architectures are being increasingly researched, One such example is the magnetic quantum cellular automata (MQCA) scheme used to implement nanomagnetic logic (NML), where nanomagnets are placed in specific geometric patterns to construct Boolean logic gates, and the dipole interactions between the nanomagnets elicit the desired logic operations on the bits encoded in their magnetization orientations (Cowburn and Welland, 2000; Csaba *et al.*, 2002). The dipole interaction also acts as

an effective "wire" to link successive gates and thus build different combinational or sequential Boolean circuits. This methodology builds on the Single Spin Logic (SSL) paradigm in which exchange interaction between spins (up- and down-spin polarizations encode the two logic bits) is equivalent to the role of dipole interaction between magnets (Bandyopadhyay, Das and Miller, 1994). NML schemes can be very energy-efficient if the magnets are switched in a way that dissipates very little energy in the external switching circuit.

1.3.1 Clocking: Disadvantages

Despite all its inherent advantages over transistors dipole-coupled NML schemes also have a serious drawback that limits their applications. Since dipole interaction is perfectly bi directional, there is no "isolation" between the input and the output ports of the nanomagnetic switch, unlike in transistors. This lack of isolation hinders unidirectional propagation of logic bits from one stage to the next – a property that is required of all Boolean logic schemes. To overcome this seemingly difficult hurdle, unidirectionality must be imposed in time since it cannot be imposed in space. That requires sequential clocking of the nanomagnets (much like in bucket-brigade devices and charge coupled device shift registers) (Bandyopadhyay and Roychowdhury, 1996; Bandyopadhyay, Svizhenko and Stroscio, 2000). This can be accomplished with Bennett clocking (Bennett, 1982), which is implemented by forcibly rotating a shape-anisotropic nanomagnet's magnetization through ~90° from its easy axis (major axis, energetically favorable) to the hard axis (minor axis, energetically less favorable) prior to a bit propagating through it, as shown in Fig. 1.4.

OR

External magnetic field

(a)   (b)

Fig 1.4: Elliptical nanomagnets. (a) The magnetization shown in red tends to align along the major axis, which is energetically favorable.(b) Only on application of external magnetic field along the minor axis, the magnetization is forced to align along the minor axis.

One way of implementing Bennett clocking in traditional binary NML is to arrange shape anisotropic nanomagnets in a chain along their major axis as shown in Fig. 1.5. The ground state of the nanomagnet array will be "anti-ferromagnetic" whereby each nanomagnet's magnetization will align along the easy axis, but nearest neighbors will have anti-parallel magnetizations, representing a sequence of binary bits (0 1 0 1…) as shown in Fig. 1.5 (i). This anti- ferromagnetic ordering is a minimum energy configuration due to the dipole interaction between neighboring nanomagnets. To be able to propagate a bit, if we somehow 'write' a bit on the left most magnet (Fig. 1.5 (i)), that is if it's flipped by an external agent we want the rest of the magnets to follow suit and sequentially flip themselves in a domino- fashion. This doesn't happen as expected because once the first nanomagnet is flipped the second one finds itself in a 'frustrated' state. The left magnet's interaction makes it want to switch but on the other hand the right side magnet (3rd magnet) which is equally distanced wants it to remain in the current state. Therefore, this nanomagnet would not flip and the input bit cannot propagate any further (D'Souza, N., 2014).

8
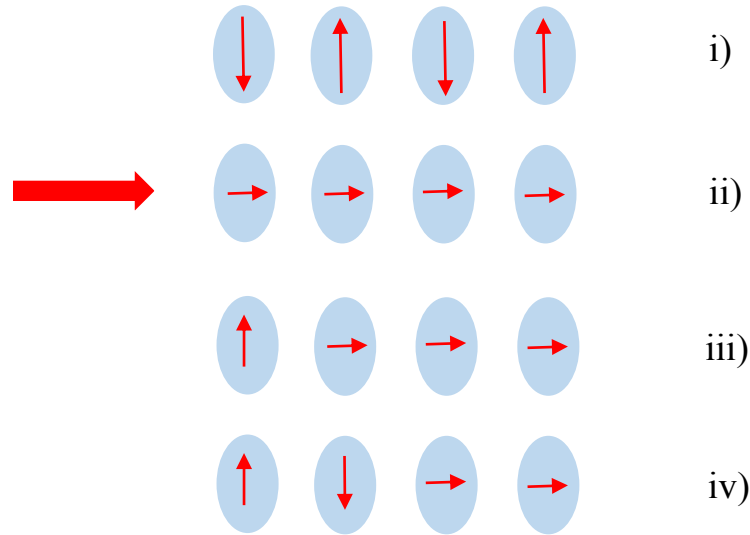
Fig. 1.5: Planar nanomagnets are arranged in a line with magnetization pointing along the in plane major axis (D'Souza, N. 2014).

1.3.2 Global clocking of nanomagnetic logic

In order to break a tie (explained in section 1.2.1) and propagate the input bit, a clock is needed (Bandyopadhyay, 2005a) . An example could be, prior to 'writing' the first bit, a global magnetic field could break the anti-ferromagnetic ordering and align every nanomagnet's magnetization along the common hard axis (Fig. 1.2 ii). This field is then withdrawn and the magnetization of the first nanomagnet is oriented by an external agent to conform to the input bit (Csaba *et al.*, 2002). Dipole interaction will then flip the magnetization of all the succeeding nanomagnets sequentially in a domino-like fashion since every nanomagnet now experiences non-zero dipole interaction that restores the anti-ferromagnetic order. This is an example of using global magnetic field as a clock and propagating bits using Bennett clocking. The same type of clock can propagate an input bit down a chain if the nanomagnets

are arranged in a line parallel to the easy axis as shown in Fig. 1.6. In this case, dipole coupling results in ferromagnetic ordering.
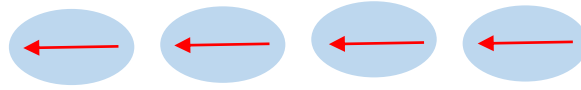
Fig 1.6: Nanomagnets arranged in a line along their easy axes, they couple ferro magnetically with the nearest neighbors having parallel magnetizations (D'Souza, N, 2014).

There is an inherent advantage to using global clock. There is no need to individually access the nanomagnets. Accessing individual nanomagnets require making electrical contacts to each one of them. These contacts will be in the sub 100 nm scale. Hence fabricating these contacts will lead to additional lithography and is undesirable. It also suffers from serious drawbacks. Since the bit is propagating from the left, the nanomagnets at the far end of a long chain are left in their unstable energy maxima state along the hard axes until the propagating bit reaches them. This could lead to them spontaneously relaxing to either of their two energy minima, which are along the major axis, before the bit reaches them. Even in one nanomagnet in the chain flips in this manner, it is error prone and renders the global clocking scheme unreliable. Secondly a bigger drawback is non-pipelined computing architecture. Pipelining refers to the ability to propagate a bit as the previous bit has propagated and not having to wait till the previous bit reaches the end of a chain of nanomagnets. This means that the propagating bit must travel through the entire chain before the global field can be applied again to reset the chain and prepare for the next bit to be propagated. This makes it unacceptably slow, compared to say a local clocking scheme where the next bit is ready to be propagated when the first bit leaves the first few nanomagnets in the chain, besides being error-prone (Bandyopadhyay and Cahay, 2009).

Attempts to alleviate pipelining issue by utilizing nanomagnets with biaxial anisotropy that have shallow energy minima at the minor axes have been reported in the literature (Carlton et al., 2008).

1.3.3 Local clocking of nanomagnetic logic

A better strategy to global clocking is to employ local clocking where the magnetization of every nanomagnet is reoriented, one at a time, along the hard axis via a local agent to implement Bennett clocking (Behin-Aein, Salahuddin and Datta, 2009). Although this increases the lithography overhead significantly since every nanomagnet needs to be contacted, it allows for pipelining of data, resulting in a faster access times (Bandyopadhyay and Cahay, 2009). Since pipelined and less error prone architectures are essential for Boolean logic, we will consider only the clocking schemes that have potential to be implemented locally. There have been a few such local clocking schemes explored recently. Some of them are illustrated below to describe their advantages and disadvantages and more importantly to evaluate which technique which might be the most promising method of rotating the magnetization of a nanomagnet from the easy to the hard axis, energy efficiently?

(a) A magnetic field generated by a current: In this approach, (Ney *et. al.*, 2003; Alam *et. al.*, 2010) a local magnetic field is generated by a current based on Ampere's law. The minimum magnetic field H_{min} required to flip a magnet is found by equating the magnetic energy in the field to the energy barrier E_b separating the two stable magnetization directions encoding the bits 0 and 1 in a shape-anisotropic nanomagnet. The energy barrier determines the equilibrium bit error probability. For reasonable static error rate (high

11

information retention time), it must be ensured that $E_b \geq 30kT$, which yields a Joule heating energy dissipation of about , 360 fJ, or 107-108kT.

(b) With a spin transfer torque delivered by a spin polarized current: Spin transfer torque is a method of switching a magnet by driving a spin-polarized current through it. The magnetization flips in the direction of spin polarization because of angular momentum transfer (Slonczewski, 1996; Ralph and Stiles, 2008). This method dissipates about $10^8 kT$ of energy to switch a single-domain nanomagnet in ~ 1 ns, even when the energy barrier within the magnet is only ~ 30 kT (Atulasimha and Bandyopadhyay, 2010). Additionally, spin currents are usually generated by current through magnetic tunnel junctions (MTJs) that have superior spin-torque efficiency but also suffer from operational reliability issues, especially in large scale memories (D'Souza, 2014).

(c) With a spin transfer torque delivered by a Spin hall effect in a heavy metal underlayer: An alternate method of generating spin-polarized current in nonmagnetic materials is by the Spin Hall Effect (SHE) (Dyakonov and Perel, 1971). Here, spin-orbit coupling causes electrons with different spins to deflect in opposite directions, resulting in a net flow of spin (spin current) which is perpendicular to the charge current that created it. This effect can be used, for instance to convert electric signals into a pure spin signal and converted back to electric signals after being transmitted through an insulating magnet as spin waves (Kajiwara et al., 2010). Other experiments have been carried out to using SHE to produce spin torques to rotate and switch the magnetic moments of perpendicularly polarized CoFeB films (Liu *et al.*, 2012) and CoFeB nanomagnets (Bhowmik, You and Salahuddin, 2014).

(d) With domain wall motion induced by a spin polarized current: In this method, a magnet is switched by inducing domain wall motion (M. Yamanouchi, D. Chiba et. al. 2004). The switching of a multi-domain nanomagnet may be possible in ~2 ns while dissipating 10^4 kT– 10^5 kT of energy (H. Tanigawa, S. Fukami et al. 2009).

Another application is a Racetrack memory (Parkin *et al.*, 2008) that uses a spin-coherent electric current to move magnetic domains along a nanoscopic permalloy wire about 200 nm across and 100 nm thick. As current is passed through the wire, the domains pass by magnetic read/write heads positioned near the wire, which alter the domains to record patterns of bits. A racetrack memory device is made up of many such wires and read/write elements.

However, these are still 2-3 orders of magnitude more dissipative than what has been shown to be achievable with "straintronics", where a multiferroic nanomagnet is switched with mechanical strain generated by a tiny voltage (Fashami, M.S. *et. al.*, 2011).

1.3.4 Strain based switching of nanomagnetic logic

Recently a scheme was proposed (Atulasimha and Bandyopadhyay, 2010) where electrically generated mechanical strain rotates the magnetization of a magnetostrictive layer. This is an extremely energy-efficient strategy for local Bennett clocking of NML since it can be implemented by applying a small voltage to a multiferroic nanomagnet consisting of two elastically coupled piezoelectric and magnetostrictive layers (Fig. 1.7) (Eerenstein, Mathur and Scott, 2006). The applied voltage generates strain in the piezoelectric layer which is transferred almost entirely to the magnetostrictive layer by elastic coupling if the top layer is much thinner than the bottom piezoelectric (Atulasimha and Bandyopadhyay, 2010).

This strain/stress can cause the magnetization of the magnetostrictive layer to rotate by a large angle and has been demonstrated in recent experiments (Brintlinger *et al.*, 2010; Hockel *et al.*, 2012; Dusch *et al.*, 2013; Chu *et al.*, 2008), although not in single-domain nanomagnets. Voltage-controlled switching of the magnetization vector by ~90° was also theoretically demonstrated to be feasible in ferromagnetic multilayers and spin valves mechanically coupled to a ferroelectric substrate, with one of the ferromagnetic layers possessing a small degree of cubic magnetocrystalline anisotropy (Pertsev and Kohlstedt, 2010).
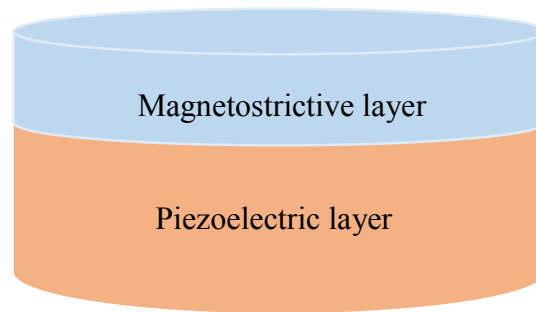
Fig. 1.7: A two-phase multiferroic nanomagnet composed of a magnetostrictive layer and a piezoelectric layer.

These rotations are sufficiently large to fulfill the requirements of Bennett clocking in logic chains (Atulasimha and Bandyopadhyay, 2010; Salehi Fashami, Atulasimha and Bandyopadhyay, 2012). This particular scheme is known as "hybrid straintronics" since the application of mechanical strain, generated by a tiny voltage, induces a magnetization rotation. Normally, strain can rotate the magnetization of an isolated magnet by up to ~90° because it moves the energy minimum of the magnet from the easy to the hard axis. This is sufficient to implement Bennett clocking. Recently it was shown that if the strain is withdrawn at the right juncture, as soon as the 90° rotation has been completed, the magnetization will continue to rotate and will end up rotating by 180° (Roy, Bandyopadhyay and Atulasimha, 2012). This will result in a complete bit flip. One

could also use a two electrode pair scheme (Biswas, Atulasimha and Bandyopadhyay, 2014) to implement a strain switched nanomagnetic memory scheme where the magnetization rotates by 180º

In the studies conducted by Atulasimha and Bandyopadhyay (2010), Bennett clocking of 2-state logic chains was considered where the logic switches are ellipsoidal multiferroic nanomagnets with the dimensions of the major axis = 105 nm and that of the minor axis = 95 nm. The piezoelectric layer, Lead Zirconium Titanate(PZT), of the multiferroic was 40 nm thick and the magnetostrictive layer, an alloy of Terbium, Dysprosium and Iron ($Tb_{0.3} Dy_{0.7} Fe_2$) popularly known as Terfenol-D), was 6 nm thick. Fig. 1.8 (a) illustrates the Bennett clocking scheme that was implemented by applying tiny rectangular voltage pulses of amplitude ~15 mV across the piezoelectric layer of the multiferroic generating a strain which, in turn, caused a magnetization rotation of ~90° in the magnetostrictive layer (Salehi Fashami et al., 2011). Transient simulations showed that for a pulse period of ~1 ns, the total energy dissipated in the clocking circuitry and in a nanomagnet is ~200 kT per rotation at room temperature (Roy, Bandyopadhyay and Atulasimha, 2011b; Salehi Fashami et al., 2011).

(a)   **(b)**
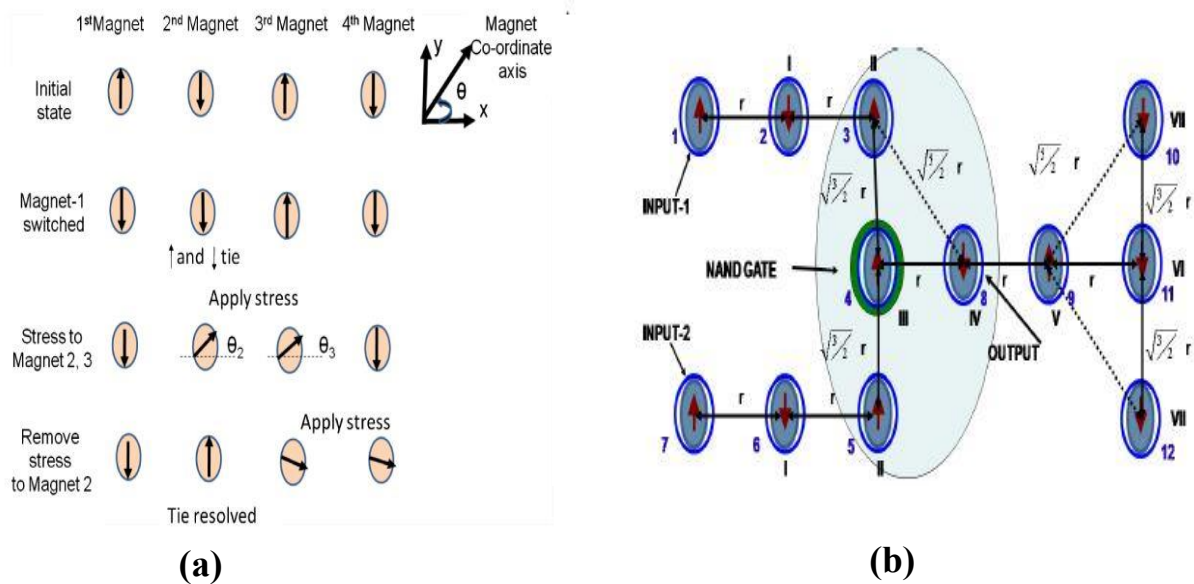
Fig 1.8: Local clocking scheme (a) Bennet clocking of NML (Salehi Fashami et al., 2011) (b) NAND Gate (Salehi Fashami, Atulasimha and Bandyopadhyay, 2012)

Thermal noise wasn't taken into account in these simulations since it doesn't have much effect. Dipole coupling between such Bennett clocked nanomagnetic switches was also shown to propagate information unidirectionally along a chain while dissipating a few 100 *kT/bit* at ~1 GHz clock rate (Salehi Fashami *et. al.*, 2011). Finally, simulations of a dipole-coupled NML NAND gate with multiferroic nanomagnets were performed (with fan-in and fan-out) and demonstrated a total energy dissipation of only ~1000 kT per NAND operation (Salehi Fashami, Atulasimha and Bandyopadhyay, 2012). This makes multiferroic nanomagnets one of the most energy efficient digital switches, and the hybrid spintronic/straintronic scheme one of the least dissipative memory and logic paradigms existent.

1.4 SAW based clocking: Memory and Logic

As discussed earlier, strain can be generated in a two-phase multiferroic nanomagnet by direct application of a voltage (or electric field) across a piezoelectric under layer using contact pads. However, this would be lithographically challenging in an array of nanomagnets of feature size ~100 nm and pitch 300-500 nm as it would require individual contact pads around each nanomagnet. A global electric field can be used to stress all magnets simultaneously, but the drawbacks of a global clocking scheme have already been discussed in detail to. First, the voltage generated by the field will be very large (resulting in large energy dissipation), and second, this precludes addressing individual nanomagnets selectively. This leads to a slow and non-pipelined architecture. Alternatively, a Surface Acoustic Wave (SAW) can be used to stress an array of nanomagnets sequentially as the wave propagates along the array. SAW leads to cycles of compression and rarefactions along the surface of the substrate. It leads to compressional and tensile stress at a point on the substrate as SAW propagates. This has the advantage of allowing

sequential stressing (writing bits one at a time in a pipelined manner provided the SAW velocities are sufficiently small) as opposed to simultaneous stressing. More importantly, this reduces the energy dissipation, calculated over individual nanomagnet, dramatically. Since there is also no need for lithographic contacts to individual nanomagnets (Atulasimha and Bandyopadhyay, 2010), this technique is superior to other local Bennett clocking schemes.

1.4.1 Principle

Consider the scheme depicted in Fig 1.6. In this case, a global surface acoustic wave (SAW) is passed underneath a large number of magnets usually delineated on the top of a piezoelectric substrate (LiNbO3). SAW generates a strain pulse on the surface of LiNbO3 substrate. The easy axis of the single domain nanomagnet that encodes the logic bit ("0" and "1"- with magnetization "down" and "up" respectively) is perpendicular to the direction of propagation of the longitudinal wave. This planar surface acoustic wave is generated by a piezoelectric strip at one end of the substrate. This wave produces a tension and compression cycle in the magnetostrictive nanomagnet deposited on the substrate as it propagates along it. The stress direction is perpendicular to the easy axis (along the in-plane hard axis). Therefore, during the tensile cycle, the stress anisotropy generated in a material with negative magnetostriction rotates the magnetization by 90º towards the hard axis because that is the minimum energy orientation. Both Ni and Co (Bozorth, 1993; Lee, 1955) possess negative values of magnetostrictive constant, implying that a tensile stress raises the energy barrier along the axis of applied stress while lowering the energy barrier along the axis perpendicular to this direction. This causes the magnetization to reorient itself perpendicular to the axis of tensile stress application. A compressive stress, on the other hand, causes the magnetization orientation to favor alignment

along the axis of stress application. Since Terfenol-D has positive magnetostriction, it experiences the exact opposite behavior. During the compressive cycle, the magnetization remains oriented along the easy axis since that becomes the minimum energy orientation. This principle is the basis of our clocking strategy.
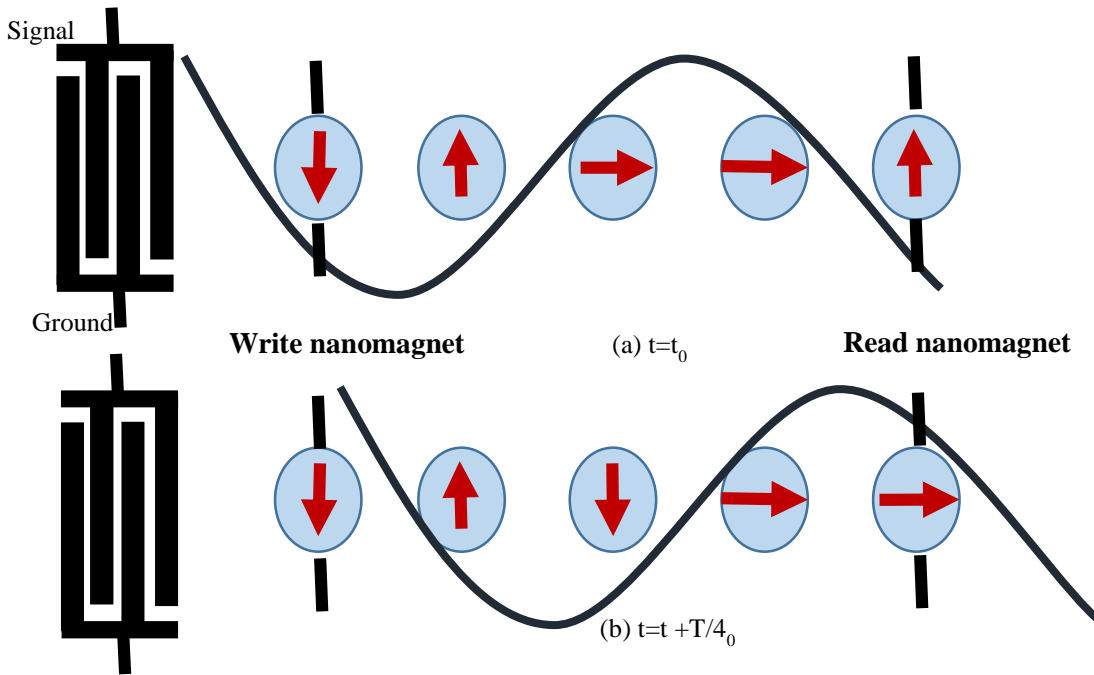
Fig. 1.9: MQCA wire consisting of 5 nanomagnets clocked by acoustic waves. The lithographic contacts are not needed for the intermediate magnets between write magnet and read magnet.

For example, when the wave-front that had clocked (rotated the magnetization of the nanomagnets 3 and 4 in Fig 1.9 (a) has moved the distance of one nanomagnet, the 3rd nanomagnet relaxes to a state under the influence of the dipole coupling of the first (Fig 1.9 b), implementing Bennett clocking. Immediately, a new input bit can be received by nanomagnet-2 that propagates along with the next acoustic pulse. Thus, the input bit train can follow the wave front and propagate unidirectionally while also being pipelined. The nanomagnets which propagate the bit do not need

individual lithographic contacts, for local clocking. In the current scheme of 5 nanomagnets in Fig. 1.9, the middle three nanomagnets do not require any kind of lithographic contacts. This computing architecture is therefore fast (large throughput), but unlike normal pipelined architecture, does not require a contact for every nanomagnet.

It should be noted here that in Fig. 1.9 the black lithographically deposited wires depicted as connectors to the 'write' and 'read' nanomagnets are only indicative of the possible lithographic contacts needed. In reality, these nanomagnets could be contacted by wires perpendicular to the plane of the nanomagnets, which could then be used to write by spin transfer torque current. Or there could be a four pad mechanism (Biswas, Bandyopadhyay and Atulasimha, 2014), which has to be created lithographically, to write a bit.

1.4.2 SAW Memory scheme

A nanomagnet with two stable states can encode bits "1" and "0". As shown in Fig. 1.10, we experimentally demonstrate SAW-based magnetization switching from single domain to a stable vortex state in isolated nanoscale elliptical cobalt nanomagnets that are not dipole coupled to any other nanomagnet. "Vortex" state is formed when magnetizations curl around the center with orientation in the surface plane (Fig. 1.10b). It has a distinct quadrant image, of alternate light and dark, on a Magnetic Force Microscopy image (MFM image). The nanomagnet's magnetization, which is a single domain in the pre-stress state, goes into a vortex state upon application of the SAW, and *remains* in the "vortex" state even after the SAW has propagated through and there is no longer any strain in the nanomagnets. The vortex state is therefore *non-volatile*. Both the pre SAW state and the Vortex state are non-volatile stable states.
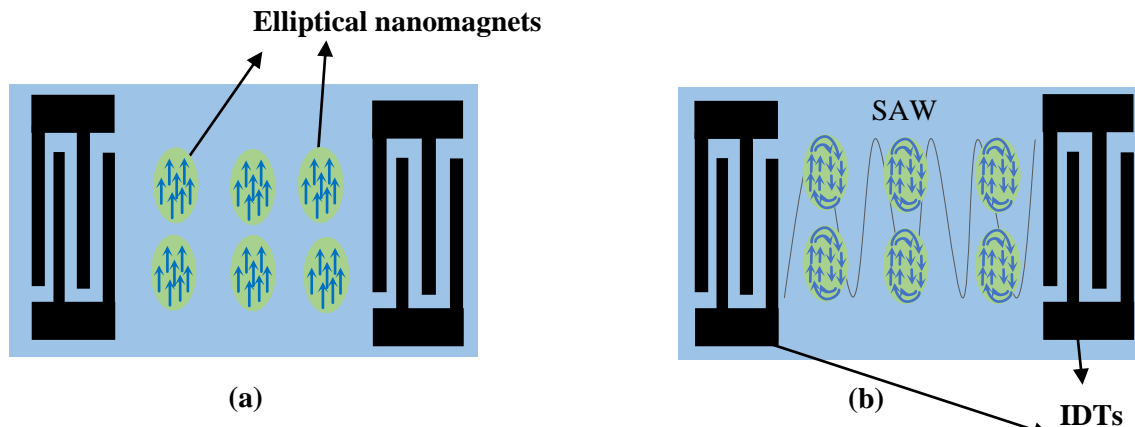
Fig. 1.10: SAW memory scheme (a) Schematic of isolated nanomagnets with their magnetization pointing up before SAW (b) The magnetizations go into a nonvolatile vortex state after SAW.

As the SAW propagates in the delay line it generates cyclic mechanical strain on the piezoelectric substrate. Each nanomagnet that is delineated on the piezoelectric substrate, experiences cycles of tensile and compressive stress along its major axis corresponding to the crest and trough of the SAW. Multiple cycles of SAW pass through the nanomagnet, not just a single pulse. Also since the wavelength of the acoustic wave that generates the cyclic stress is much larger than the dimensions of the nanomagnets, at any given instant the stress experienced by each nanomagnet is fairly uniform across its dimension.

The scheme shown and explained above may not directly translate to a practical memory scheme by itself. However, it is a proof of concept and a forerunner to different memory schemes, a couple of which are described below.

SAW Interference scheme: One such scheme could be using the principle of interference of SAW waves to be able to access specific nanomagnets in an array of nanomagnets between the IDTs in the delay line. The frequency of the wave can be manipulated in a way that with differing frequencies and constructive interference of the propagated and reflected waves, local areas of stress maxima and minima can be created. Those nanomagnets which lie on the stress maxima

will be accessed and clocked/switched while the ones lying in stress minima will not be affected and continue to keep their magnetic states.

STT and SAW: It was shown recently that writing bits in spin-transfer-torque random access memory can be reduced by an order of magnitude if a surface acoustic wave (SAW) is launched underneath the magneto-tunneling junctions (MTJs) storing the bits. (Biswas, Bandyopadhyay and Atulasimha, 2013). The scheme consists of using elliptical MTJs deposited between IDTs. Thus using SAW can increase the energy efficiency with which bits are written in STT memory by lowering the shape anisotropy barrier due to SAW induced stress anisotropy, thus reducing the write current significantly.

1.4.3 SAW based logic propagation, combinational logic and sequential logic

Unlike the isolated nanomagnets used in a memory scheme, a scheme consisting of dipole coupled nanomagnets can be used to show implementation of a basic Boolean NOT gate (Fig. 1.11).

Here the SAW passes through the dipole coupled nanomagnets and the combination of dipole coupling and stress transferred by the SAW can switch the magnetization in the less shape anisotropic magnet by 180º. This implements a Boolean NOT gate. The more shape anisotropic (on the left the scheme) nanomagnets are not affected by the strain because the SAW is not sufficient to beat the shape anisotropy and cause a magnetization rotation in these magnets.
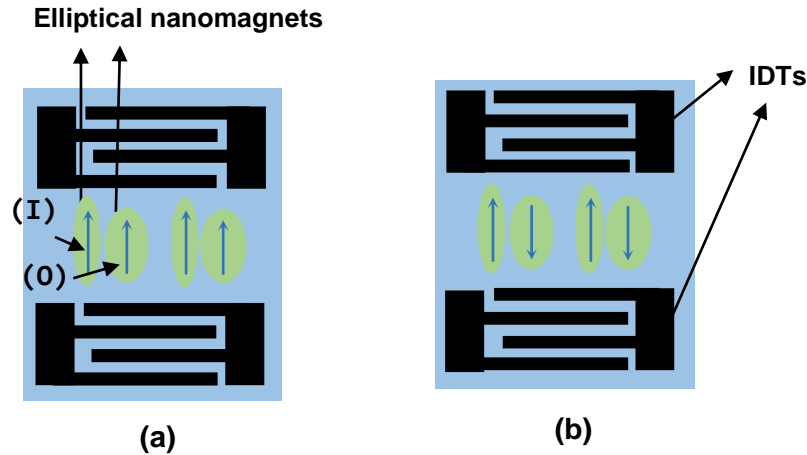
Fig. 1.11: Schematic representing a NOT gate. (a) The blue arrows indicate the direction of the magnetization state of the nanomagnets. (b) Upon acoustic wave propagation¸ a mechanical strain is generated and transferred to the nanomagnets which reverses the magnetization of the lower shape anisotropy nanomagnets (O).

If the SAW can be slowed down then bit propagation along a chain of nanomagnets as shown in Fig. 1.12 becomes a distinct possibility and so does combinational logic like a NAND gate and sequential logic like a Flip Flop. We assume the velocities that are needed to achieve these scheme may be obtained along specific orientations of the piezoelectric crystal or adding periodic barriers that slow the propagation velocity of the SAW wave.

Next, the schematic configuration of a NAND gate amenable to clocking with SAW waves is shown in Fig 1.12 (M.S. Fashami, 2014). It is composed of eight nanomagnets, which include Input-1 and Input-2, NAND gate elements and output. Nanomagnets are categorized in different groups of I, II, III and IV as the SAWs reach all elements of a specific group simultaneously and trigger magnetization rotation in each element of that specific group at the same time. In order to implement clocking with SAW waves the NAND gate has to be designed so that no group of neighboring elements are in one vertical line or perpendicular to the direction of propagation of the SAW wave as this is not amenable to sequential clocking of nanomagnets with a SAW wave. Furthermore, the NAND design in Fig 1.12 has a set of magnets that follow input-1 which are all

in a horizontal row while magnets that follow input-2 are at 45 degrees to the horizontal. The bias magnetic field of -300(A/m) is also applied on magnet marked III to resolve the "tie" cases when the inputs are different from each other (i.e. the two inputs are "0" and "1" or vice versa) . Such a geometry may be useful for implementing elements such a flip-flops (Fig. 1.13) where one of the input is basically the output fed back and cannot be in a nice horizontal line. The 90 degree phase between each group of magnets clocked has to be achieved due to the path delay in the SAW wave travelling from one group to the next.
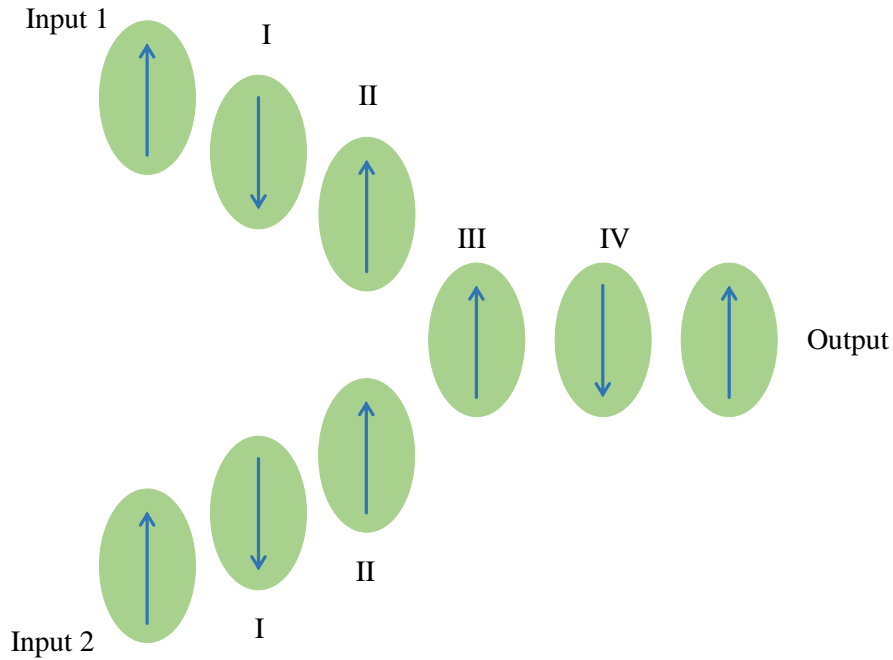
Fig. 1.12: Schematic view of computational NAND gate configuration under triggering of SAW. (M.S. Fashami, 2014)

To build a sequential logic device, feedback from the output state to the input is required. Since the acoustic wave propagation is unidirectional and because of timing and interference issues, one cannot use the same channel to propagate information both ways. This issue is solved

by dedicating a channel (in between two channels where information is propagated forward) to propagate information backwards by locating the SAW launcher on the other (right) side and propagating the SAW leftwards. This, combined with the "wire crossing" scheme-using ferromagnetic coupling (as shown in Fig. 1.13), will enable feedback.

However, the work in this thesis is restricted to the experimental demonstration of Boolean NOT gate using SAW as local clocking scheme only.
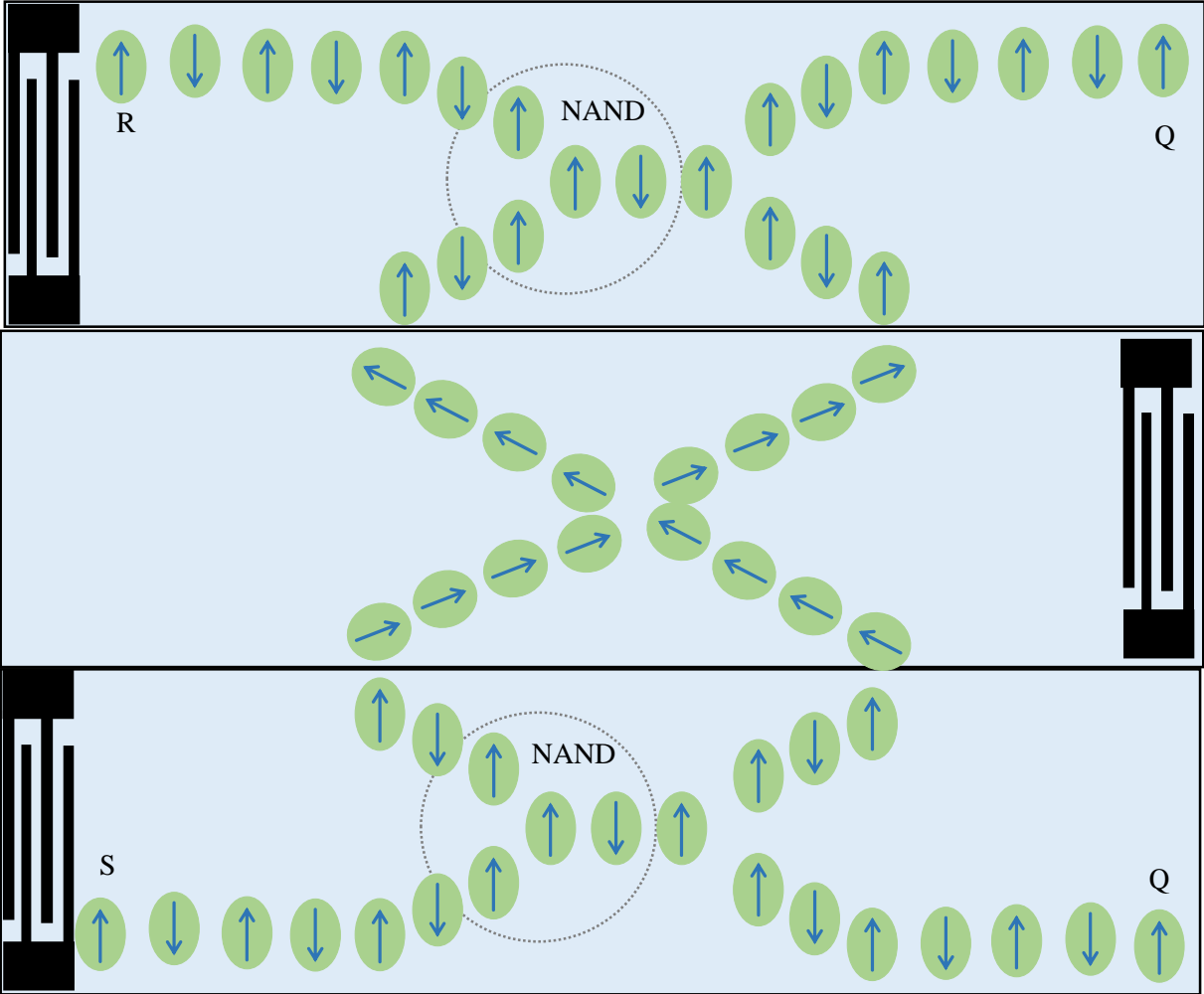
Fig. 1.13: RS Flip Flop built with NAND gates. To enable feedback we need to have a channel with SAW propagating in reverse direction between two channels that contain the NAND gates clocked by SAW travelling in forward direction.

1.4.4 Fabrication methods

The process flow for fabrication and characterization of magnetostrictive ellipsoidal nanomagnets to study SAW induced magnetization rotation is as follows:

1) Deposit Aluminum by e-beam evaporation and photoresist spin coat

2) Photolithography and PAN etch to create IDTs

3) Spin-coat electron-beam resist on piezoelectric substrate

4) Perform electron-beam lithography (EBL)

5) Deposit magnetic material using electron-beam evaporation

A detailed explanation of the process methodology is given below:

1) Deposit Aluminum by ebeam evaporation and Photoresist spin coat

A pristine Lithium niobate substrate is loaded in an electron beam evaporator, having a base pressure of ~3.5×10^{-7} Torr. A 200 μm Aluminum layer is deposited at a deposition rate of 2 angstrom/s. This results in the 4" substrate being coated with Aluminum. Next this substrate is spin coated at 4000 rpm for 30 seconds with photoresist (SPR 3012). It is then baked on a hot plate at 90°C for 5 minutes. This results in a resist thickness of about 100 nm.

2) Photolithography and PAN etch to create IDTs

The substrate is then loaded onto a contact aligner which has a glass mask with the patterned IDTs. The substrate is exposed to UV light, which passes through the patterned mask. The exposure is at 50 mW/cm^2 and is done for about 10 s. Then the substrate is put in a developer (Microposit MF-CD-26) for about 120 seconds. This selectively washes away the UV exposed areas on the substrate. This can be seen with naked eyes since the resist has a dye in it and development is stopped 10 seconds after the dye disappears in the developer. Then the substrate is then left in a

PAN (Phosphoric-Acetic-Nitric acid) etch solution at 40º C for about 4 minutes. This process etches away excess aluminum and leaves Aluminum IDTs onto the Lithium niobate substrate.

3) Spin-coat electron-beam resist on piezoelectric substrate

A bilayer of positive e-beam resist (495K PMMA and 950K PMMA; 4% Anisole) was then spin-coated using the following procedure: A static dispense of ~3 ml (495K PMMA) was carried out on the substrate followed by a dynamic spread at 500 rpm for 5 seconds. The spin cycle was performed at a rate of 2000 rpm for 45 seconds. A pre-bake at 90° was then performed for 300 seconds, resulting in a 495K PMMA layer of ~ 30 − 40 nm (Microchem). The top 950K PMMA layer was spin-coated next using the same procedure, resulting in the final bilayer PMMA having a thickness of ~ 190 nm.

The reason for the bilayer PMMA (instead of a single layer) is to ensure effective liftoff of metallic structures. Since the bottom resist layer, 495K PMMA, has lower molecular weight than the top layer, it has a greater sensitivity to exposure from the electron beam during lithography than the upper resist layer having higher molecular weight. This results in the bottom resist layer developing with an enhanced undercut (as shown in Fig. 1.14b), thereby ensuring little to no deposition along the sidewalls of the resist during material evaporation.
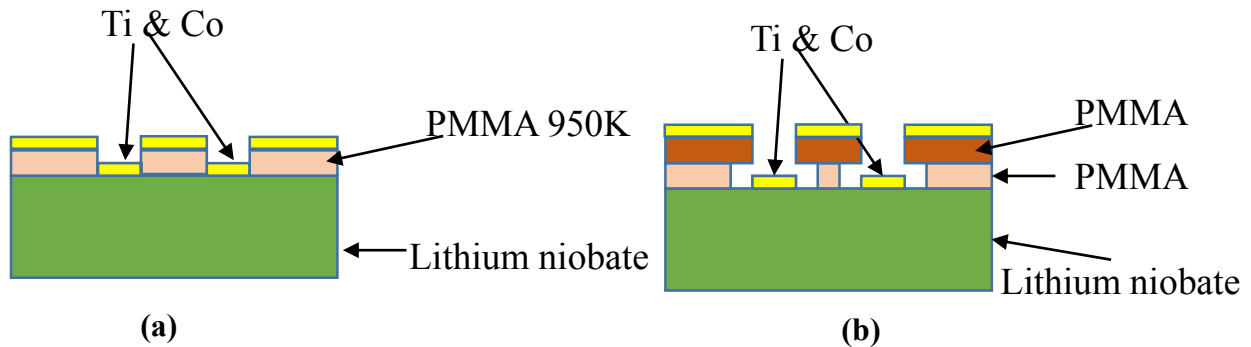
Fig. 1.14: Schematic showing the advantage of a bilayer PMMA over a single layer and the essential undercut needed for a clean lift-off.

4) Perform electron-beam lithography (EBL)

Following the bilayer PMMA resist spin-coating, the patterns to be created are written and transferred to the bilayer resist through EBL using a Hitachi SU-70 Scanning Electron Microscope (SEM) in conjunction with the Nabity Nanometer Pattern Generation System (NPGS). The SEM is configured to have an acceleration voltage of 30 KV and the appropriate aperture/lens setting to give a beam current of 60 pA. The beam current is 60 pA, as measured during the SEM beam optimization. The center-to-center spacing defines the spacing of the exposure points during the electron beam exposure. After pattern exposure is completed with the SEM/Nabity NPGS system, the PMMA-coated substrate is then developed in an MIBK:IPA (1:3) [(methyl isobutyl ketone: isopropyl alcohol)] solution for 70 seconds, rinsed in Isopropyl Alcohol for 20 seconds to remove the exposed PMMA and finally blow-dried.

5) Deposit magnetic material using electron-beam evaporation

Next, the substrate is loaded in an electron beam evaporator, having a base pressure of ~3.5 $\times 10^{-7}$ Torr. A 5 nm Ti adhesion layer is deposited at a deposition rate of 0.5 angstrom/s, followed by a 12 nm layer of Co at a rate of 0.3 angstrom/s. Finally, lift-off was performed by soaking the substrate in acetone for ~5 minutes at 30° C and using an ultrasonic cleaner for 10 seconds to strip off the Ti/Co layers above the unexposed PMMA regions.

1.5 Need for higher magnetostriction for better yield

As reported in a recent work (D'Souza *et. al.*, 2016), the switching statistics (number of nanomagnets switched/total nanomagnets strained) of multiferroics using strain is low because often the stress anisotropy energy is unable to overcome the pinning sites in these nanomagnets. The reason is explained as follows:

The stress energy anisotropy of a nanomagnet can be expressed as

$$E_{stress\text{-}anisotropy=}\ \mu_o\ M_s\ H_{eff}\ \sim (-3/2\ \lambda_s)\ \sigma$$

$$H_{eff}= (1/\ \mu_o\ M_s\ )(-3/2\ \lambda_s)\ \sigma$$

where H_{eff} is the effective magnetic field due to the applied stress (σ), μ_0 is the permeability of free space ($4\pi \cdot 10\text{-}7$ H·m-1), M_s is the saturation magnetization of Cobalt (14.22×105 A·m-1), ($3/2\ \lambda_s$) is the saturation magnetostriction of Co (50 ppm). When $\sigma= 80$ Mpa is the stress applied to the nanomagnet the value of $H_{eff} \sim 30$ Oe for cobalt. This points to a fundamental limitation of strain clocking with Co nanomagnets. Besides the formation of pinning sites leading to high coercivity of Co nanomagnets, the low yield of switching events in a large nanomagnetic array could be attributed to the weak magnetoelastic coupling of the magnetostrictive material investigated.

If materials with better Magnetoelastic coupling and higher magnetostriction could be fabricated (e.g. Galfenol, Terfenol-D), then switching statistics could improve significantly. This is because H_{eff} due to strain ~100Oe for such materials can be achieved at the same stress levels (80 MPa) and can easily overcome any pinning sites or other defects and lead to better switching. However to be able to use such materials with high magnetostriction, we need to study the magnetization dynamics of these materials. Since FeGa is a binary alloy (unlike Terfenol D!) and it's relatively easier to grow we study the dynamic parameters associated with magnetization switching in thin films of FeGa using FMR in this thesis.

1.6 Magnetization dynamics in thin films and FMR

Ferro-Magnetic Resonance (FMR) is an experimental technique used in the study of ultra-thin film magnetic properties. Essential parameters describing the magnetic properties of ultrathin films can be measured or estimated using FMR. These include magnetic anisotropy, magnetic moment, Curie temperature, magneto-elastic coupling coefficients and relaxation mechanisms of the magnetization. The first experimental observation of ferromagnetic resonance (FMR) was made by Griffiths (Griffiths J.H.E, 1946). The initial theory of this resonance phenomenon was given by Kittel (Kittel C., 1947)

1.6.1 FMR and extraction of parameters

FMR is a method to measure magnetic properties by detecting the precessional motion of the magnetization in a ferromagnetic sample. It is thus related to the electron paramagnetic resonance technique. From a macroscopic point of view, the applied static magnetic field H causes the total magnetic moment to precess around the direction of the local field H_e, before relaxation processes damp this precession and the magnetization aligns with H_e. If the sample is irradiated with a transverse r.f. field (microwaves of typically 1–35 GHz), and if the r.f. frequency coincides with the precessional frequency, the resonance condition is fulfilled and the microwave power is absorbed by the sample. The motion of the magnetization around its equilibrium position is described by LLG equation of motion:

$$\frac{dM}{dt} = -\mu_0 \gamma M \times (H + H_e) + \frac{\alpha}{M_s}(M \times \frac{dM}{dt})$$

Where M is the magnetization, μ_0 is the vacuum magnetic permeability, $\gamma = g\frac{e}{2m_e}$ is the gyromagnetic ratio, H is the externally applied DC magnetic field and H_e is the effective field which includes the driving r-f microwave magnetic field h (t) of frequency$\frac{\omega}{2\pi}$, the demagnetizing field and the magneto crystalline anisotropy field; α is the dimensionless Gilbert damping parameter, that describes a viscous-like damping proportional to the velocity of the magnetization. Usually the absorption derivative, as shown in figure 6, is measured (Farle, 1998). The resonance signal resembles a Lorentzian line-shape. The resonance field position H_{res} depends on the angles, anisotropy parameters, g-factor, and magnetization of the sample. The linewidth ΔH is proportional to the relaxation constant which is known as Gilbert damping coefficient.
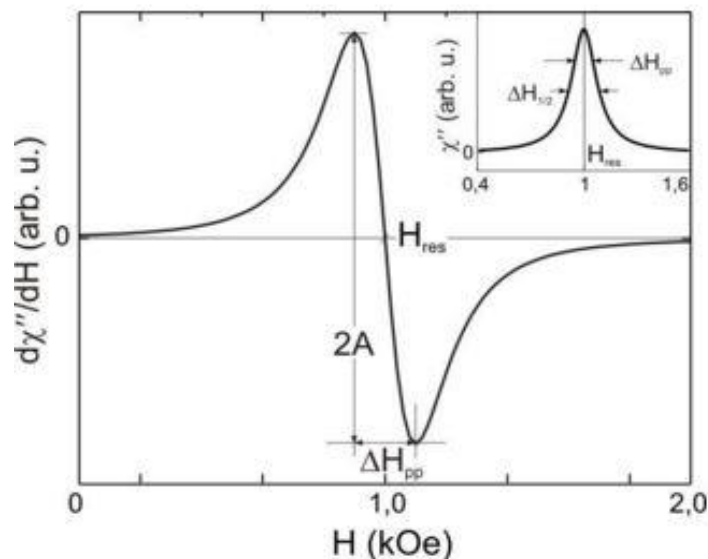
Fig. 1.15: Derivative of absorption with DC magnetic field. (Inset) Absorption with DC magnetic field showing the resonance field. [Image source: http://www.physik.fu-berlin.de/einrichtungen/ag/ag-kuch/research/techniques/fmr/index.html]

Chapter 2: Experimental demonstration of Acoustic wave based switching of nanomagnets from Single domain to vortex.

2.1 Introduction

The triggering of magnetization dynamics using surface acoustic waves (SAWs) can implement a low power dissipation switching methodology while reducing the burden of lithographic contacts to each individual nanomagnet. However, the use of this method for implementing memory has remained largely unexplored.

In this chapter, I experimentally demonstrate SAW-based magnetization switching from single domain to a stable vortex state in isolated nanoscale elliptical cobalt nanomagnets that are not dipole coupled to any other nanomagnet. Magnetic Force Microscopy (MFM) is used to characterize the nanomagnets' magnetic state before and after the SAW clocking cycle. The pre-stress state, which is a single domain state, goes into a vortex state upon application of the SAW, and *remains* in the "vortex" state even after the SAW has propagated through and there is no longer any strain in the nanomagnets. The vortex state is therefore *non-volatile* and a strong magnetic field has to be applied to 'reset' the magnetization of the nanomagnets to their initial single-domain magnetic state. I also note that after the AW propagation, the nanomagnets either retain their initial single-domain magnetization orientation (not shown here), i.e. the shape anisotropy due to dimensional variation in nanofabrication resists the stress induced change to a vortex state, or switch to a non-volatile vortex state that is stable and does not show any variation after repeated MFM scans (section 2.5.3). However, none of the nanomagnets studied experienced a complete

reversal in magnetization (i.e.180º switching). I also show that this observation is consistent with micromagnetic simulations used to study the magnetization dynamics during stress application. They successfully predict the formation of the non-volatile vortex state when the single domain state is perturbed by the SAW-generated strain which is demonstrated experimentally.

The thickness of the piezoelectric wafer used is about 1/3 rd the wavelength of the acoustic waves being launched from the IDTs. This leads to particle motion in the bulk of the substrate and not just at the surface level. So we use the term AW and SAW interchangeably in the rest of the thesis. Please note that the particle motion at the surface still has Rayleigh mode characteristics. Hence all the equations and used for Rayleigh mode when SAW propagates on the surface of a piezoelectric substrate, still apply (Datta, S. 1996).

2.2 Acoustic waves: theory, Design and fabrication

Surface waves propagate along the surface and decay into the depth within a distance of the order of a wavelength. It is thus not uniform in the direction perpendicular to the surface. However, there is little loss along the propagation direction and no variation in transverse direction to the propagation direction. The particles move both in the direction of wave propagation and perpendicular to the surface.

In SAW technology we are almost always interested in piezoelectric substrates where the acoustic fields generate electric fields. The electric field is conveniently described in terms of an electric potential, ϕ. With SAW, the purpose is to generate and control surface waves. This is done by interdigitated transducers (IDTs) fabricated on a piezoelectric lithium niobate substrate. Since all interactions with surface waves take place through the surface, we are often interested in the values of the particle displacements or electric potential (ϕ) at the surface. 128º Y-cut Lithium

Niobate substrate is chosen because of its high piezoelectric coupling constant (K^2=5.6%) and a relatively moderate acoustic wave velocity of 3996 m/s.

An acoustic wave is generated and propagated along the substrate by applying a sinusoidal voltage V, between the IDTs . This sinusoidal voltage is applied at the characteristic frequency of the fabricated IDTs. The relationship between electrostatic potential ϕ, and applied sinusoidal voltage, V, is

$$\phi = \mu(f)\, V \qquad\qquad (2.1)$$

Here, $\mu(f)$ is the transmitter response function, which is a function of the frequency of applied voltage, f. This transmitter response function is, in turn, a product of the single tap response function $\mu_s(f, \eta)$ and array factor, $H(f)$:

$$\mu(f) = \mu_s(f, \eta)\, H(f) \qquad\qquad (2.2)$$

$$\mu_s(f, \eta) = \mu_s(f_0, \eta)\, \sin(\pi f/2f_0)$$

$$H(f) = N \sin N\pi\, [(f-f_0/f_0] \,/\, N\pi\, [(f-f_0/f_0]$$

The single tap response function varies with frequency, f, and the metallization ratio, η. For an applied frequency of $f = f_0$ and a large metallization ratio of say 0.75, $\mu_s(f, \eta) = 0.9K^2$ where $K^2 =$ 0.056.[30] When the frequency of applied voltage is equal to the characteristic frequency of the IDTs, the array factor is equal to the pairs of electrodes in the transmitter IDT, N.

The IDTs are fabricated using conventional photolithography and wet etching processes, as described in chapter 1. Two sets of IDTs are fabricated. One set is used to launch the AW and the other is used to sense the propagated AW. For the purpose of these experiments, the receiver transducer is redundant and is only used to check electrical connections and confirm the propagation of AW with minimal attenuation.

Elliptical Co nanomagnets are delineated in the space between the IDTs, shown in Figures 1d and 1e. Elliptical Co nanomagnets of dimensions ~ 340 nm × 270 nm × 12 nm were fabricated on a 128° Y-cut lithium niobate substrate as described in Chapter 1.

The magnetostrictive nanomagnets of nominal dimensions 340 nm × 270 nm × 12 nm are initially magnetized along the major axis with a large external magnetic field of ~0.2 Tesla (Figure 1a) and characterized by MFM (Figure 2b). The magnetization state of these nanomagnets is single-domain, as expected.

2.3 Schematic design

SAWs are excited and detected by aluminum interdigitated transducers (IDTs) fabricated on a piezoelectric lithium niobate substrate. Elliptical Co nanomagnets are delineated in the space between the IDTs, as explained in the Methods section and shown in Figures 2.1d and 2.1e. The magnetostrictive nanomagnets of nominal dimensions 340 nm × 270 nm × 12 nm are initially magnetized along the major axis with a large external magnetic field of ~0.2 Tesla (Figure 2.1a) and characterized by MFM (Figure 2.4b). The magnetization state of these nanomagnets is single-domain, as expected.

An acoustic wave is generated and propagated along the substrate by applying a sinusoidal voltage of 50 V_{p-p} between the IDT's (Figure 2.1b). This sinusoidal voltage is applied at a frequency of 3.5 MHz (characteristic frequency of the fabricated IDTs). The resulting electrostatic potential associated with the SAW in the delay line of Lithium Niobate is 100.8 V.

The particle displacement in the substrate due to SAW is 0.18 nm per volt of electrostatic potential. The maximum strain generated by this acoustic wave in the substrate over a length of 340 nm length is calculated to be 142.16 ppm. Assuming that this maximum strain is completely transferred to the nanomagnet, the maximum stress generated in the elliptical Co nanomagnets is

~30 MPa. Each nanomagnet experiences cycles of tensile and compressive stress (±30 MPa) along

its major axis corresponding to the crest and trough of the AW. I note that multiple cycles of AW
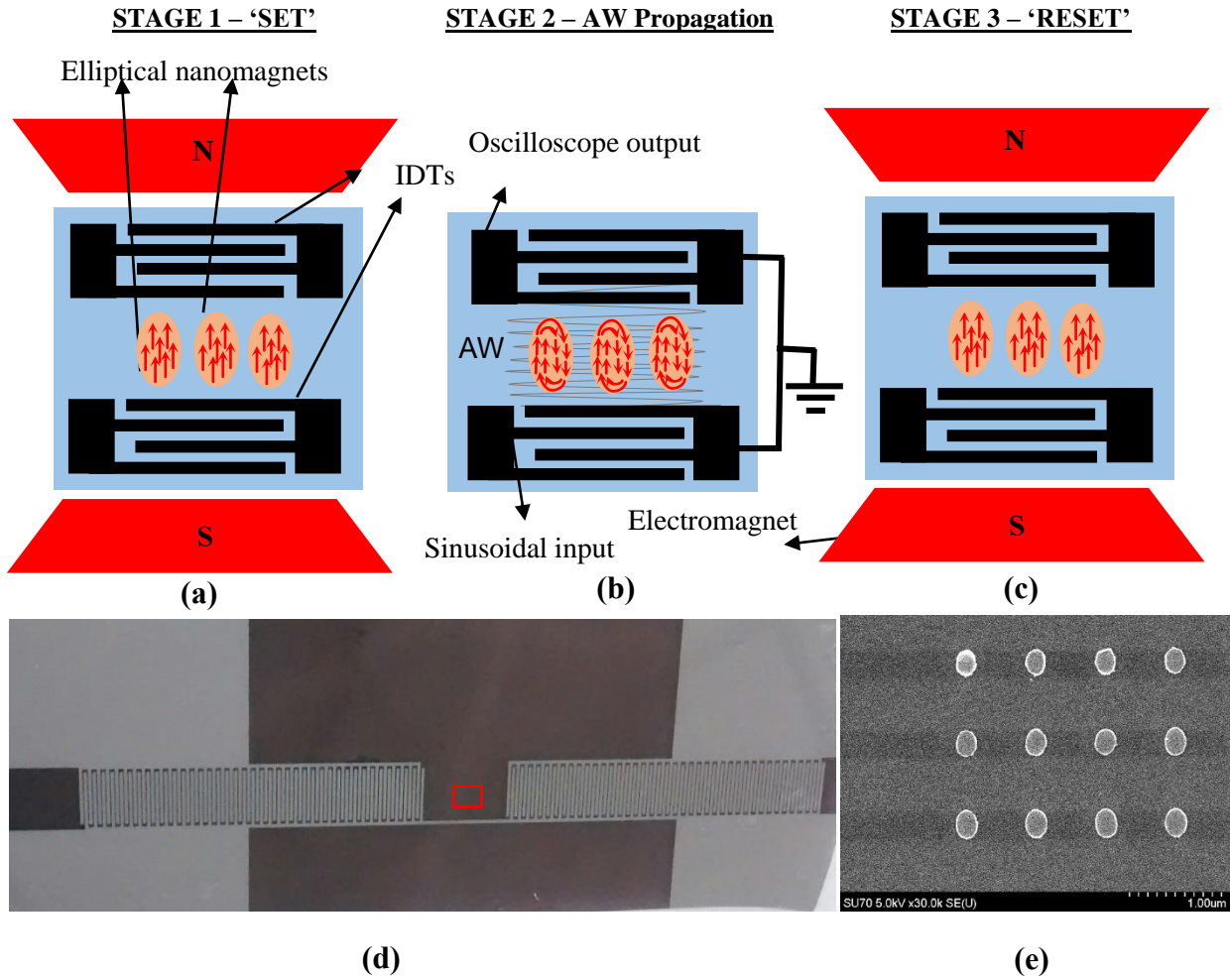
Fig 2.1. (a) Schematic of experimental set-up with initial application of an external magnetic field on the nanomagnets. The arrows indicate the direction of the magnetization state of the nanomagnets. (b) Upon AW propagation¸ a mechanical strain is generated and transferred to the nanomagnets which switches the magnetization of the nanomagnets to a 'vortex' state. (c) 'Reset' of the nanomagnets' magnetization by the external magnetic field. (d) SEM micrograph of the lithium niobate substrate with the fabricated IDTs. The red rectangle highlights the region containing the nanomagnets in the delay line. (e) SEM image of the nanomagnets with nominal dimensions of 340 nm × 270 nm × 12 nm.

Pass through the nanomagnet, not just a single pulse. Also since the wavelength of the acoustic

wave that generates the cyclic stress is much larger than the dimensions of the nanomagnets, at

any given instant the stress experienced by each nanomagnet is fairly uniform across its dimension. Since cobalt has negative magnetostriction, the tensile stress on the nanomagnet results in the magnetization rotating toward the minor axis. This is because tensile stress anisotropy shifts the minimum of the nanomagnet's potential energy profile to a location that corresponds to the magnetization being perpendicular to the stress axis. When the tensile stress is removed, the potential energy landscape should revert to its original symmetric double well profile (favoring a magnetization orientation along either direction collinear with the major axis). Therefore, the magnetization should have equal probability of either returning to its original orientation along the major axis or switching its orientation by 180°. Furthermore, when the compressive stress cycle is applied, a magnetization orientation parallel to the major axis is preferred and this will only reinforce the magnetization state that existed at zero stress. Thus, after AW propagation through the nanomagnets, one would ideally expect the magnetization to be along the major axis, i.e. either point along the original direction, or switch by 180°.

2.4 Results

The results we see are different from expectation. As seen in the MFM image of Figure 2.2 c, after SAW propagation (Post-SAW, Cycle 1), the magnetization state is no longer of a single-domain nature. Instead, the magnetization goes into a 'vortex' state which persists indefinitely after the removal of SAW.

| | Topography | Pre-AW (Cycle 1) | Post-AW (Cycle 1) | Pre-AW (Cycle 2) | Post-AW (Cycle 2) |
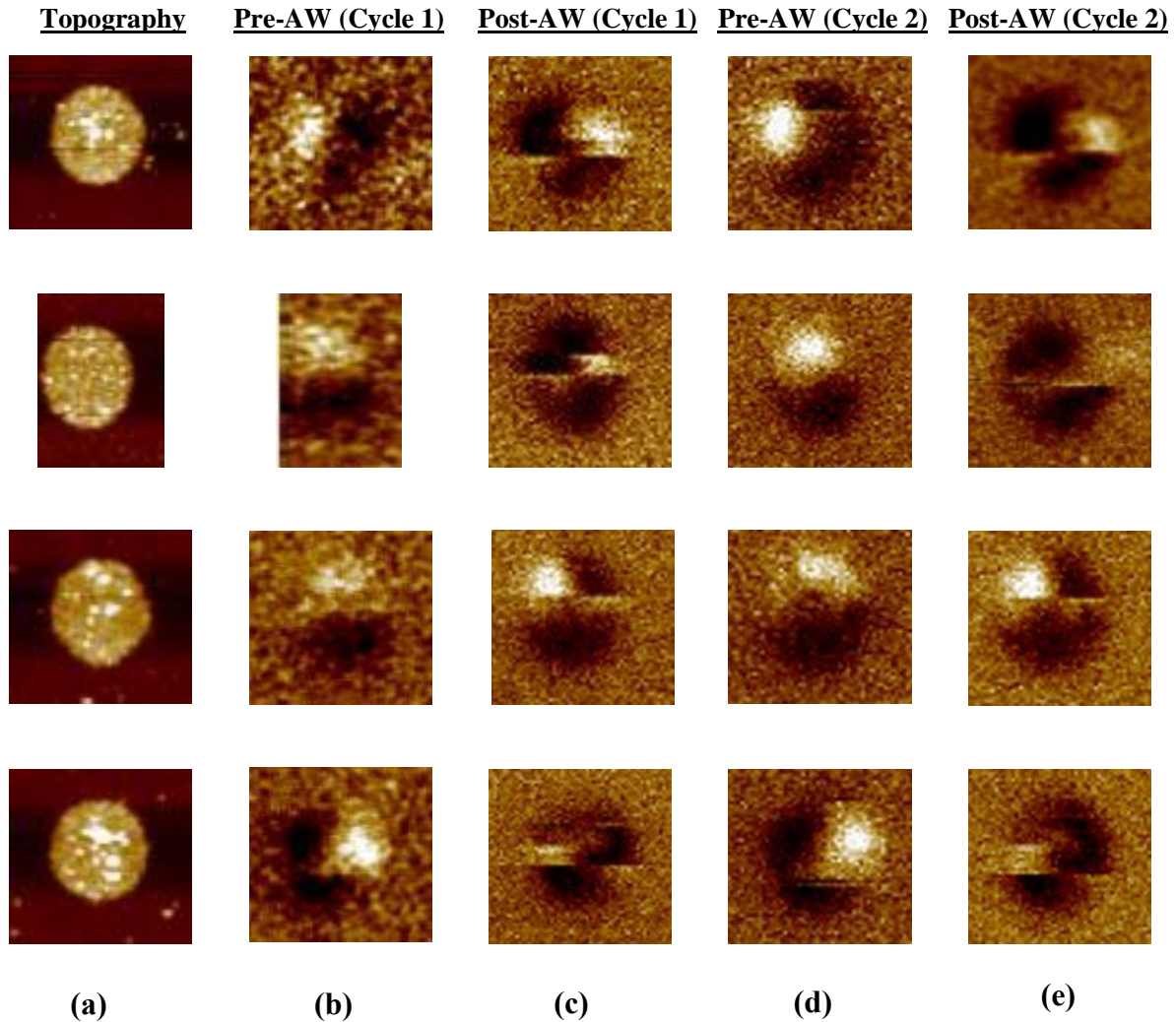
Fig. 2.2. (a) Topography of Co nanomagnets on PMN-PT substrate. (b-e) MFM images of 4 different Co nanomagnets. (b) In the pre-stress state prior to AW propagation, the nanomagnets possess a single-domain magnetic state after being initialized by a magnetic field applied along the major axis, (c) In the post-stress state after AW propagation, the magnetization enters into a stable 'vortex' state. (d) The nanomagnets are 'reset' by a magnetic field along the same direction as the initial state. (e) In the second post stress state, the magnetizations again enter into the same vortex state as in (c).

Here, it's notable that since the MFM tip is magnetized in a direction perpendicular to the substrate, it is sensitive to variations in the perpendicular (out-of-plane) component of the magnetic stray field, with 'bright' (and 'dark') regions indicating a repulsive (and attractive) force between the tip and sample. Thus, there is strong bright and dark contrast when the nanomagnet is in a near single domain state (Figures 2.2 b, d). This experimental observation is later rigorously corroborated by detailed micro-magnetic simulations. These simulations also explain why the

tensile stress spawns the vortex state, why it is stable and why it is preserved when the subsequent compressive stress cycle is applied or when the stress is completely withdrawn. The MFM images in Figures 2.2 (c, e) represent the magnetic state of the nanomagnets *after* the AW has propagated and is not an instantaneous visualization. The contrast seen in the images is a quadrant like representation of the vortex state (Figures 2.2c, e). The contrast is usually sharper in micron sized magnets; it is not so sharp here because of the smaller (sub-micron) size of the magnets (Figure 2.2c, e).

To 'reset' the magnetization of the nanomagnets to the original single domain magnetization state, a large external magnetic field of 0.2 Tesla is applied along the major axes of the nanomagnets in the manner shown in Figure 2.1c (Cycle 2). The MFM images of exactly the same nanomagnets after this 'reset' step are shown in Figure 2.2d (Cycle 2). The images clearly show that the single domain pre-stress state of the magnetization has been restored since the images in Figure 2.2d are nearly identical to those in Figure 2.2b.

To establish repeatability, AW is again applied as shown in Figure 2.1b. The wavelength of the acoustic wave is much larger than the dimension of the nanomagnets (Figure 2.1b) and the size of the nanomagnets has been enlarged in the schematic. The magnetization of the nanomagnets go into a vortex state again. The resulting MFM images are shown in Figure 2.2e. The images clearly show that the magnetization goes into same vortex state again in Cycle 2 since the images in Figure 2.2e are nearly identical to those in Figure 2.2c.

2.5 Discussions

The experimental results are compared against theoretical predictions of magnetization dynamics computed with the MuMax simulation package (details explained in appendix 1). The simulations were carried out by a fellow graduate student Dhritiman Bhattacharya.
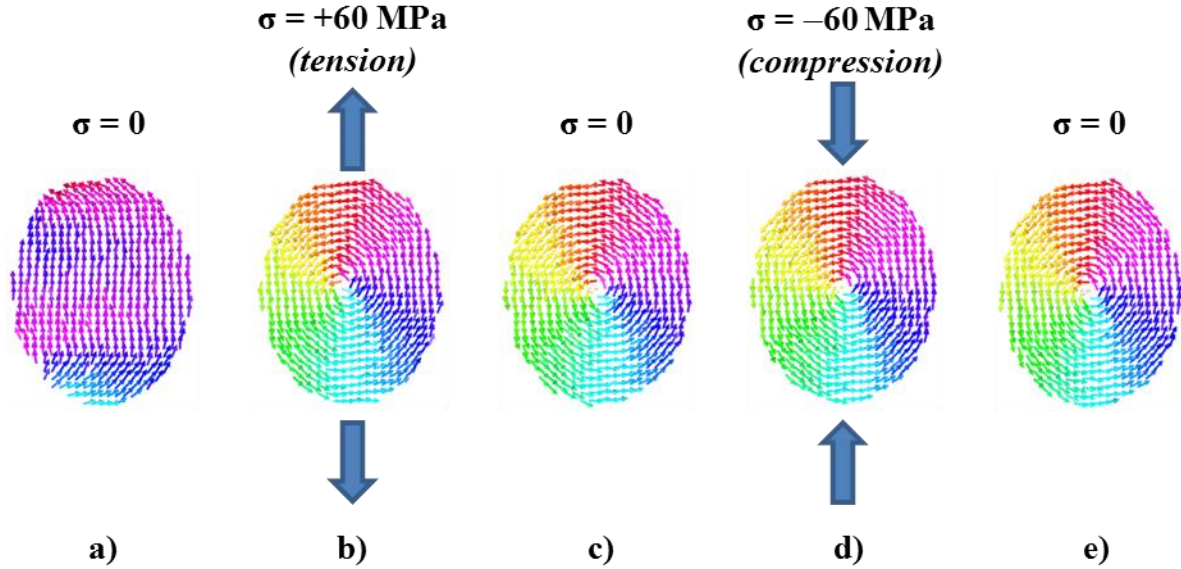
Fig. 2.3. Micromagnetic simulations of a nanomagnet with dimensions of 340 nm × 270 nm × 12 nm for the following scenarios: a) Relaxed pre-stress state, b) Tensile stress of +60 MPa, c) Post-stress at 0 MPa, d) Compressive stress of -60 MPa, and e) Post-stress at 0 MPa.

The switching from a single-domain to a vortex state under tensile stress can be explained by analyzing the various energies involved (exchange, demagnetization, stress and total) (A. Vansteenkiste *et. al.* 2014.). The total energy calculations show that the vortex state is a local energy minimum and that there exists an energy barrier between the initial relaxed and final vortex states (D. Bhattacharya *et. al.* 2015). When the stress anisotropy energy overcomes this barrier, the magnetization enters a vortex state and remains in this state even after the stress is withdrawn since it is a local minimum. A tensile stress not only drives the magnetization of the nanomagnet to a

vortex state, but also causes a slight increase in the magnetization component along the *minor* axis within the vortex (Figure 2.3b), albeit with the net magnetization remaining zero. Conversely, a compressive stress results in a slight increase in magnetization component along the *major* axis (Figure 2.3d). Although the visible difference in the tensile (Figure 2.3b) and compressive (Figure 2.3d) states is very small, the tendency for the magnetization to align along the major and minor axes, respectively, is expected. This is because the negative magnetostriction of Co causes the easy axis to lie along the long (short) axis when a tensile (compressive) stress is applied. Note that magnetization rotation occurs when the stress anisotropy energy overcomes the shape anisotropy energy. However, due to the presence of a very stable vortex state, the simulations show only a slight deviation from this state at the maximum compressive or tensile stress applied. This shows that the applied stress is clearly not sufficient to drive the magnetization out of the stable vortex state. The magnetization remains in the vortex state even after removal of the stress and an external magnetic field (applied along the major axis) is required to restore the single-domain magnetization state along the easy (major) axis.

While the micromagnetic simulations support the experimental MFM analysis of magnetization switching from single-domain to vortex states, the magnitude of stress required to overcome the energy barrier and enter the vortex state as predicted by the theoretical simulations (60 MPa) is larger than that generated in our experiments. This is not entirely unexpected due to the fact that only uniaxial stress is assumed in the simulations, whereas the AW produces a tensile stress of ~ +30 MPa along the major axis and a compressive stress of ~10 MPa along the minor axis (calculated from the materials' Poisson's ratio values). Therefore, the net stress experienced by the nanomagnet due to the AW will be ~40 MPa. Furthermore, stress concentrations due to

non-uniformities, cracks, etc. in the vicinity of the fabricated nanomagnets could increase the actual stress seen by these nanomagnets, which would explain the remaining discrepancy.

2.5.1 Energy dissipation per magnet

The energy dissipated during AW propagation for magnetization switching can be determined by calculating the total power generated by the acoustic wave. For a 128° Y-cut lithium niobate substrate having a characteristic wave velocity, $v_0 \sim 4000$ m/s , operating frequency $f = 3.5$ MHz and a potential $\phi = 100.8$ V, the power density per unit beam width is 1333.6 W/m, as described in the Methods section. For the purpose of estimating the energy dissipation per nanomagnet, I consider the nanomagnets used in the experiment having lateral dimensions of 340 nm × 270 nm and assume that a 2-dimensional array of such magnets can be designed with a center-to-center separation of ~0.5 μm between the nanomagnets (both along the AW propagation direction and perpendicular to it). With negligible AW attenuation at low frequencies (less than 0.1% over a length of 1 cm, at 10 MHz[34]), it can be safely assumed that at a frequency of 3.5 MHz, the AW can clock a ~2 cm long chain of nanomagnets with minimal attenuation. Considering an IDT beam width of 1 cm, a single AW cycle can clock 800 million nanomagnets and the energy dissipated per nanomagnet for one AW cycle (tension and compression) of time period 285.7 ns is ~4.76 fJ. If the clocking frequency is increased to, say, ~500 MHz while the power is kept constant (as less stress over smaller time is needed if materials with large magneto-elastic coupling such as Terfenol-D are used) the energy dissipation can be decreased to a mere ~47.6 aJ per nanomagnet. This would make the AW based clocking extremely energy efficient without requiring lithographic contacts to each and every nanomagnet.

2.5.2 Electrical characterization

It is important to confirm the propagation of SAW between IDTs on the lithium niobate substrate. This is also important to verify attenuation as SAW propagates in the delay line. Sinusoidal and square wave voltages are applied on a control substrate made of Glass which has the identical design of Aluminum IDTs on it. Then the voltage is applied to IDTs on the Lithium niobate substrate. The transmitter and receiver IDTs are connected to an Oscilloscope.

The Fig. 2.2 (a) and (b) show the oscilloscope image when sinusoidal and square wave voltage respectively are applied to the IDTs fabricated on glass. The figures 2.3 (a) and (b) show the oscilloscope images of sinusoidal and square wave voltage respectively are applied to the IDTs fabricated on Lithium niobate. It can be clearly seen that the receiver IDTs on Lithium niobate show sinusoidal electrical signal with applied frequency. The voltage of the signal is almost equal to the applied voltage thus proving no loss of amplitude in the delay line. Also noticeable is the output voltage in figure 2.3 (b) is sinusoidal, even though applied voltage is a square wave. Thus, the Acoustic wave device acts as a filter when the applied voltage is of the frequency of the characteristic frequency of the device, as theoretically predicted in literature.
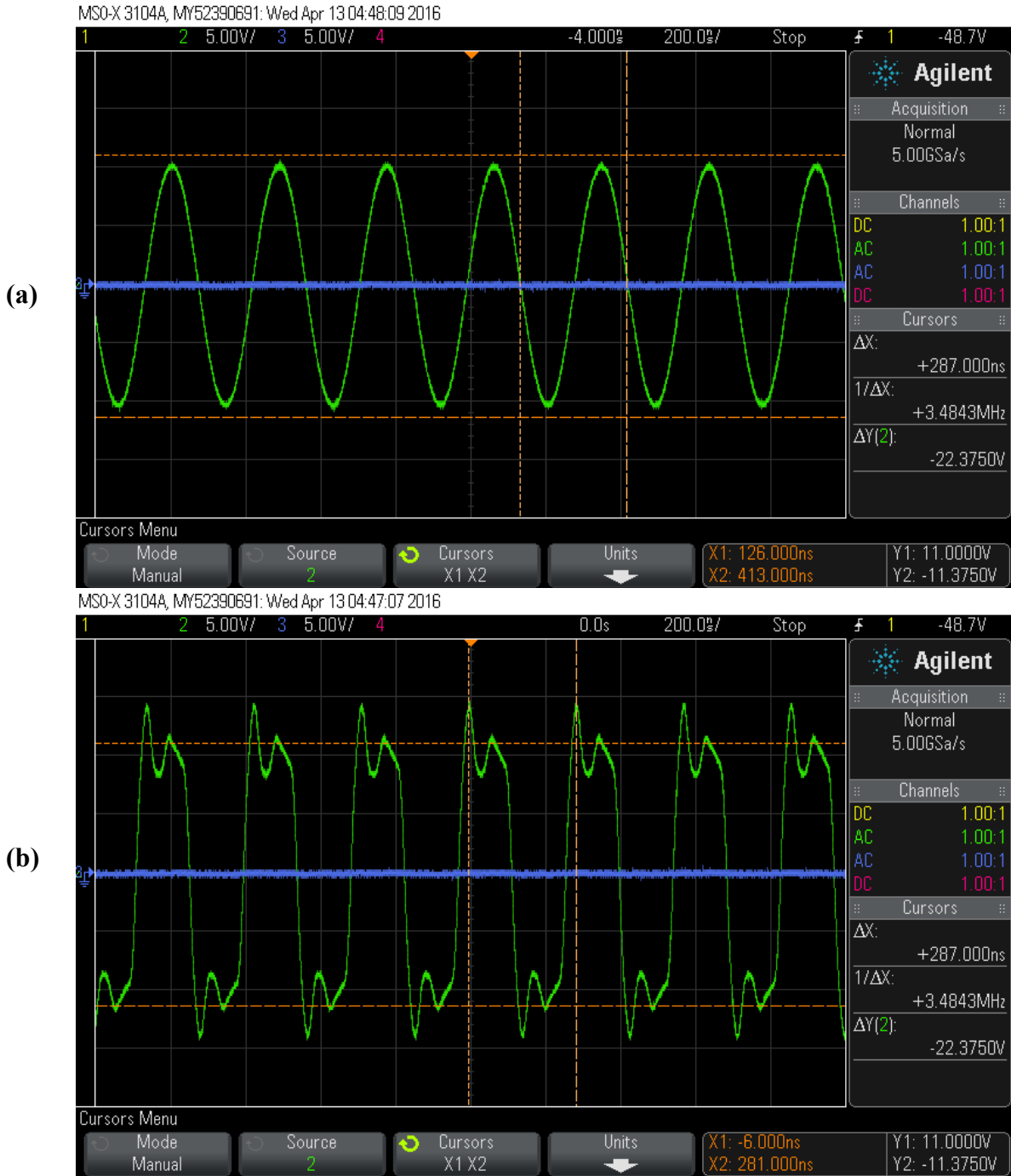
Fig. 2.4: (a) Sinusoidal voltage applied to input IDT on Glass. (b) Square wave applied to input IDT on Glass. The input is shown in green. The output from receiver IDT is in blue.

43
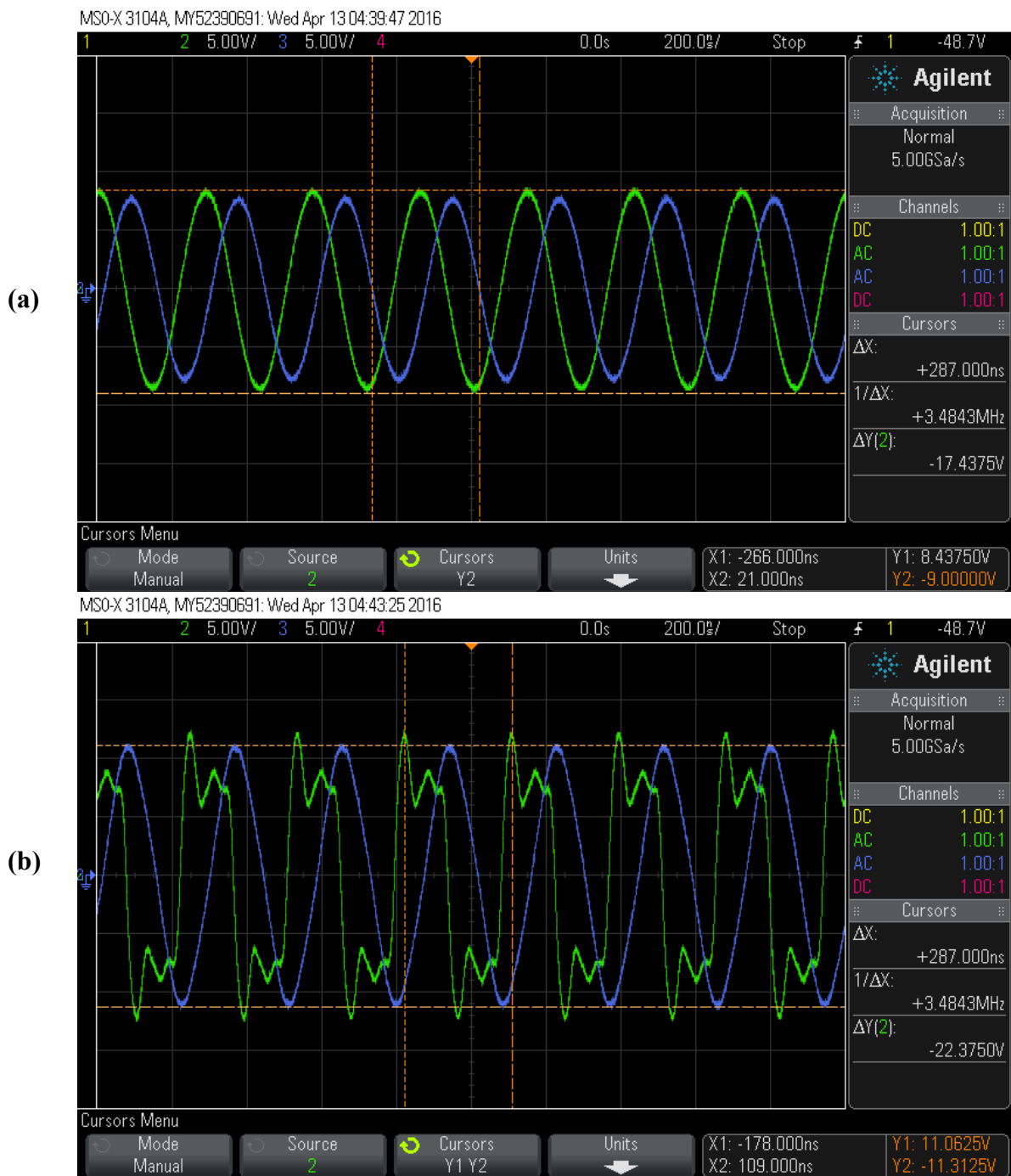
Fig. 2.5: (a) Sinusoidal voltage applied to input IDT on Lithium Niobate. (b) Square wave applied to input IDT on Lithium Niobate. The input is shown in green. The output from receiver IDT is in blue.

2.5.3 Consecutive MFM scans to demonstrate no tip-induced effects

To demonstrate that the magnetization states of the nanomagnets are stable and not affected by the magnetization of the MFM tip, we performed consecutive MFM scans of the pre-AW (not shown here) and post-AW (Figure 2.6) states to verify that the magnetization states show no variance. The images shown in Figure 2.6 illustrate the consecutive post-AW MFM phase

(a)   **(b)**   **(c)**   **(d)**
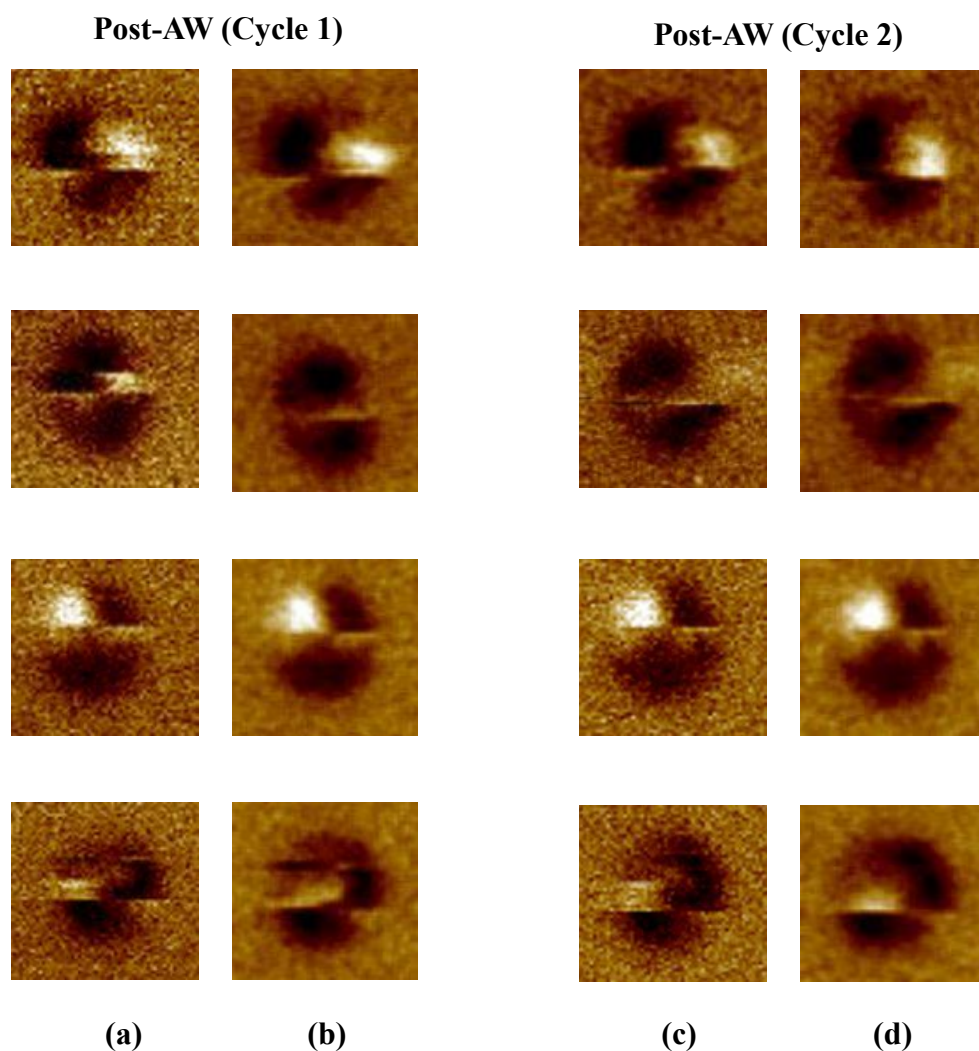
Fig. 2.6: Consecutive MFM scans of post-AW magnetization states of four different Co nanomagnets. Columns a and b are same as columns c and e in Figure 2 of the main paper. Columns b and d are repeated scans of columns a and c respectively, when the slow scan axis of the tip is different.

images of the four nanomagnets shown in Figures 2.2c and 2.2e of the main paper. These images (Figure 2.6) represents consecutive scans along the slow-scan axis, and demonstrate that the magnetic states of the nanomagnets experience no tip-induced magnetization rotation and are also unaffected by the scan direction.

2.6 Conclusion

In conclusion, we have shown that acoustic waves, generated by IDTs fabricated on a piezoelectric lithium niobate substrate, can be utilized to manipulate the magnetization states in elliptical magnetostrictive Co nanomagnets. The magnetization switches from its initial single-domain state to a vortex state after AW stress cycles propagate through the nanomagnets. The vortex states are stable and the magnetization remains in this state until it is 'reset' by an external magnetic field. Furthermore, micromagnetic simulations performed using the MuMax package corroborate the vortex state formation and their being stable under subsequent tensile/compressive stresses. We have also shown detailed calculations to show that the energy expended in switching each nanomagnet is only tens of attoJoules. These results lay the foundation for energy efficient switching of nanomagnets with AW for future memory applications.

Chapter 3: Experimental demonstration of Acoustic wave based switching of dipole coupled nanomagnets

3.1 Introduction

Nanomagnetic logic and memory devices offer the benefit of non-volatility and energy efficiency, but the challenge is to find an energy-efficient way to switch the magnetic state of nanomagnets for bit operations. The traditional methods for switching magnetization, as discussed in the introduction chapter, include the use of electric current-generated magnetic field, spin transfer torque, current-driven domain wall motion, current-induced spin orbit torque or spin hall effect , and strain generated by applying an electrical voltage to a multiferroic nanomagnet . The energy dissipated in strain-induced switching can be as low as 0.6 atto-Joules (Fashami, Atulasimha and Bandyopadhyay, 2012), making it attractive. This strain is generated in a two-phase pieozoelectric-magnetostrictive multiferroic by applying an electrostatic potential to the piezoelectric layer using contact pads and transferring the resulting strain to the magnetostrictive layer via elastic coupling [Pertsev and Kohlstedt, 2009; Ahmad, Atulasimha and Bandyopadhyay, 2015)].

For some applications, such as Bennett clocking of pipelined dipole coupled logic (Atulasimha and Bandyopadhyay, 2010), it would be necessary to apply strain sequentially to successive magnetostrictive nanomagnets in an array. This would be lithographically challenging as described in section 1.3.2. An acoustic wave launched in the direction of the array with the appropriate wavelength, on the other hand, will sequentially generate local stress underneath each nanomagnet (when a crest of the wave reaches a nanomagnet), thereby effectively carrying out Bennett clocking of pipelined dipole coupled logic without lithographic contacts to individual

nanomagnets. This affords the best of both worlds - pipelined nonmagnetic logic for high speed computing and minimal lithography for high yield and low cost. The acoustic wave must have a phase velocity that is slow enough that the stress dwells sufficiently long in a nanomagnet for the reversal to occur. Therefore, there is a need to use slow waves and it has been theoretically shown that the wave velocity can be as low as 470 m/s for X-cut PMN-33%PT poled along $[111]_c$ (Xiuming Li *et. al., 2009)*. In this chapter, we demonstrate a simple proof of concept of implementing an acoustic wave clocked NOT gate using dipole coupled multiferroic nanomagnets.

The use of Surface Acoustic Wave (SAW) to lower energy dissipation in switching of nanomagnets with spin transfer torque has been studied theoretically (Biswas, bandyopadhyay and Atulasimha, 2013). The periodic switching of magnetization between the hard and the easy axes of 40 μm × 10 μm × 10 nm Co bars sputtered on GaAs (Davis *et. al.,* 2010) and Ni films (Kim *et. al.,* 2012) was experimentally shown, while the excitation of spin wave modes in a (Ga, Mn) As layer by a pico-second strain pulse has also been demonstrated (Bombeck *et. al. ,* 2012*)*. On in-plane magnetized systems, SAWs have been used to drive ferromagnetic resonance in thin Ni films (Weiler *et. al.,* 2011; Janušonis *et. al,* 2015*).* Recent theoretical work discussed the possibility of complete reversal of magnetization with acoustic pulses (Kovalenko *et. al.* 2013*; Thevenard *et. al.)*. The effect of acoustic waves on magnetization switching in single domain isolated nanomagnets to a non-volatile vortex state has also been demonstrated in the previous chapter. The pre-stress state, which is a single domain state, goes into a vortex state upon application of the acoustic waves, and remains in the "vortex" state even after the waves have propagated through and there is no longer any strain in the nanomagnets. The vortex state is therefore non-volatile.

In this paper, we demonstrate, acoustic wave-based magnetization reversal of a single domain, dipole coupled, elliptical cobalt nanomagnet that ultimately implements a Boolean 'NOT'

operation. Two elliptical nanomagnets are placed very close with their major axes parallel and the line joining their centers aligned along the minor axes. The ground state of the system is known to be the anti-ferromagnetic. In the pre-stress state, the magnetization of the nanomagnets are 'initialized' by a strong external magnetic field (FIG. 3.1a) that makes the ordering ferromagnetic (both magnetizations pointing in the direction of the field) and leaves both nanomagnets in a single-domain state. Upon acoustic wave propagation (FIG. 3.1b), the magnetization of the nanomagnet having the lower shape anisotropy switches and 'reverses' due to the dipole interaction with the neighboring nanomagnet having higher shape anisotropy (the stress anisotropy energy is unable to overcome the higher shape anisotropy). The stress anisotropy energy generated in the switched nanomagnet allows it to overcome the shape anisotropy energy and flip its magnetization. This 'reversed' magnetization state persists even after the acoustic wave has propagated and is no longer straining these nanomagnets. Magnetic Force Microscopy (MFM) is used to characterize the nanomagnets' magnetic state before and after the acoustic wave clocking cycle is applied.

3.2 Energy matrices for different dimension of nanomagnets

We provide detailed energy matrices calculations to show the choice of dimensions where the nanomagnets' volume suffices to produce the stress anisotropy energy that along with the dipole coupling energy overcomes the shape anisotropy energy and switches the magnetization. Tables T1 to T4 shown below summarize the energy calculations for different nanomagnet dimensions. The shape anisotropy energy is calculated as

$$E_{Shape} = 0.5 \; \mu_0 \; M_s^2 \; V \; (N_{d\text{-}long} - N_{d\text{-}short}), \tag{3.1}$$

where $\mu_0 = 4\pi \times 10^{-7}$ N/A, $M_s = 1.422 \times 10^6$ saturation magnetization of Cobalt, V is the volume of each nanomagnet, $N_{d\text{-}long}$ and $N_{d\text{-}short}$ correspond to the demagnetization factor along long and short axis of the ellipse, respectively.

The dipole interaction energy of each magnet with a highly shape anisotropic dipole coupled magnet of dimension 400 nm x 150 nm x 12 nm is

$$E_{Dipole} = ((\mu_0/4\pi)\ M_s^2\ V\ V_{Dipole})/\ r^3, \tag{3.2}$$

where V_{Dipole} is the volume of the high shape anisotropy magnet, V is the volume of the low shape anisotropy magnet whose magnetization is being switched, r is the center to center distance between these magnets.

The stress anisotropy energy due to strain transfer from the acoustic wave is

$$E_{Stress} = Strain\ (Y)\ (\lambda)\ V, \tag{3.3}$$

where strain is 142 ppm, Y is the young's modulus for Cobalt= 209 GPa, λ is the magnetostriction of cobalt = -50 ppm and V is the volume of each nanomagnet.

*Table 3.1: **Energy matrix for different aspect ratios of nanomagnets with major axis 200nm***

	200x125 nm²	200x135 nm²	200x145 nm²
E_{Shape}(eV)	68.099	61.4236	53.7172
E_{Dipole} (eV)	49.8251	44.3390	43.4239
E_{Stress}(eV)	2.2059	2.3824	2.5589
[E_{Dipole}+E_{Stress}-E_{Shape}] (eV)	-16.068	-14.7022	-7.7344

Table 3.2: Energy matrix for different aspect ratios of nanomagnets with major axis 250 nm

	250x175 nm²	250x185 nm²	250x195 nm²
E_{Shape}(eV)	72.116	64.0351	55.2993
E_{Dipole} (eV)	50.4595	45.3558	40.9890
E_{Stress}(eV)	3.8604	4.0810	4.3016
[E_{Dipole}+E_{Stress}-E_{Shape}] (eV)	-17.7961	-14.5983	-10.0087

Table 3.3: Energy matrix for different aspect ratios of nanomagnets with major axis 300 nm

	300x230 nm²	300x240 nm²	300x250 nm²
E_{Shape}(eV)	69.9338	60.8590	51.3615
E_{Dipole} (eV)	50.1157	45.4828	41.4629
E_{Stress}(eV)	6.0884	6.3531	6.6178
[E_{Dipole}+E_{Stress}-E_{Shape}] (eV)	-13.7298	-9.0231	-3.2808

Table 3.4: Energy matrix for different aspect ratios of nanomagnets with major axis 340 nm

	340x260 nm²	340x270 nm²	340x280 nm²
E_{Shape}(eV)	79.8467	70.8256	61.4205
E_{Dipole} (eV)	64.2062	66.6756	56.2175
E_{Stress}(eV)	7.8002	8.1002	8.4002
[E_{Dipole}+E_{Stress}-E_{Shape}] (eV)	-7.8403	3.9502	3.1972

It can be noticed from these tables that only for the dimension 340 nm x270 nm and 340 nm x280 nm, the combination of dipole and stress energies is slightly over shape energies. These

calculations were the blueprint for the actual dimensions of the nanomagnets used for the experimental studies.

3.3 Schematic design

Dipole-coupled elliptical Co nanomagnets - one of dimensions ~ 400 nm x 150 nm x 12 nm termed the input nanomagnet (I) and the other of dimensions 340 nm $\times$ 270 nm $\times$ 12 nm termed the output nanomagnet (O) were fabricated on a 128° Y-cut lithium niobate substrate.

(a)   **(b)**   **(c)**

(d)
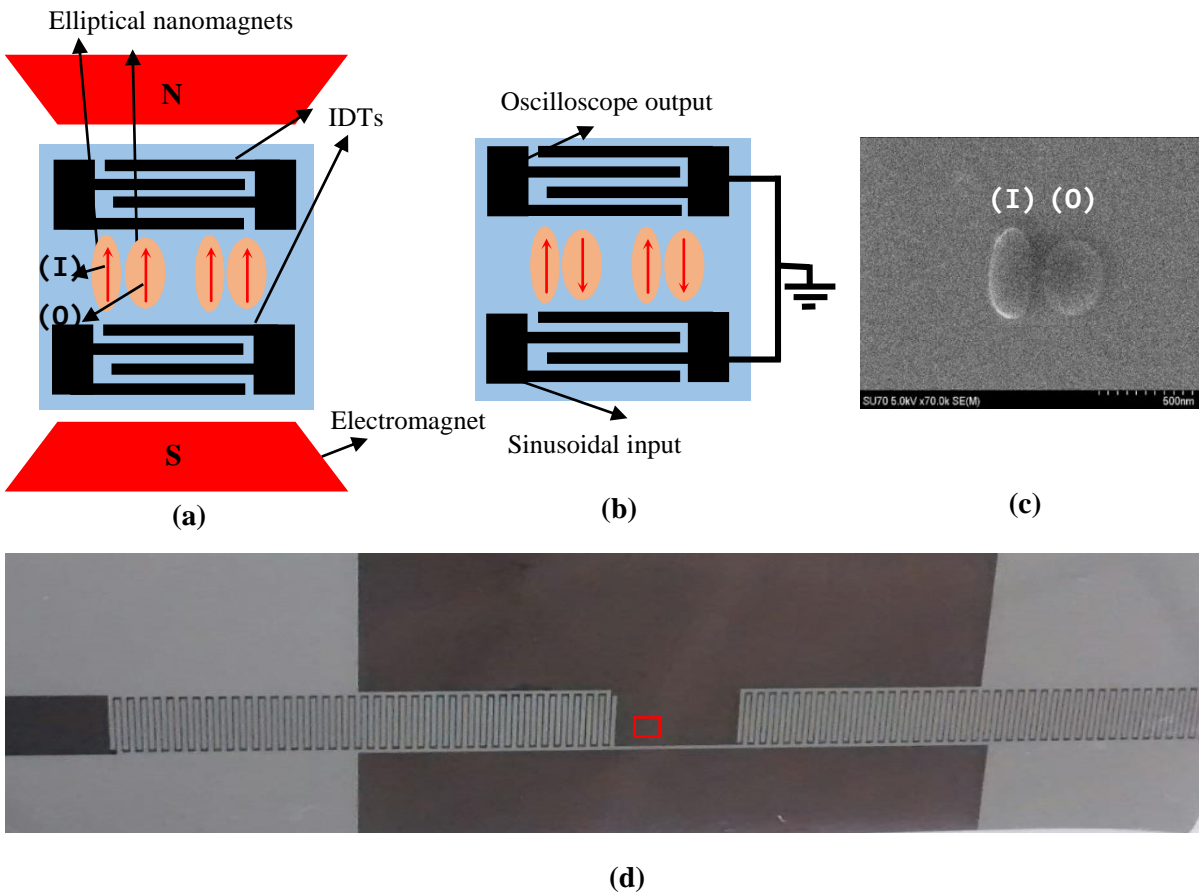
Fig. 3.1: (a) Schematic of experimental set-up with initial application of an external magnetic field on the nanomagnets. The red arrows indicate the direction of the magnetization state of the nanomagnets. (b) Upon acoustic wave propagation, a mechanical strain is generated and transferred to the nanomagnets which reverses the magnetization of the lower shape anisotropy nanomagnets (O). (c) SEM micrograph of the dipole coupled nanomagnets with nominal dimensions of 400 nm $\times$ 150 nm $\times$ 12 nm (I) and 340 nm $\times$ 270 nm $\times$ 12 nm (O). (d) Optical image of the lithium niobate substrate with the fabricated IDTs. The red rectangle highlights the region containing the nanomagnets in the delay line.

Note that the input nanomagnet is much more shape-anisotropic than the output nanomagnet, so that the input nanomagnet is "hard" (stress does not affect it) while the output nanomagnet is "soft" (stress can flip its magnetization). The wavelength of the acoustic wave is set to be 800 µm. This is to ensure that the wavelength is large enough that the strain across the nanomagnets is uniform. The interdigitated transducers (IDTs) are a comb-like arrangement of rectangular aluminum bars of thickness 300 µm and gap of 100 µm. The pitch of the IDTs is 400 µm which is exactly half the value of the intended acoustic wave wavelength.

Elliptical nanomagnets are delineated in the delay line, as shown in FIG. 3.1d. The pairs of nanomagnets of nominal dimensions (340 nm × 270 nm × 12 nm) and (400 nm × 150 nm × 12 nm) are initially magnetized along the major axis with a large external magnetic field of ~0.2 Tesla (FIG. 3.1a) and characterized by MFM (FIG. 3.2 a). Mechanical strain is applied by applying a sinusoidal voltage of 50 V_{p-p} between the IDTs (FIG. 1d) at a characteristic frequency.

3.4 Results

Assuming that maximum strain is completely transferred to the multiferroic nanomagnet, the maximum stress applied to the elliptical Co nanomagnets is 30 MPa. During this stress (voltage) application, each nanomagnet experiences cycles of tensile and compressive stress (± 30 MPa) along its major axis. We note that multiple cycles of acoustic waves pass through the nanomagnets, and not just a singular pulse. Since cobalt has negative magnetostriction, the tensile stress on the lower shape anisotropic nanomagnet (340 nm × 270 nm × 12 nm) results in magnetization rotation towards the minor axis. This is because stress anisotropy shifts the potential

energy minimum to an orientation that is perpendicular to the stress axis. The stress needed for such a rotation is likely to be smaller if there is incoherent rotation compared to strictly coherent single domain magnetization rotation.

The higher shape anisotropic nanomagnets (400 nm × 150 nm × 12 nm) have a greater shape anisotropy energy barrier which the stress anisotropy is unable to beat. As seen in the MFM image of FIG. 3.2b, after acoustic wave propagation, the magnetization state of the nanomagnets having lower shape anisotropy energy barrier (O) [on the right] switches by 180° due to the dipole

Pre-acoustic wave **Post-acoustic wave**

Input (I)   **Output (O)**

Acoustic wave

(a)   (b)
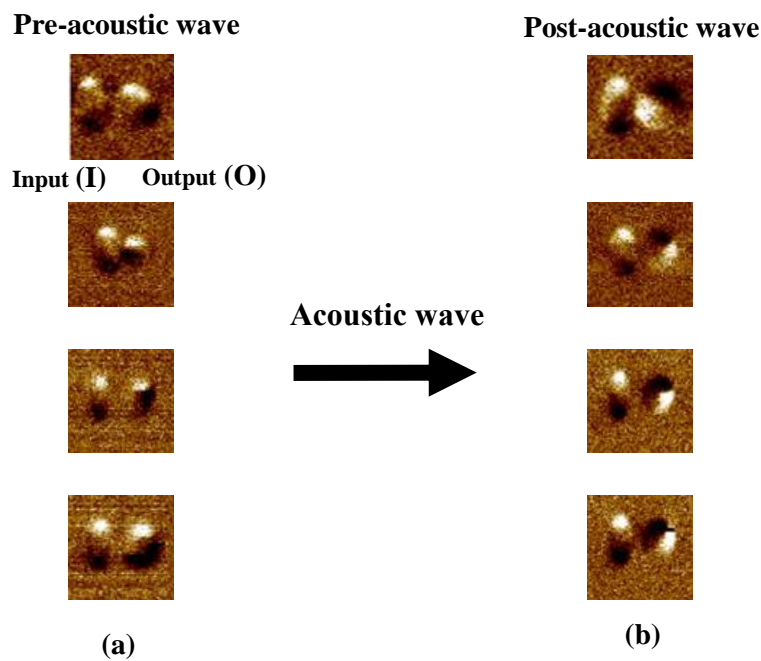
Fig. 3.2: MFM images of four distinct nanomagnet pairs. (a) Pre-stress (pre-acoustic wave) magnetization state. (b) Post-stress (post-acoustic wave) magnetization state. The lower shape anisotropic nanomagnets (O) clearly show a magnetization rotation of 180°.

interaction with the higher shape anisotropic nanomagnet (I). This nanomagnet remains in this 'reversed' state even upon removal of the acoustic wave. No nanomagnet that we studied under the influence of the dipole coupling settled into a vortex state proving that the initial (before acoustic wave) and final (after acoustic wave) states are always single domain states. Thus, the

acoustic wave has triggered the operation of the NOT gate where each individual nanomagnet's single domain magnetization state ("up" or "down") encode the binary logic state ("0" or "1").

3.5 Discussions

3.5.1: Magnetic Force Microscopy (MFM) scans to demonstrate repeatability

The images shown in top two rows in FIG. 3.3 are MFM phase images of the two bottom nanomagnets shown in FIG. 3.2. Here we confirm that on application of a magnetic field they can reset to the initial state. The next two sets of images (row 3 and 4) show different nanomagnets where we not only show the "reset" after the switching but also demonstrate that the entire switching sequence is repeatable.

To establish repeatability and to 'reset' the magnetization of the nanomagnets to the original pre-stress magnetization state, a large external magnetic field of 0.2 Tesla is applied along the major axes of the nanomagnets as shown in FIG. 3.1a. The MFM images of exactly the same nanomagnets after this 'reset' step are shown in FIG. 3.3c. The images clearly show that the single domain pre-stress state (before the acoustic wave is applied) of the magnetization has been restored since the images in FIG. 3.3c are nearly identical to those in Fig. 3.3a.

Acoustic wave (AW) is again applied as shown in Fig. 3.1b. The magnetization of the bottom nanomagnets are again reversed. The resulting MFM images are shown in Fig. 3.3d. The images clearly show that the magnetization again goes into same reversed state since the images in Fig. 3.3d are nearly identical to those in Fig. 3.3b.

Fig. 3.4 shows MFM images of two different pairs of nanomagnets which have the same shape as magnets in 3.3. Unlike the acoustic wave applied to magnets shown in 3.3, where the wavelength was 800 μm, the applied acoustic wave wavelength was 1600 μm in this case.
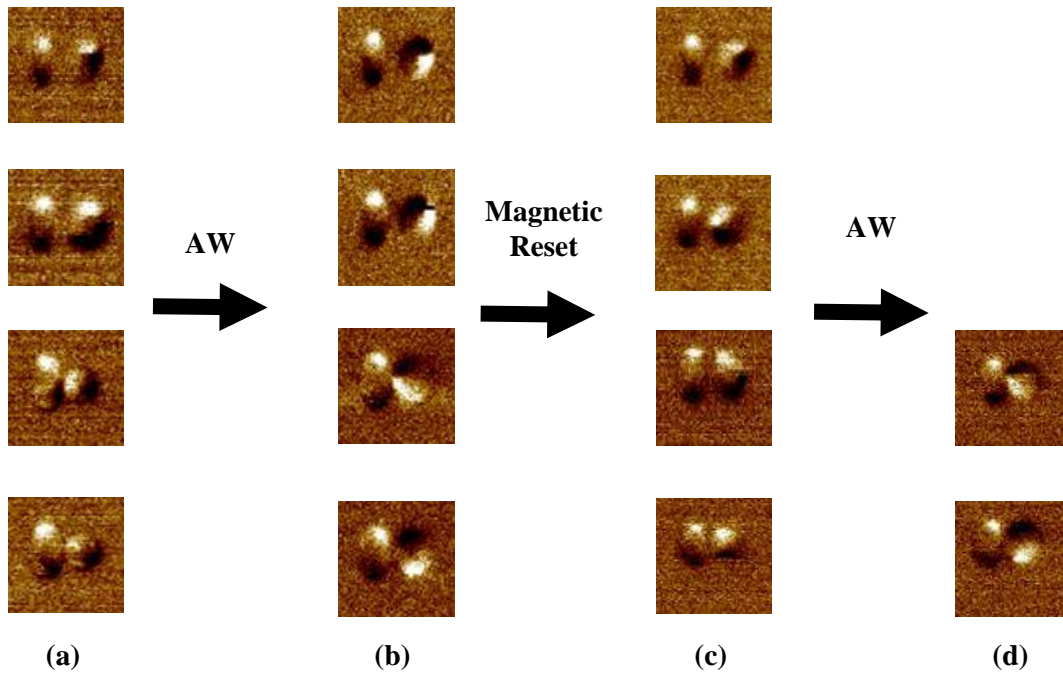
Fig. 3.3: MFM images of 4 dipole coupled nanomagnet pairs in the: (a) Pre-stress state before AW application. (b) Post-AW images. (c) The third column shows MFM images taken after magnetization of the nanomagnet pair is reset with a magnetic field. (d) This is the post AW images when AW is applied to nanomagnets.

Fig. 3.4 shows the same kind of repeatability and MFM scans as Fig. 3.3. Since, the wave dwells on the nanomagnet for sufficient time in the former case, additional dwell time in the latter case causes no significant difference in switching behavior.
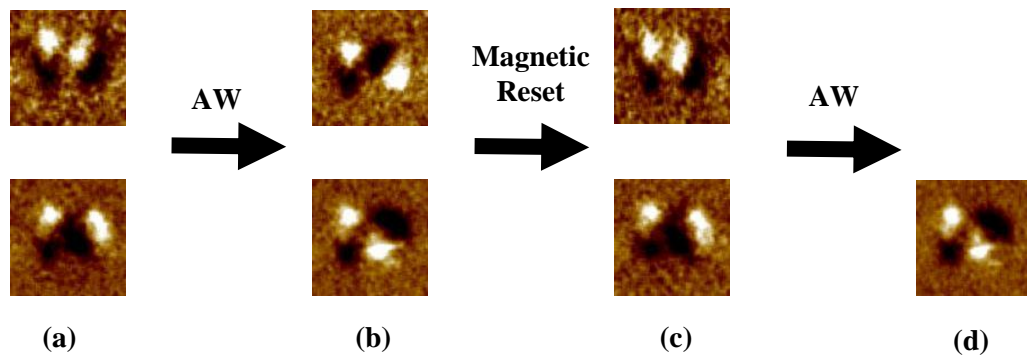
Fig. 3.4: Two sets of dipole coupled magnets where applied AW wavelength is doubled.

3.5.2 Electrical characterization of IDTs

The Figs. 3.5 (a) and (b) show the oscilloscope image when sinusoidal and square wave voltage respectively are applied to the IDTs fabricated on glass. There is no transmission as expected for a glass substrate.

The Figs. 3.6 (a) and (b) show the oscilloscope images of sinusoidal and square wave voltage respectively that are applied to the IDTs fabricated on Lithium niobate. It can be clearly seen that the receiver IDTs on Lithium niobate show sinusoidal electrical signal and the peak-peak voltage of this signal is almost equal to that applied to the transmitted IDTs, thus proving no significant loss of amplitude in the delay line. We also note that the output voltage in Fig. 3.6 (b) is sinusoidal, even though the applied voltage is a square wave. Thus, the acoustic wave device acts as a filter when the applied voltage has the characteristic frequency of the device, as discussed in literature.
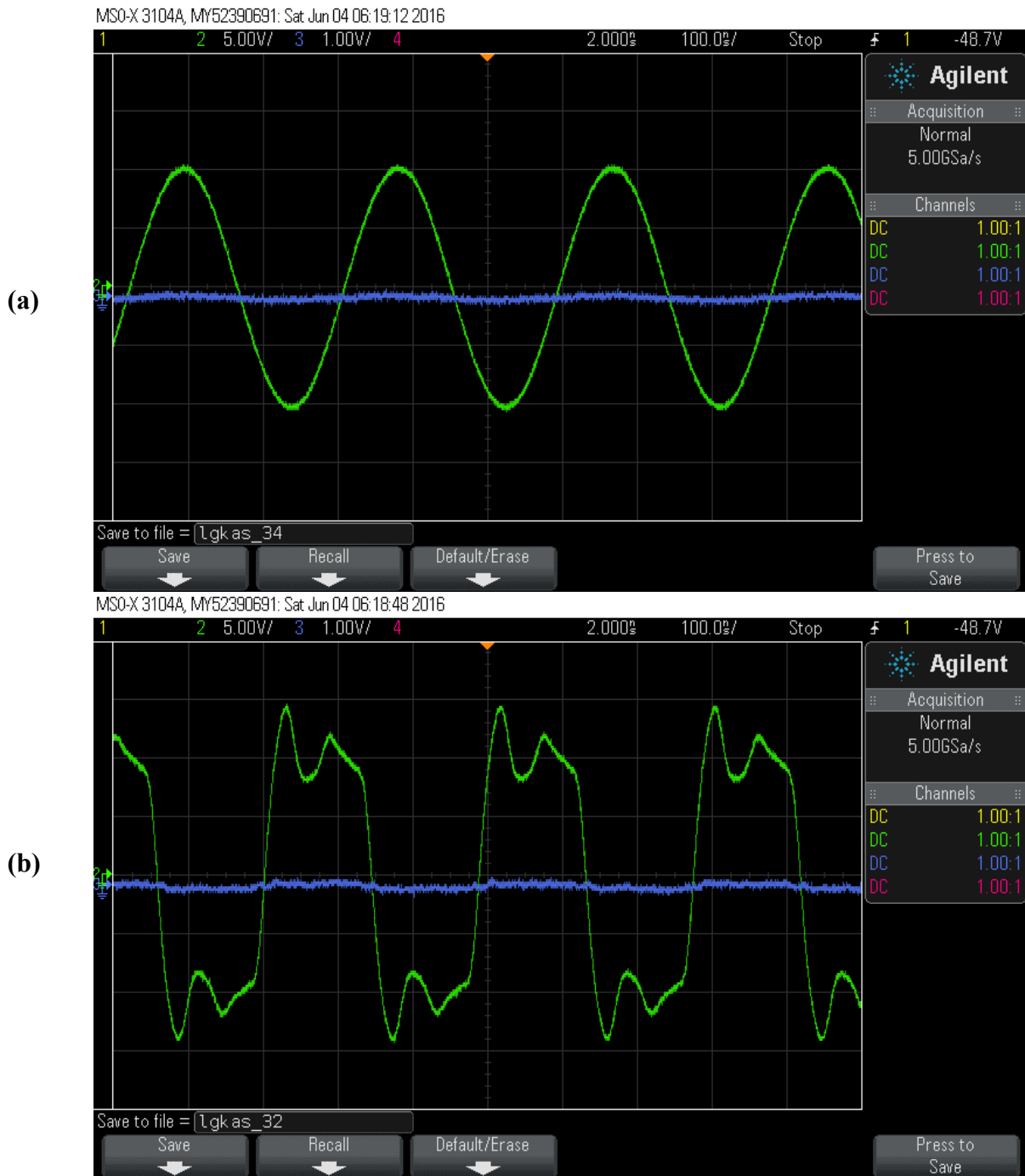
Fig. 3.5: (a) Sinusoidal voltage applied to input IDT on Glass. (b) Square wave applied to input IDT on Glass. The input is shown in green. The output from receiver IDT is in blue. Shows NO transmission as expected.
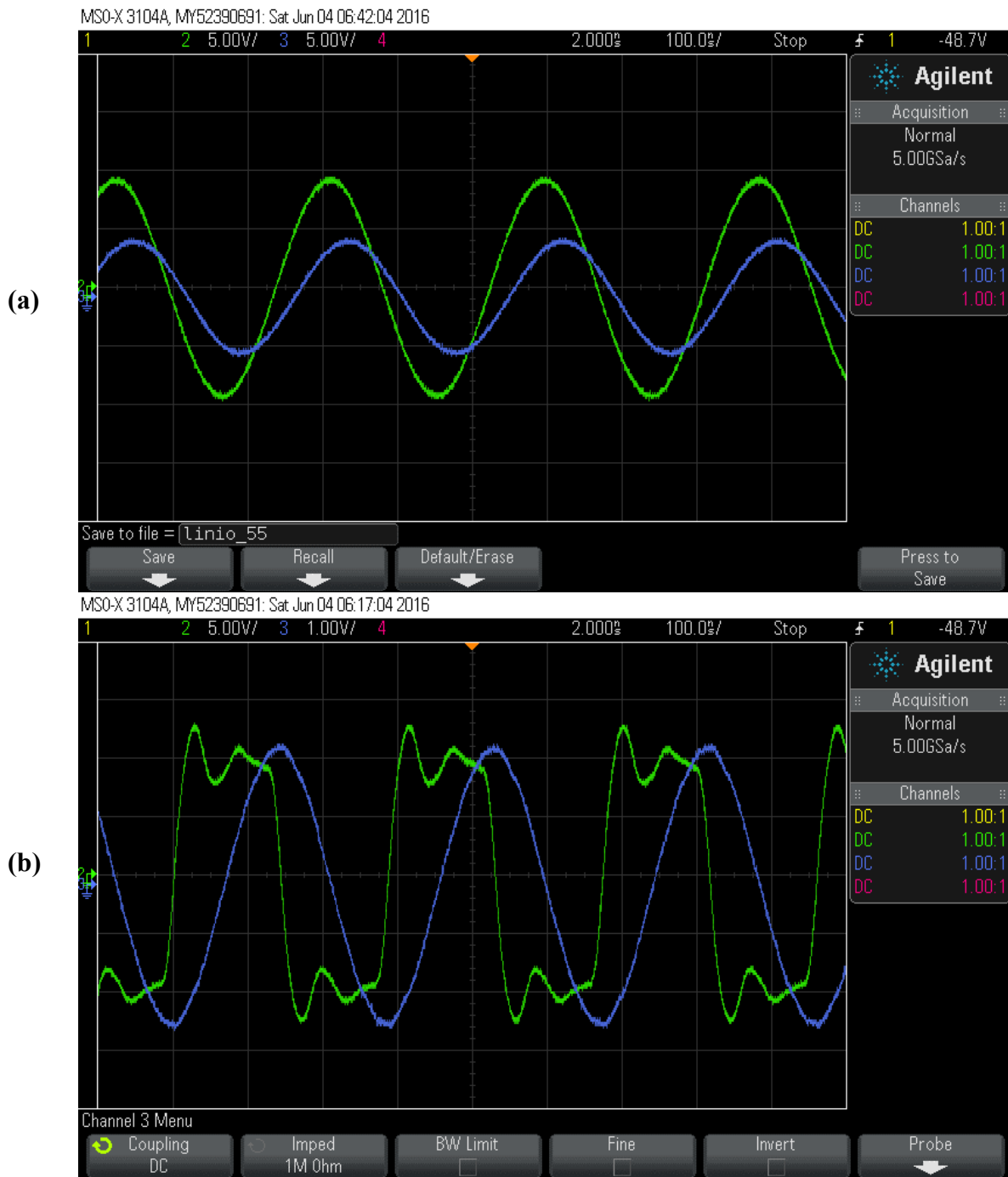
Fig. 3.6: (a) Sinusoidal voltage applied to input IDT on Lithium Niobate. (b) Square wave applied to input IDT on Lithium Niobate. The input is shown in green. The output from receiver IDT is in blue. Shows large transmission.

3.6 Conclusion

In conclusion, we have shown that acoustic waves, generated by IDTs fabricated on a piezoelectric lithium niobate substrate, can be utilized to induce 180° magnetization switching in dipole coupled elliptical Co nanomagnets. The magnetization switches from its initial single-domain 'up' state to a single-domain 'down' state after tensile/compressive stress cycles propagate through the nanomagnets. The switched state is stable and non-volatile. Furthermore, the acoustic wave energy amortized over all the nanomagnet pairs that can potentially fit in the delay could result in energy dissipation of the order of tens of attojoules per nanomagnet per clock cycle. These results show the feasibility of an extremely energy efficient acoustically clocked Boolean NOT gate.

Chapter 4: FMR study of FeGa films for determining dynamic parameters

4.1 Introduction

In chapters 2 and 3, we have experimentally demonstrated magnetization switching in isolated and dipole coupled nanomagnets, where strain is transferred using Surface Acoustic waves. Recently strain control of magnetization in isolated and dipole coupled Co and FeGa-alloy based nanomagnets (D'Souza, N. 2016; Ahmad, H, 2016; Atulasimha and Bandyopadhyay, 2015) was demonstrated. The use of FeGa alloys attract great interest as they exhibit ~300 micro-strain magnetostriction (in bulk) without containing rare earth elements (Clark *et. al.*, 2003), at the same time much higher than non-rare earth elements such as Co which exhibits ~50 micro-strain magnetostriction (in bulk). Potential use of FeGa alloys in SAW based memory and Logic devices could lead to higher switching statistics (not discussed here) due to their higher magnetostriction. In order to transition from quasistatic application of magnetostriction and villari effect to dynamic magnetoelastic control of magnetization in these FeGa alloys (in the nanoseconds time scale where the magnetization dynamics becomes extremely important), we need to better understand the dynamic properties of FeGa, including the exchange stiffness and the Gilbert damping. Recent work has explored the Gilbert damping (Parkes et. al. 2013) in a single 21 nm thick epitaxial FeGa film and exchange constant (Tacchi *et. al,* 2014) in a 65 nm thick FeGa film. However, since magnetostrictive nanomagnetic elements for computing applications would typically involve ~10 nm thick FeGa with lateral dimensions ~100 nm, it is technologically important to understand how the dynamic properties vary while scaling down to these relevant length scales. In this chapter, we present a ferromagnetic resonance (FMR) study of the Gilbert damping and exchange stiffness values for FeGa continuous films between 20 nm and 80 nm thick.

4.2 FMR principles

If a magnetic field is applied on a series of magnetic moments, they will tend to line up parallel to the field, because they will minimize their zeeman energy by doing so. If, in this configuration, the magnetic moments are taken out from this equilibrium stage, they will try to go back to it through the torque produced by the magnetic field. In a real ferromagnetic system, a damping term must be added to this "equation of motion", to describe correctly the behaviour of the magnetic moments involved. For example, Landau Lifshitz Gilbert (LLG) equation considers the damping in the following way:

$$\frac{dM}{dt} = -\gamma \left[M \times (H + H_{eff}) \right] + \frac{\alpha}{\gamma M^2} \left(M \times \frac{\partial M}{\partial t} \right) \tag{4.1}$$

with the externally applied DC magnetic field H, H_{eff} the effective magnetic field which includes the driving rf-microwave magnetic field $h(t)$ of frequency $\omega/2\pi$, the demagnetizing field, the magnetocrystalline anisotropy field; $\gamma = g\mu B / h$ where γ is the gyromagnetic ratio, g is the electron spin g-factor, h is the Planck's constant, and G the phenomological Gilbert damping parameter.

LLG equation describes the damped motion of a magnetic moment about the direction of an external magnetic field.
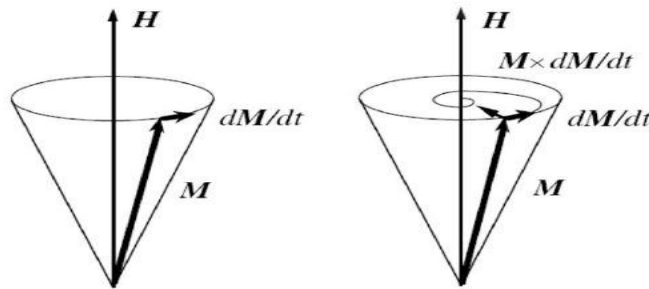
Fig. 4.1: Magnetization dynamics with damping

In a typical experimental arrangement the ferromagnetic specimen is in the form of a thin sheet or foil, which is employed as one wall of a rectangular cavity terminating a wave guide fed by a microwave generator. The ferromagnetic side of the cavity is chosen so that the magnetic vector of the microwave field is constant in the direction of the plane of the wall. A static magnetic field is applied (by means of an electromagnet) also in the plane of the wall but perpendicular to the microwave magnetic field. If a varying force perpendicular to **H** is applied over the magnetic moment (like a radio frequency (RF) electro-magnetic signal), it can make the magnetization **M** precess about the equilibrium direction. Besides, if this force has a frequency similar to the precessional frequency of **M** , that we will call ω_0 , a maximum of energy absorption by the ferromagnetic sample will be observed. This is when ferromagnetic resonance is taking place, and all magnetic moments will be oscillating in phase. It is found experimentally that the energy loss in the cavity goes through a maximum as the strength of the static magnetic field is increased (Kittel, C., 1948).

There are several approaches used to determine the resonance frequency from the LLG equation. The Kittel equation for ferromagnetic resonance governs the relationship between microwave excitation frequency and resonant applied magnetic field for fields applied in the plane (Kittel, 1948):

$$\left(\frac{2\pi f}{\gamma}\right)^2 = \mu_0^2\left(H_{res} + H_{ip}\right)\left(H_{res} + H_{ip} + H_K + M_s\right) \tag{4.2}$$

where γ is the gyromagnetic ratio, μ_0 is the vacuum permeability, H_{ip} reflects the in-plane magnetic anisotropy, H_K reflects the uniaxial magnetic anisotropy, and M_S is the saturation magnetization.

Furthermore, the estimate for the dimensionless Gilbert damping parameter, α is obtained by fitting the linear frequency dependence of measured resonance linewidth ΔH:

$$\Delta H = \frac{4\pi\alpha f}{\gamma\mu_0} + \Delta H_0 \tag{4.3}$$

where ΔH_0 is the inhomogeneous linewidth broadening.

4.3 Sample preparation and setup

We deposit Ta (10 nm)/FeGa (δ)/Ta (10 nm) layers on 500 μm thick silicon wafers by dc magnetron sputtering in a chamber with a base pressure of less than 4 x 10^{-8} Torr. Here δ= 20nm, 40 nm, 60 nm and 80 nm of FeGa thickness. The FeGa targets have a stoichiometry of 81% Fe and 19% Ga. Ta was used as capping layer. The wafers were spin-coated with approximately 150 nm of PMMA resist to avoid electrical shorting with the coplanar wave guide. About 5 mm x 5mm pieces were cleaved wafers were cleaved for each thickness to be tested on the FMR setup.
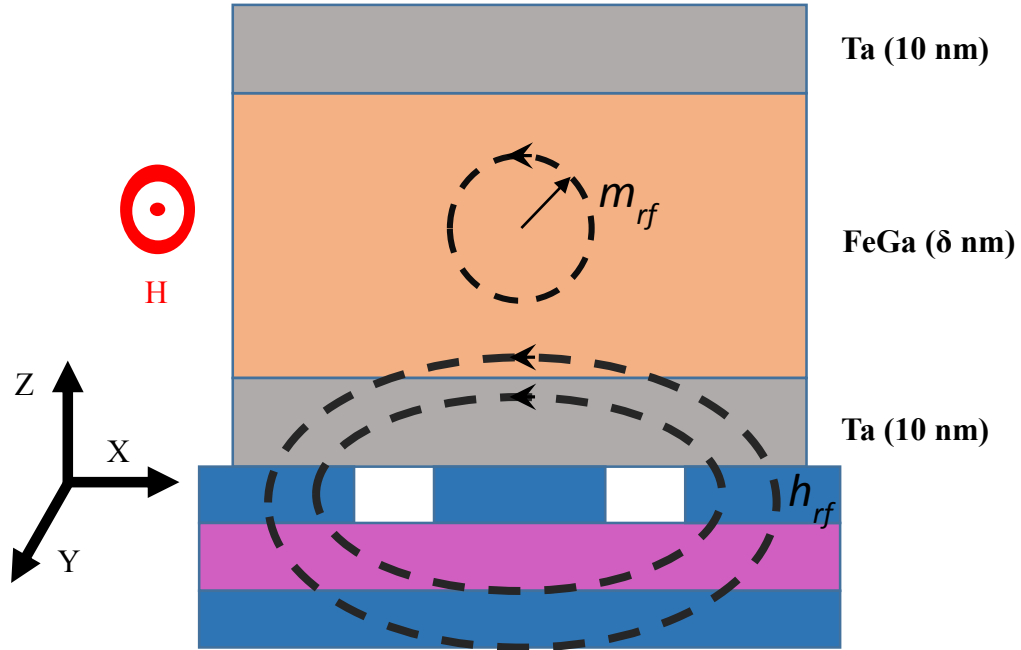
Fig. 4.2: Schematic of the experimental setup for broadband ferromagnetic resonance. The trilayer is placed film-side down onto a grounded coplanar waveguide with a fixed frequency microwave magnetic field, h_{rf} along the x direction. Additionally, there is an applied in–plane field H along the y–axis. By varying H, the dynamic magnetization m_{rf} is brought into resonance with h_{rf} (Gopman $et. al.$, 2016).

The dynamical properties were studied using broadband ferromagnetic resonance spectroscopy, schematically depicted in Fig. 4.1. At fixed microwave excitation frequencies between 10 GHz and 50 GHz, we sweep the applied in–plane magnetic field and record the position of Lorentzian–shaped absorption modes (Gopman *et. al.*, 2016).

4.4 Results

An excitation field collinear to the dc magnetic field is generated for lock-in detection of the differential absorption versus applied magnetic field (Fig. 1.11) The 0th ferromagnetic resonance mode is obtained by fitting the absorption data to a sum of Lorentzian curves. (Schoen *et. al.,* 2015*)*. To get the experimental points, for several values of *H*, a Lorentzian fit was performed to find where the crossing point of the absorption derivative is (Fig. 1.11 inset), and therefore find the resonance field at different frequencies.

Figures 4.3 to 4.6 show (a) Inplane frequency vs. resonant static field and (b) In plane line width vs. resonant frequency. Using equation 4.2, these plots in (a) are used to determine H_{ip} and M_{eff} ($=H_k + M_s$). Using equation 4.3 these plots in (b) are used to determine dimensionless gilbert damping parameter α and ΔH_0. The line width in figure (b) in each case is obtained from the absorption vs static magnetic field curve.
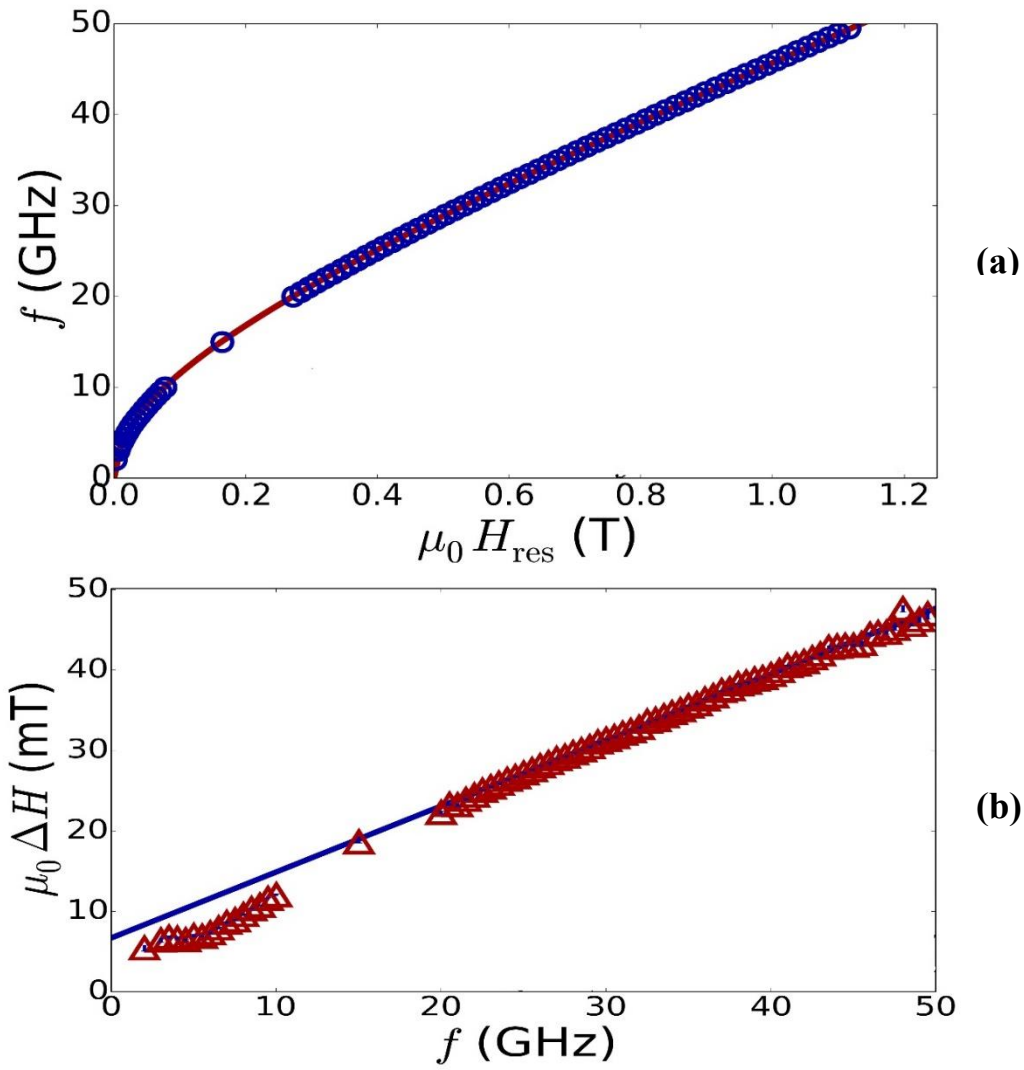
Fig. 4.3: 20 nm thickness FeGa film (a) In plane frequency vs resonant static field (b) Inplane linewidth vs resonant frequency. [Image source: Daniel Gopman, NIST Maryland]
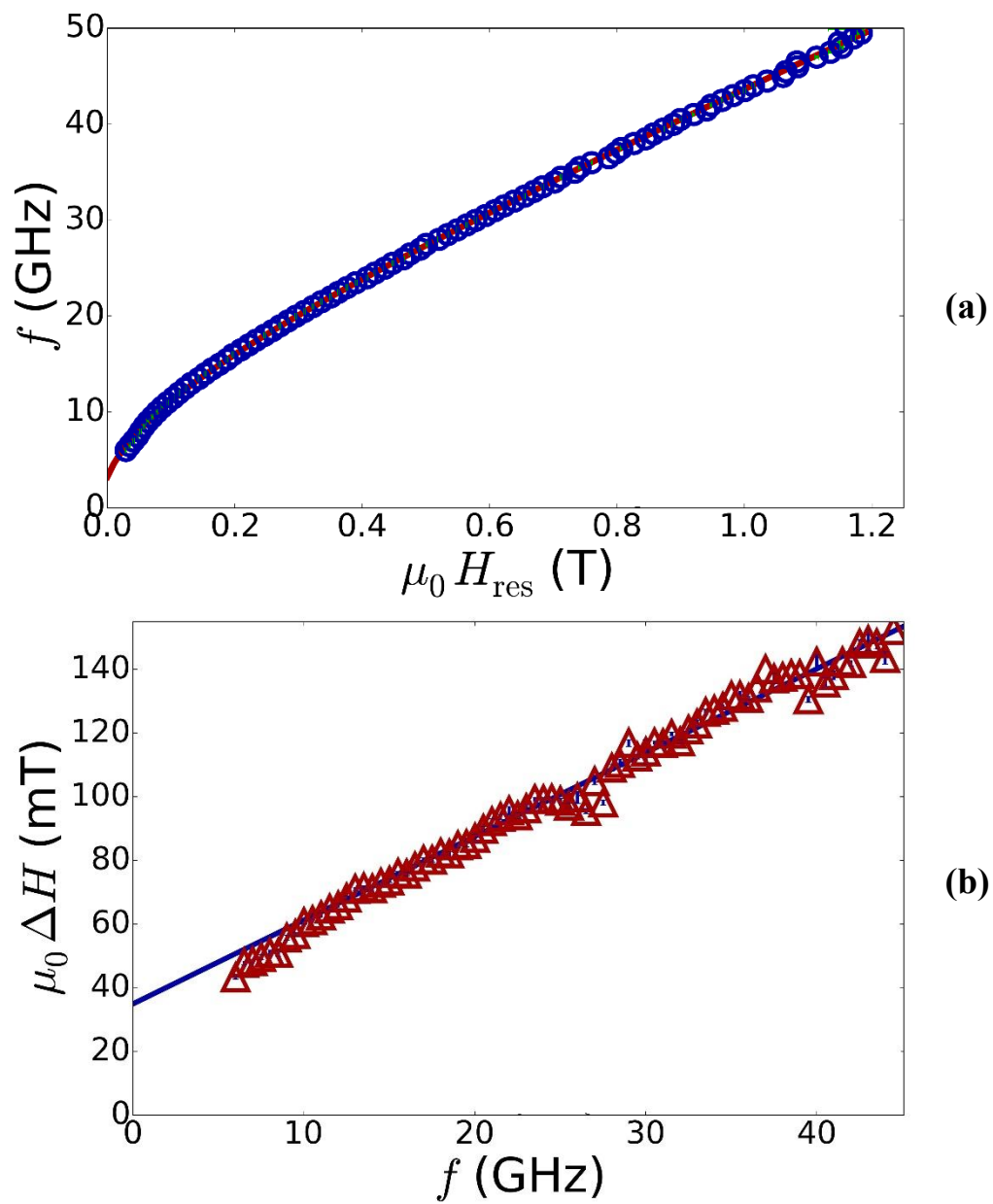
Fig. 4.4: 40 nm thickness FeGa film (a) In plane frequency vs resonant static field (b) Inplane linewidth vs resonant frequency.[Image source: Daniel Gopman, NIST.]

(a)

(b)
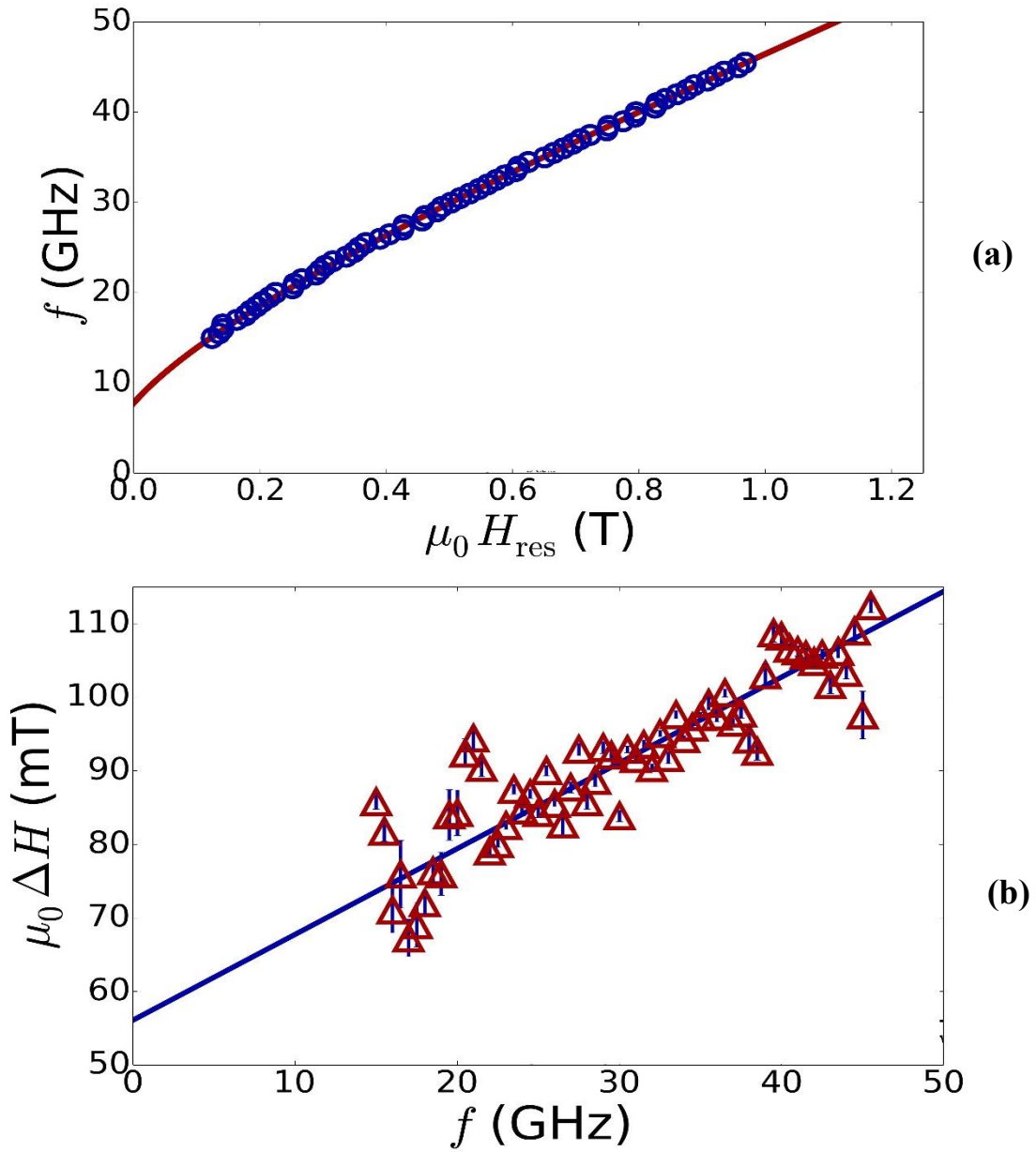
Fig. 4.5: 60 nm thickness FeGa film (a) In plane frequency vs resonant static field (b) Inplane linewidth vs resonant frequency.[Image source: Daniel Gopman, NIST, Maryland.]
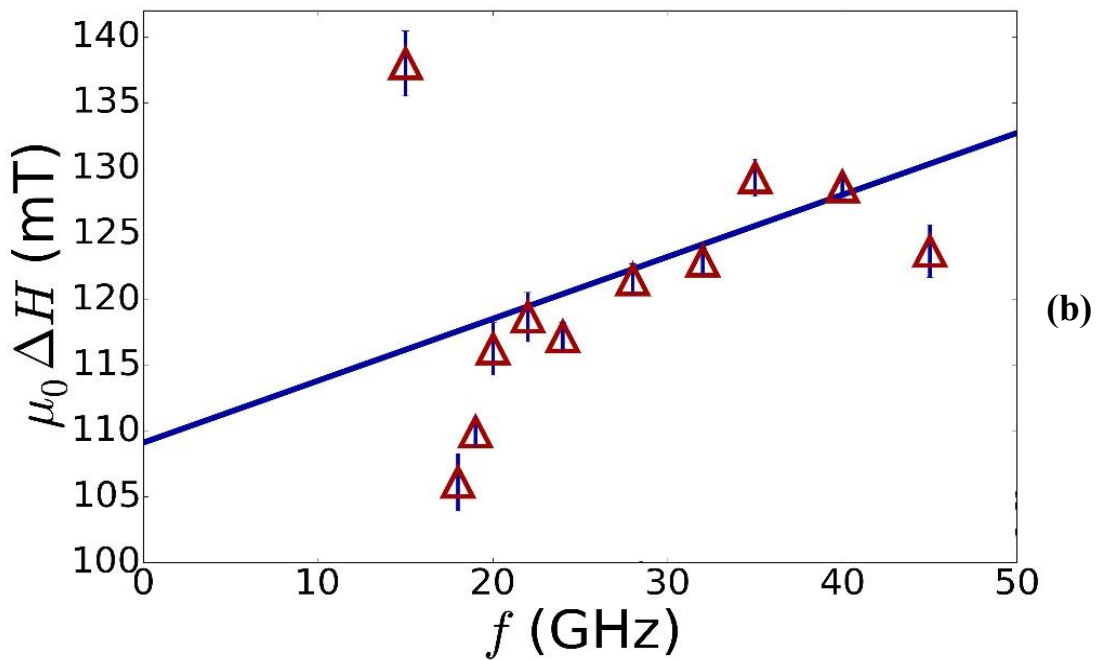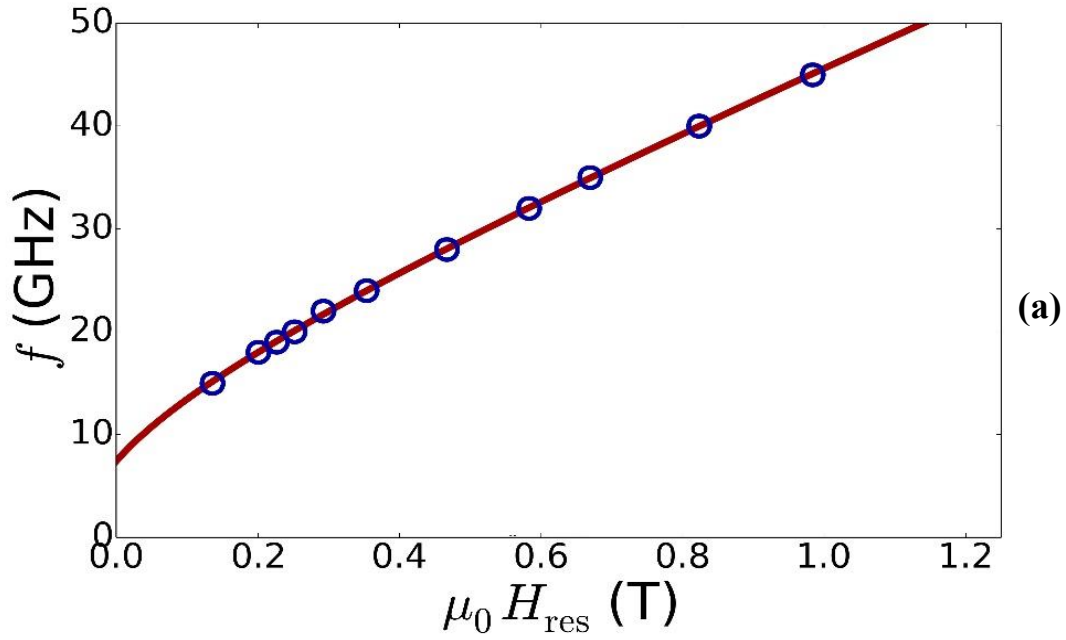
Fig. 4.6: 80 nm thickness FeGa film (a) In plane frequency vs resonant static field (b) Inplane linewidth vs resonant frequency.[Image source: Daniel Gopman, NIST, Maryland.]

4.5 Discussions

The table 4.1 shows the various parameters determined from the plots. The values marked with a star are not reasonable estimations due to unavailability of enough data.

Table 4.1: Ferromagnetic Resonance Spectroscopy Results for series of FeGa sputtered films. Table source: Daniel Gopman, NIST, Maryland

FeGa thickness (nm)	M_eff (T)	M_eff err (T)	H_cub (T)	H_cub err (T)	g	g (err)	Gilbert damping α	Gilbert damping err	dB linewidth (T)	dB linewidth err (T)
20	1.468	0.007	0.0005	0.0001	2.078	0.003	0.01193	0.00007	0.0067	0.0002
40	1.24	0.01	0.011	0.001	2.07	0.01	0.038	0.001	0.035	0.001
60	1.35	0.02	0.05	0.006	2.09	0.01	0.017	0.001	0.056	0.003
80	1.27	0.02	0.05	0.01	2.09	0.01	0.007*	0.003	0.109*	0.008

We notice that the Gilbert damping constant α, increases with thickness as the thickness increases from 20 nm to 60 nm. We disregard the Gilbert damping for 80 nm thickness since sufficient data wasn't available. For the 40 nm film, the value of α is abnormally high and it's likely that this can be due to several anomalies with the film growth process. Sometimes these films can form rectangular pillar structures leading to different cubic magnetic anisotropies than expected. Also, the stoichiometry of the film could easily be different from that of the target. If the amount of iron is more than 80%, that could lead to such anomalies too. It's important to be to carry out VSM to determine the saturation magnetization of these films and Energy dispersive X-Ray spectroscopy (EDS) to determine the stoichiometry of Fe and Ga in the alloys grown, to explain the anomalous α value for 40 nm film.

Figure 4.7 shown below is the compilation of differential absorption vs sweep of static magnetic field for different microwave frequencies for the 60 nm thickness sample. The plots in Fig. 4.5 are obtained by lorentzian fit of these curves to get resonant frequencies and linewidths. The same is true for all figures 4.3 to 4.6.
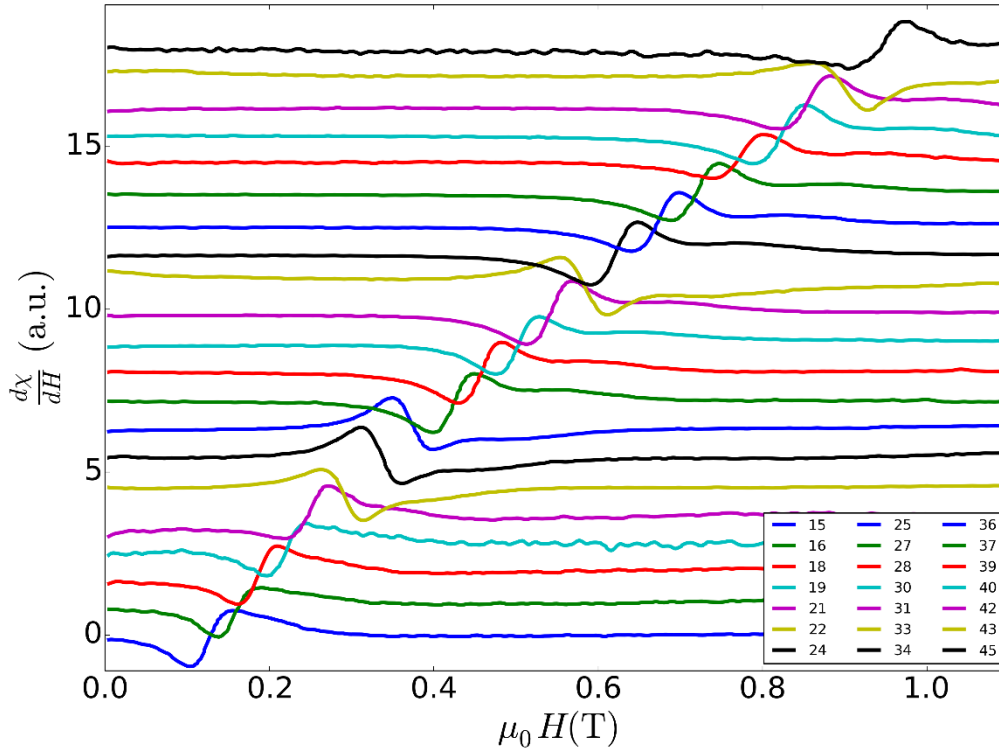
Fig. 4.7: Differential absorption vs applied field for FeGa thickness of 60 nm. The different colors show microwave frequency from 15 GHz to 45 GHz. [Image source: Daniel Gopman, NIST, Maryland.]

It can be seen in this figure that although the 0th mode is clearly visible it is hard to see the 1st Or 2

nd mode. These modes are called perpendicular standing spin wave mode (PSSW).

4.5.1 Determination of exchange constant.

Fig. 4.8 shows the in plane frequency vs. resonant static field for the 40 nm. The green line

the fit of the first PSSW mode. The red line is the same as one shown in figure 4.2 (a)

71
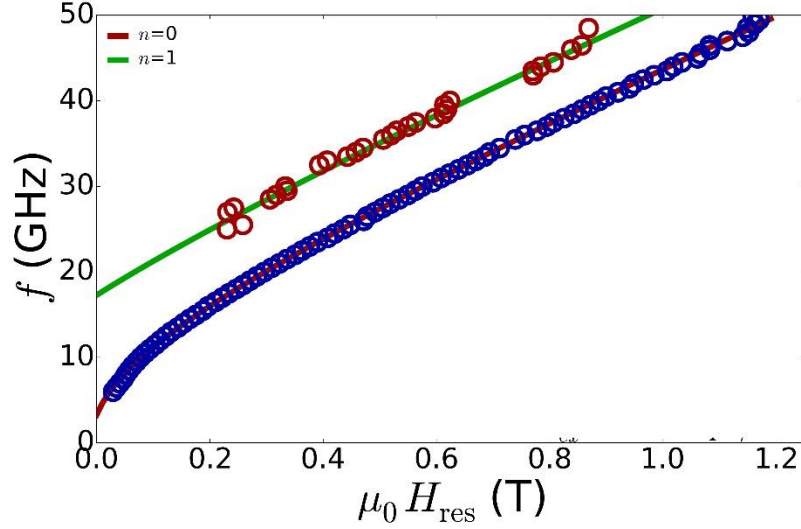
Fig. 4.8: Figure showing the in plane frequency vs. resonant static field for the 40 nm. The green line the fit of the first PSSW mode. The red line is the same as one shown in figure 4.2 (a). [Image source: Daniel Gopman, NIST, Maryland.]

Exchange stiffness can be estimated from the observation of, what appears to be, the first PSSW mode (Gopman *et. al.* , 2016). A nearly frequency independent shift (0.23 T) down to lower resonance field is seen between the most intense mode (0th mode) and a second absorption of lesser intensity. The following calculations were used to estimate the exchange field of the first mode.

$$\mu_0 \, H_{ex}^1 = \mu_0 H_0 - \mu_0 H_1 = 0.23 \, T$$

$$\mu_0 H_{ex}^1 = \frac{A_{ex} M_s}{2} k_1^2$$

since, $$k_1 = \frac{n\pi}{t} = \frac{1 * \pi}{t}$$

using $$M_s = 1000 \pm 10 \; \frac{kA}{m} \;\; \text{and} \; t = 40 \pm 4 \; nm$$

$$A_{ex} = 18 \pm 4 \, \frac{pJ}{m}$$

This value of A_{ex} compare reasonably well with 16 pJ/m (Tacci *et al.*, 2014). For such a value of the exchange stiffness, we expect that the next PSSW mode ($n = 2$) would be shifted down by approximately 0.93 T, which could explain why we see only one mode (n=1) in addition to the uniform mode (0th mode).

Since we are unable to obtain such frequency independent shift for other thicknesses, we need to perform more measurements to compare the value of exchange constant.

4.5.2 Energy Dispersive X-Ray spectroscopy Analysis of FeGa thin films.

To characterize the thin films for the stoichiometric composition of Iron and Gallium (Atomic percentages), energy Dispersive X-Ray spectroscopy (EDS) was carried out. Fig. 4.9 shows the Quantitative analysis for the 80 nm thick FeGa film deposited on a Silicon substrate. Since EDS gathers the spectrum of all elements present in the sample upto a thickness of 2 μm, the Fig. shows other elements too. Carbon and oxygen are impurities due the film being exposed to atmosphere before the analysis. A thin copper film was deposited as seed layer for the FeGa growth and hence its presence in the quantitative spectrum.

```
c:\edax32\genesis\genspc.spc
Label :
Acquisition Time  : 14:13:37        Date:17-Oct-2016

kV : 15.00   Tilt: 0.00   Take-off:24.79   AmpT : 12.8
Detector Type:SDD Apollo 10+       Resolution:137.32       Lsec 44

EDAX ZAF Quantification (Standardless)
Element Normalized
SEC Table : Default


Element    Wt %     At %   K-Ratio     Z        A        F
   C K    21.29    41.30   0.0258   1.0787   0.1121   1.0001
   O K     5.22     7.60   0.0127   1.0580   0.2288   1.0009
   CuL     4.05     1.48   0.0191   0.8690   0.5431   1.0028
   GaL     3.54     1.18   0.0191   0.8430   0.6381   1.0047
   SiK    50.76    42.11   0.4015   1.0084   0.7843   1.0002
   FeK    15.14     6.31   0.1339   0.8805   0.9962   1.0085
 Total   100.00   100.00
```

Fig. 4.9 EDS results for an 80 nm thick film on Si substrate.

It can be seen in the analysis that the ratio of Atomic percentages of Iron:Gallium is 6.31:

1.18. This translates to an 84.2 %:15.8 %, when all other elements are ignored. This is

encouraging since it proves that the film stoichiometry was very close to he intended ratio of

81%:19%. This quantitative analysis needs to be carried out for the 40 nm film too. That may

result in an explanation of the anomalous value of Gilbert damping constant α, in 40 nm film.

4.6 Conclusion

In this chapter, we obtain frequency vs. resonant field and line width vs frequency for four

different thicknesses of sputtered FeGa films using FMR. The latter plot gives us a trend of Gilbert

damping constant which can be explained only with further studies on saturation magnetization

and stoichiometry of the FeGa films of 20nm, 40 nm and 60 nm films.

We also are able to see the first PSSW mode on the 40 nm film which has a frequency independent shift on the differential absorption vs field plot. This plot is used to determine the exchange constant values which agrees with current literature. Further FMR studies need to be carried out to confirm this exchange constant value for other film thicknesses.

Chapter 5: Conclusion

In summary, the proof of concept for SAW switched memory device which is non-volatile and can be highly energy efficient, is demonstrated. The initial expectation was to see some isolated Co nanomagnets to show complete 180º rotation, on application of strain using SAW. However experimentally, it was noticed that the magnetic state breaks down into multiple domains and sets into a stable, 'vortex' state. This state is indicated by the four quadrant MFM images that is seen. Nevertheless, since the pre SAW single domain like magnetic state (bit '1') and the post SAW vortex state (bit '0') are stable and non-volatile, it leads to a conclusion that this work demonstrated the prelude to the implementation a successful memory scheme using "straintronics" implemented with SAW. It is also shown through calculations that the energy that'll be potentially expended in writing memory using SAW onto these nanomagnets will turn out to be only of the order of few tens of atto-Joules per element (nanomagnet). Thus making it highly energy efficient compared to current memory writing schemes.

When the same dimensions of nanomagnets are fabricated with higher shape anisotropic dipole coupled nanomagnets, these nanomagnets can be used to implement a Boolean NOT gate. The combination of strain generated by SAW and dipole coupling is enough to beat the shape anisotropy of the less shape anisotropic magnets and hence can lead to 180º switching of single domain magnetic states in the less shape anisotropic magnets.

A trend of Gilbert damping constant for 3 different thicknesses of FeGa film is obtained. The exchange constant for one such film is calculated and it agrees with recently observed values in films of similar thicknesses.

This research has several important outcomes in the pursuit of ultra-low power computing and lays foundation and acts as a proof of concept for future devices implementing 'straintronics' based on acoustic waves.. It has major technological importance because nanomagnetic logic clocked with strain could potentially be 1,000-10,000 times more energy-efficient than current CMOS logic at comparable clock speeds.

Finally, in the long run, the theoretical and experimental studies performed in this work can potentially open up unimaginable applications enabled when computing and information processing can be performed with such low power that these processors can be run from energy harvested from the ambient. Such a strain-clocked nanomagnetic processors that can be implanted, for example, in an epileptic patient's brain to monitor and process brain waves continuously to warn of an impending seizure. It will need so little power that it can potentially function by harvesting energy from the patient's head movements alone without ever requiring a battery. There are other applications such as in sensors embedded in structures (tall buildings, bridges) that continuously monitor fracture, material fatigue, etc. while running by harvesting energy from vibrations caused by wind or passing traffic. With the advent of Internet of Things it straintronic based processors can be used in wearables and wouldn't require any charging of the battery.

Appendix
(Information on simulations carried out by Dhritiman Bhattacharya)

The experimental results in chapter 2 are compared against theoretical predictions of magnetization dynamics computed with the MuMax simulation package. The dimensions of the elliptical Co nanomagnet used in our simulations are 340 nm × 270 nm × 12 nm and conform to the nominal dimensions of the experimentally fabricated nanomagnets. The evolution of the magnetization is investigated from its relaxed pre-stress state to a vortex state upon application of one cycle of tensile stress followed by compressive stress. This stress cycle replicates the stress applied on the nanomagnets during AW propagation.

The discretized cell size used in the MuMax simulations was 4 nm × 4 nm × 4 nm (which is smaller than the exchange length of Cobalt, $\lambda_{ex} \sim 5$ nm), implemented in the Cartesian coordinate system. Since there is no inherent mechanism of incorporating stress in the micromagnetic software package MuMax, the material's uniaxial magnetocrystalline anisotropy (K_1) is used instead, which is modeled using the following effective field due to the magnetocrystalline anisotropy,

$$\vec{H}_{anis} = \frac{2K_{u1}}{\mu_0 M_{sat}}(\vec{u} \cdot \vec{m})\vec{u} + \frac{4K_{u2}}{\mu_0 M_{sat}}(\vec{u} \cdot \vec{m})^3\vec{u} \tag{A.1}$$

where K_{u1} and K_{u2} are the first and second order uniaxial anisotropy constants, M_{sat} is the saturation magnetization, $\vec{u}$ and $\vec{m}$ are the unit vectors in the direction of the anisotropy and magnetization, respectively. Assuming $K_{u2} = 0$,

$$\vec{H}_{anis} = \frac{2K_{u1}}{\mu_0 M_{sat}}(\vec{u} \cdot \vec{m})\vec{u} \tag{A.2}$$

The effective field due to an applied external uniaxial stress, σ, is

$$\vec{H}_{stress} = \frac{3\lambda_s \sigma}{\mu_0 M_{sat}}(\vec{s} \cdot \vec{m})\vec{s} \tag{A.3}$$

where $(3/2)\lambda_s$ is the saturation magnetostriction, σ is the external stress and $\vec{s}$ is the unit vector in the direction of the applied stress. To simulate the effect of a uniaxial stress applied in the same direction as the uniaxial anisotropy, we equate $\vec{H}_{anis}$ with $\vec{H}_{stress}$ in order to determine the value of K_{u1}, as

$$K_{u1} = \frac{3\lambda_s\sigma}{2} \tag{A.4}$$

The magnetization dynamics are simulated using the Landau Lifshitz Gilbert (LLG) equation:

$$\frac{\delta\vec{m}}{\delta t} = \vec{\tau} = (\frac{\gamma}{1+\alpha^2}) \times (\vec{m} \times \overrightarrow{H_{eff}} + \alpha \times (\vec{m} \times (\vec{m} \times \overrightarrow{H_{eff}}))) \tag{A.5}$$

where m is the reduced magnetization (M/M_s), M_s is the saturation magnetization, γ is the gyromagnetic ratio and α is the Gilbert damping coefficient. The effective magnetic field (H_{eff}) is given by

$$\overrightarrow{H}_{eff} = \overrightarrow{H}_{demag} + \overrightarrow{H}_{exchange} + \overrightarrow{H}_{stress} \tag{A.6}$$

where, H_{demag}, $H_{exchange}$ and H_{stress} are the demagnetization (or magnetostatic) field, the effective field due to exchange coupling, and effective field due to stress anisotropy, respectively. These are evaluated in theMuMax framework as reported by Vansteenkiste et al.[31] For material parameters, typical values for cobalt are used: exchange stiffness A = 2.1×10^{-11} J/m, saturation magnetization M_s = 1.42×10^6 A/m, Gilbert damping constant α = 0.01, magnetostrictive coefficient $(^3/_2)(\lambda_s)$ = -50 ppm.

The results of the MuMax micromagnetic simulations for an elliptical Co nanomagnet of dimensions $340\,\text{nm} \times 270\,\text{nm} \times 12\,\text{nm}$ subjected to a tensile/compressive stress cycle are illustrated in Figure 3. The initial magnetization state of the nanomagnets is set to the ($\uparrow$) direction along the major axis. However, when the spins are allowed to relax, the magnetization states settle to the configuration as shown in Figure 3a which shows that not all the spins point along the major axis (as in a perfect single-domain state) and there is some deviation around the edges. Note that the counter-clockwise orientation of the spins in the vortex state is due to the initial conditions applied in our simulation. If the initial magnetization state was such that the pre-stress relaxed state settled
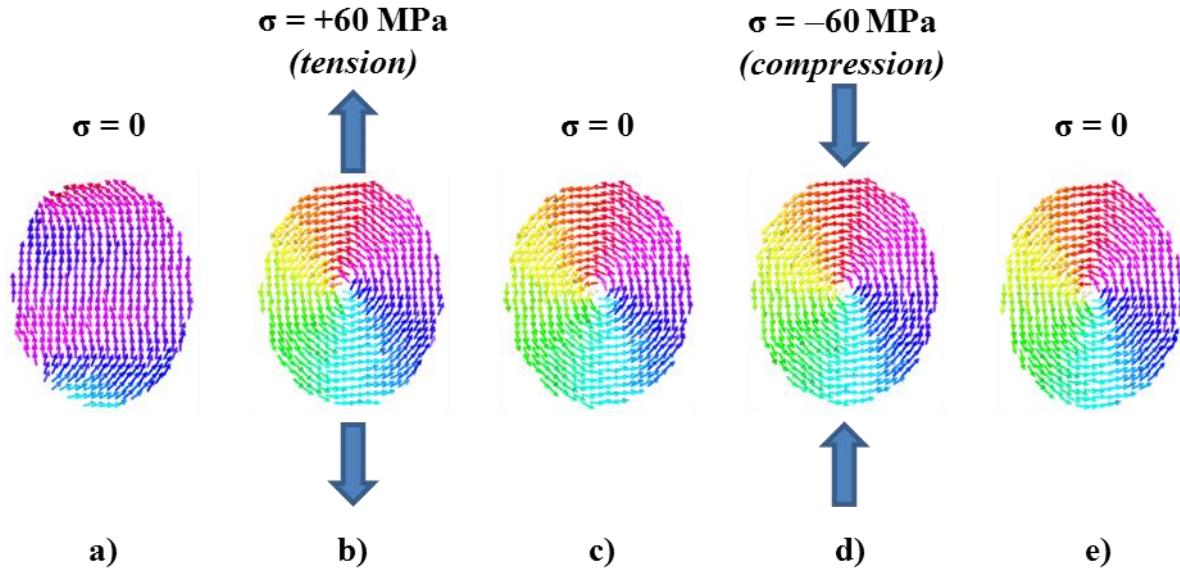
Figure A1: Micromagnetic simulations of a nanomagnet with dimensions of $340\,\text{nm} \times 270\,\text{nm} \times 12\,\text{nm}$ for the following scenarios: a) Relaxed pre-stress state, b) Tensile stress of +60 MPa, c) Post-stress at 0 MPa, d) Compressive stress of -60 MPa, and e) Post-stress at 0 MPa.

to where the spins had a small component in the clockwise direction, this would give rise to a clockwise vortex state.

Next, when the sinusoidal stress cycle is applied to the nanomagnet, the magnetic state transforms

to a 'vortex' state at a tensile stress of ~ +60 MPa (Figure 3b) and remains in this state as the stress

decays down to 0 MPa (Figure 3c). A compressive stress of -60 MPa is subsequently applied to

the nanomagnet in a similar manner but it does not nudge the system out of the vortex state (Figure

3d) and finally after stress is removed, the vortex state continues to persist (Figure 3e). This state

is non-volatile.

References

Ahmad, H., Atulasimha, J. and Bandyopadhyay, S. (2015)" Electric field control of magnetic states in isolated and dipole-coupled FeGa nanomagnets delineated on a PMN-PT substrate." *Nanotechnology,* 26, 401001.

Alam, M. T., Siddiq, M. J., Bernstein, G. H., Niemier, M. T., Porod, W. and Hu, X. S. (2010) "On-chip clocking for nanomagnet logic devices," *Nanotechnology, IEEE Transactions on*. IEEE, 9(3), pp. 348–351.

Allwood, D. A., Xiong, G., Faulkner, C. C., Atkinson, D., Petit, D. and Cowburn, R. P. (2005) "Magnetic domain-wall logic", *Science (New York, N.Y.)*, 309(5741), pp. 1688–92.

Atulasimha, J. and Bandyopadhyay, S. (2010) "Bennett clocking of nanomagnetic logic using multiferroic single-domain nanomagnets," *Applied Physics Letters*, 97, p. 173105.

Atulasimha, J. and Bandyopadhyay, S. (2012) "An energy-efficient Bennett clocking scheme for 4-state multiferroic logic," *Nanotechnology, IEEE Transactions on*, 11(2), pp. 418–425.

Bandyopadhyay, S. (2005a) "Computing with spins: from classical to quantum computing," *Superlattices and Microstructures*, 37(2), pp. 77–86.

Bandyopadhyay, S. (2005b) "Computing with spins: from classical to quantum computing," *Superlattices and Microstructures*, 37(2), pp. 77–86.

Bandyopadhyay, S. and Cahay, M. (2009) "Electron spin for classical information processing: a brief survey of spin-based logic devices, gates and circuits," *Nanotechnology*, 20(41), p. 412001.

Bandyopadhyay, S., Das, B. and Miller, a E. (1994) "Supercomputing with spin-polarized single electrons in a quantum coupled architecture," *Nanotechnology*, 5(2), pp. 113–133.

Bandyopadhyay, S. and Roychowdhury, V. (1996) "Computational Paradigms in Nanoelectronics: Quantum Coupled Single Electron Logic and Neuromorphic Networks," *Japanese Journal of Applied Physics*, 35(Part 1, No. 6A), pp. 3350–3362.

Bandyopadhyay, S., Svizhenko, A. and Stroscio, M. A. (2000) "Why would anyone want to build a narrow channel (quantum wire) transistor?," *Superlattices and Microstructures*, 27(2-3), pp. 67–76.

Behin-Aein, B., Salahuddin, S. and Datta, S. (2009) "Switching energy of ferromagnetic logic bits," *Nanotechnology, IEEE Transactions on*. IEEE, 8(4), pp. 505–514.

Bennett, C. H. (1982) "The thermodynamics of computation—a review," *International Journal of Theoretical Physics*. Springer, 21(12), pp. 905–940.

Bhowmik, D., You, L. and Salahuddin, S. (2014) "Spin Hall effect clocking of nanomagnetic logic without a magnetic field.," *Nature nanotechnology*. Nature Publishing Group, 9(1), pp. 59–63.

Biswas, A. K., Bandyopadhyay, S. and Atulasimha, J. (2013) "Acoustically assisted spin-transfer-torque switching of nanomagnets: An energy-efficient hybrid writing scheme for non-volatile memory" *Appl. Phys. Lett.,* 103, p. 232401.

Biswas, A. K., Bandyopadhyay, S. and Atulasimha, J. (2014) "Complete magnetization reversal in a magnetostrictive nanomagnet with voltage-generated stress: A reliable energy-efficient non-volatile magneto-elastic memory" *Appl. Phys. Lett.,* 105, p. 072408.

Bombeck, M., Salasyuk, A.S. , Glavin, B. A., Scherbakov, A. V. , Brüggemann, C. , Yakovlev, D. R. , Sapega, V. F., Liu, X., Furdyna, J. K., Akimov, A. V. and Bayer, M.(2012)" Excitation of spin waves in ferromagnetic (Ga,Mn)As layers by picosecond strain pulses" *Phys. Rev. B*, 85, p.195324

Boyd, E. (1960) "Magnetic anisotropy in single-crystal thin films," *IBM Journal of Research and Development*, (April), pp. 116–129.

Bozorth,R. M. (1993) *Ferromagnetism*. Wiley, p. 968.

Brintlinger, T., Lim, S.-H., Baloch, K. H., Alexander, P., Qi, Y., Barry, J., Melngailis, J., Salamanca-Riba, L., Takeuchi, I. and Cumings, J. (2010) "In situ observation of reversible nanomagnetic switching induced by electric fields.," *Nano letters*, 10(4), pp. 1219–23.

Carlton, D., Emley, N., Tuchfeld, E. and Bokor, J. (2008) "Simulation Studies of Nanomagnet-Based Logic Architecture," *Nano Letters*, 8(12), pp. 4173–4178.

Chen, K.-P., Zhang, X.-W. and Luo, H.-S. (2002) "Electric-field-induced phase transition in <001>-oriented Pb(Mg 1/3 Nb 2/3)O3 -PbTiO 3 single crystals," *Journal of Physics: Condensed Matter*, 14(29), pp. L571–L576.

Chikazumi, S. (1964) *Physics of Magnetism*, *John Wiley Sons New York Chichester Weinheim Brisbane Singapore Toronto*. John Wiley & Sons, Inc., Hoboken, New Jersey, p. 554.

Chow, P. P. (1991) "Molecular Beam Epitaxy," in Vossen, J. L. and Kern, W. (eds) *Thin film processes II*. Boston: Academic Press.

Chu, Y.-H., Martin, L. W., Holcomb, M. B., Gajek, M., Han, S.-J., He, Q., Balke, N., Yang, C.-H., Lee, D., Hu, W., Zhan, Q., Yang, P.-L., Fraile-Rodríguez, A., Scholl, A., Wang, S. X. and Ramesh, R. (2008) "Electric-field control of local ferromagnetism using a magnetoelectric multiferroic.," *Nature materials*, 7(6), pp. 478–82.

Chung, T.-K., Keller, S. and Carman, G. P. (2009) "Electric-field-induced reversible magnetic single-domain evolution in a magnetoelectric thin film," *Applied Physics Letters*, 94(13), p. 132501.

Clark, A.E., Hathaway, K.B., M. Wun-Fogle, Restorff, J.B., Lograsso, T.A., Keppens, V.M. Petculescu, G. Taylor R.A., (2003), *J. Appl. Phys.,* 93, p. 8621.

Cowburn, R. P., Ercole, a., Gray, S. J. and Bland, J. a. C. (1997) "A new technique for measuring magnetic anisotropies in thin and ultrathin films by magneto-optics," *Journal of Applied Physics*, 81(10), p. 6879.

Cowburn, R. P., Koltsov, D. K., Adeyeye, A. O. and Welland, M. E. (1999) "Designing nanostructured magnetic materials by symmetry," *Europhysics Letters (EPL)*, 48(2), pp. 221–227.

Cowburn, R. P., Koltsov, D. K., Adeyeye, A. O., Welland, M. E. and Tricker, D. M. (1999) "Single-Domain Circular Nanomagnets." *Phys.Rev.Lett.*, 83(5), pp. 1042–1045.

Cowburn, R. P. and Welland, M. E. (2000) "Room Temperature Magnetic Quantum Cellular Automata," *Science*, 287(5457), pp. 1466–1468.

Csaba, G., Imre, A., Bernstein, G. H., Porod, W. and Metlushko, V. (2002) "Nanocomputing by field-coupled nanomagnets," *IEEE Transactions on Nanotechnology*, 1(4), pp. 209–213.

Cui, J., Hockel, J. L., Nordeen, P. K., Pisani, D. M., Liang, C., Carman, G. P. and Lynch, C. S. (2013) "A method to control magnetism in individual strain-mediated magnetoelectric islands," *Applied Physics Letters*, 103(23), p. 232905.

Cullity, B. D. and Graham, C. D. (2009) *Introduction to Magnetic Materials*. Wiley.

Datta,S.(1986) *Surface Acoustic wave devices; Prentice-Hall*.

D'Souza, N. (2014). *Applications of 4-state nanomagnetic logic using multiferroic nanomagnets possessing biaxial magnetocrystalline anisotropy and experiments on 2-state multiferroic nanomagnetic logic.*

D'Souza, N., Atulasimha, J. and Bandyopadhyay, S. (2011) "Four-state nanomagnetic logic using multiferroics," *Journal of Physics D: Applied Physics*, 44(26), p. 265001.

D'Souza, N., Atulasimha, J. and Bandyopadhyay, S. (2012b) "An ultrafast image recovery and recognition system implemented with nanomagnets possessing biaxial magnetocrystalline anisotropy," *Nanotechnology, IEEE Transactions on*, 11(5), pp. 896–901.

D'Souza, N., Fashami, M. S., Bandyopadhyay, S. and Atulasimha, J. (2016) "Experimental Clocking of Nanomagnets with Strain for Ultra Low Power Boolean Logic" *Nano Letters 16 (2)*, 1069–1075

Davis, S. baruth, A. and Adenwalla, S. (2010). "Magnetization dynamics triggered by surface acoustic waves" *Appl. Phys. Lett.*, 105, p.072408.

Davis, W. R., Wilson, J., Mick, S., Mineo, C., Sule, A. M., Steer, M. and Franzon, P. D.

(2005) "Demystifying 3D ICs: The Pros and Cons of Going Vertical," *IEEE Design and Test of Computers*, 22(6), pp. 498–510.

Dusch, Y., Tiercelin, N., Klimov, A., Giordano, S., Preobrazhensky, V. and Pernod, P. (2013) "Stress-mediated magnetoelectric memory effect with uni-axial TbCo2/FeCo multilayer on 011-cut PMN-PT ferroelectric relaxor," *Journal of Applied Physics*, 113(17), p. 17C719.

Dyakonov, M. I. and Perel, V. I. (1971) "Current-induced spin orientation of electrons in semiconductors," *Physics Letters A*, 35(6), pp. 459–460.

Eerenstein, W., Mathur, N. D. and Scott, J. F. (2006) "Multiferroic and magnetoelectric materials.," *Nature*, 442(7104), pp. 759–65.

Emley, N. C., Albert, F. J., Ryan, E. M., Krivorotov, I. N., Ralph, D. C., Buhrman, R. a., Daughton, J. M. and Jander, a. (2004) "Reduction of spin transfer by synthetic antiferromagnets," *Applied Physics Letters*, 84(21), p. 4257.

Farle, M. (1998) " Ferromagnetic resonance of ultrathin metallic layers", *Rep. prog. Phys.,* 61, 755-826

Fukami, S., Suzuki, T., Nagahara, K., Ohshima, N., Ozaki, Y., Saito, S., Nebashi, R., Sakimura, N., Honjo, H., Mori, K., Igarashi, C., Miura, S., Ishiwata, N. and Sugibayashi, T. (2009) "Low-current perpendicular domain wall motion cell for scalable high-speed MRAM," pp. 230–231.

Geddes, L. A. (1990) "Historical highlights in cardiac pacing.," *IEEE engineering in medicine and biology magazine : the qua te ly magazine of the Enginee ing in Medicine & Biology Society*, 9(2), pp. 12–8.

Gopman, D. B., Lau, J. W., Mohanchandra, K. P., Wetzlar, K. and Carman, G. P.(2016) "Determination of the exchange constant of Tb0.3Dy0.7Fe2 by broadband ferromagnetic resonance spectroscopy" *Phys. Rev. B,* 93, 064425

Griffiths J-H-E (1946)"Anomalous High-frequency Resistance of Ferromagnetic Metals" *Nature,* 158**,** 670

Hockel, J. L., Bur, A., Wu, T., Wetzlar, K. P. and Carman, G. P. (2012) "Electric field induced magnetization rotation in patterned Ni ring/Pb(Mg1/3Nb2/3)O3 (1−0.32)- PbTiO3 0.32 heterostructures," *Applied Physics Letters*. American Institute of Physics, 100(2), p. 022401.

Imre, A., Csaba, G., Ji, L., Orlov, A., Bernstein, G. H. and Porod, W. (2006) "Majority logic gate for magnetic quantum-dot cellular automata." *Science (New York, N.Y.)*, 311(5758), pp. 205–8.

International Technology Roadmap for Semiconductors (n.d.). Available from: <www.itrs.com>.

Janušonis, J. Chang, C. L., Loosdrecht P. H. M. V. and Tobey, R. I.(2015)." Frequency tunable surface magneto elastic waves" *Appl. Phys. Lett.*, 106, p.181601.

Kajiwara, Y., Harii, K., Takahashi, S., Ohe, J., Uchida, K., Mizuguchi, M., Umezawa, H., Kawai, H., Ando, K., Takanashi, K., Maekawa, S. and Saitoh, E. (2010) "Transmission of electrical signals by spin-wave interconversion in a magnetic insulator.," *Nature*. Nature Publishing Group, 464(7286), pp. 262–6.

Kawai, N. and Kawahito, S. (2004) "Noise analysis of high-gain, low-noise column readout circuits for CMOS image sensors," *Electron Devices, IEEE Transactions on*. IEEE, 51(2), pp. 185–194.

Kelly, J. and Leonard, M. (1997) "Effect of Composition on the Electromechanical Properties of (1-x) Pb (Mg1/3Nb2/3) O3− XPbTiO3 Ceramics," *Journal of the American Ceramic Society*, 80(4), pp. 957–964.

Kim, J.-W., Vomir, M. and Bigot, J.-Y.(2012) "Ultrafast Magnetoacoustics in Nickel Films "*Phys. Rev. Lett.*, 109, 166601

Kittel, C. (1947) "Interpretation of anomalous Larmor frequencies in ferromagnetic Resonance experiments"*Phys. Rev.,* 71, 270

Kittel, C. (1948) "On the Theory of Ferromagnetic Resonance Absorption" *Phys. Rev.,* 73, 155.

Kovalenko, O., Pezeril, Th. and Temnov, V. V. (2013)" New Concept for Magnetization Switching by Ultrafast Acoustic Pulses" *Physical Review letters*, 110, p. 266602.

Lambson, B., Gu, Z., Monroe, M., Dhuey, S., Scholl, A. and Bokor, J. (2013) "Concave nanomagnets: investigation of anisotropy properties and applications to nanomagnetic logic," *Applied Physics A*, 111(2), pp. 413–421.

Lee, E. W. (1955) "Magnetostriction and Magnetomechanical Effects," *Reports on Progress in Physics*, p. 184.

Lee, F. (1968) "Shape-induced biaxial anisotropy in thin magnetic films," *IEEE Transactions on Magnetics*, 4(3), pp. 502–506.

Lei, N., Devolder, T., Agnus, G., Aubert, P., Daniel, L., Kim, J.-V., Zhao, W., Trypiniotis, T., Cowburn, R. P., Chappert, C., Ravelosona, D. and Lecoeur, P. (2013) "Strain- controlled

magnetic domain wall propagation in hybrid piezoelectric/ferromagnetic structures.," *Nature communications*, 4, p. 1378.

Lisca, M., Pintilie, L., Alexe, M. and Teodorescu, C. (2006) "Thickness effect in Pb(Zr0.2Ti0.8)O3 ferroelectric thin films grown by pulsed laser deposition," *Applied Surface Science*, 252(13), pp. 4549–4552.

Liu, L., Pai, C.-F., Li, Y., Tseng, H. W., Ralph, D. C. and Buhrman, R. A. (2012) "Spin-torque switching with the giant spin Hall effect of tantalum.," *Science (New York, N.Y.)*, 336(6081), pp. 555–8.

Microchem (n.d.) "NANO PMMA and Copolymer^TM," Available from: < http://microchem.com/pdf/PMMA_Data_Sheet.pdf>.

Parkin, S.S.P., Masamitsu, H., Thomas, L. "Magnetic Domain-Wall Racetrack Memory" *Science*, 320 (5873), pp.190-194

Parkes, D.E., Shelford, L.R., Wadley, P., Holy, V., Wang, M., Hindmarch, A.T., van der Laan, G., Campion, R.P., Edmonds, K.W. Cavill, S.A. and Rushforth, A.W. (2013). "Magnetostrictive thin films for microwave spintronics." *Sci. Rep.,* 3, p. 2220

Pertsev, N. and Kohlstedt, H. (2010) "Resistive switching via the converse magnetoelectric effect in ferromagnetic multilayers on ferroelectric substrates.," *Nanotechnology*, 21(47), p. 475202.

Pertsev, N. and Kohlstedt, H. (2009) "Magnetic tunnel junction on a ferroelectric substrate," *Applied Physics Letters*, 95(16), p. 163503.

Ralph, D. C. and Stiles, M. (2007) "Spin transfer torques," *Journal of Magnetism and Magnetic Materials*, 320, pp. 1190–1216.

Roy, K., Bandyopadhyay, S. and Atulasimha, J. (2011a) "Hybrid spintronics and straintronics: A magnetic technology for ultra low energy computing and signal processing," *Applied Physics Letters*. AIP, 99(6), p. 063108.

Roy, K., Bandyopadhyay, S. and Atulasimha, J. (2012) "Energy dissipation and switching delay in stress-induced switching of multiferroic nanomagnets in the presence of thermal fluctuations," *Journal of Applied Physics*. American Institute of Physics, 112(2), p. 023914.

Roy, K., Bandyopadhyay, S. and Atulasimha, J. (2011b) "Switching dynamics of a magnetostrictive single-domain nanomagnet subjected to stress," *Physical Review B*, 83(22), pp. 1–15.

Roychowdhury, V., Janes, D., Bandyopadhyay, S. and Wang, X. (2002) "Collective computational activity in self-assembled arrays of quantum dots: a novel neuromorphic

architecture for nanoelectronics," *Electron Devices, IEEE Transactions on*. IEEE, 43(10), pp. 1688–1699.

Salahuddin, S. and Datta, S. (2007) "Interacting systems for self-correcting low power switching," *Applied Physics Letters*, 90(9), p. 093503.

Salehi Fashami, M. (2014) *Multiferroic nanomagnetic Logic: Hybrid Spintronics-straintronic paradigm for ultra low energy computing.*

Salehi Fashami, M., Atulasimha, J. and Bandyopadhyay, S. (2012) "Magnetization dynamics, throughput and energy dissipation in a universal multiferroic nanomagnetic logic gate with fan-in and fan-out.," *Nanotechnology*, 23(10), p. 105201.

Salehi Fashami, M., Atulasimha, J. and Bandyopadhyay, S. (2013) "Energy dissipation and error probability in fault-tolerant binary switching.," *Scientific reports*. Nature Publishing Group, 3, p. 3204.

Salehi Fashami, M. and D'Souza, N. (2014) "Implementation of 4-state nanomagnetic devices with shape anisotropy," 11(2), pp. 3–4.

Salehi Fashami, M., Roy, K., Atulasimha, J. and Bandyopadhyay, S. (2011) "Magnetization dynamics, Bennett clocking and associated energy dissipation in multiferroic logic.," *Nanotechnology*, 22(15), p. 155201.

Schoen, M. A. W., Shaw J.M., Nembach H.T., Weiler M. and Silva, T.J.(2015)" Radiative damping in waveguide-based ferromagnetic resonance measured via analysis of perpendicular standing spin waves in sputtered permalloy films" *Physical Review B,* 92, 184417.

Siegle, W. T. (1965) "Exchange Coupling of Uniaxial Magnetic Thin Films," *Journal of Applied Physics*, 36(3), p. 1116.

Slonczewski, J. (1996) "Current-driven excitation of magnetic multilayers," *Journal of Magnetism and Magnetic Materials*, 159(1-2), p. L1 <last_page> L7.

Spedalieri, F. M., Jacob, A. P., Nikonov, D. E. and Roychowdhury, V. (2011) "Performance of Magnetic Quantum Cellular Automata and Limitations Due to Thermal Noise," *IEEE Transactions on Nanotechnology*, 10(3), pp. 537–546.

Tacchi,S., Fin, S., Carlotti, G., Gubbiotti, G., Madami, M., Barturen, M., Drief, M., Bisero, D., Rettori A. and Pini, M.G. (2014) "Rotatable magnetic anisotropy in a $Fe_{0.8}Ga_{0.2}$ thin film with stripe domains: Dynamics versus statics" *Phys. Rev. B*, 89, p. 024411

Thevenard, L., Duquesne, J.-Y., Peronne, E., von Bardeleben, H. J., Jaffres, H., Ruttala, S., George, J-M. Lemaître, A. and Gourdon, C. (2013) "Irreversible magnetization switching using surface acoustic waves" *Phys. Rev. B,* 87, p.144402.

Weiler, M., Dreher, L., Heeg, C., Huebl, H. Gross, R. Brandt, M.S. and Goennenwein, S.T.B. (2011) "Elastically Driven Ferromagnetic Resonance in Nickel Thin Films"*Physical Review Letters,* 106, p.11701

Xiuming, L., Zhang R., Huang, N., Lu, T. and Cao,W.(2009)." Surface acoustic wave propagation properties in $0.67Pb(Mg_{1/3}Nb_{2/3})O_3$-$0.33PbTiO_3$ single crystal poled along $[111]_c$" *App. Phys. Lett.*, 95, p. 242906.

<u>VITA</u>

PERSONAL INFORMATION

Name: Vimal G. Sampath

Date of Birth: April 12, 1988

Place of Birth: India

Citizenship: Indian

EDUCATION

Ph.D., Virginia Commonwealth University, Richmond, VA
Department of Mechanical and Nuclear Engineering, December 2016
Thesis Advisor: Jayasimha Atulasimha, Ph.D.

Master of Technology, Indian Institute of Technology, Kharagpur, India
Department of Aerospace Engineering, May 2011
Thesis Topic: Experimental demonstration of autonomous attitude control of a fixed wing aircraft.
GPA: 8.19/10.00

Bachelor of Technology, Indian Institute of Technology, Kharagpur, India
Department Of Aerospace Engineering, May 2010
GPA: 8.19/10.00

WORK/RESEARCH EXPERIENCE

Graduate Research and Teaching Assistant, Mentor: Jayasimha Atulasimha, Ph.D., 2012 – 2016
Department of Mechanical and Nuclear Engineering, Virginia Commonwealth University.

Deputy Manager, Product development, Aug 2011- Jan 2012

Ashok Leyland Ltd., Chennai, India

HONORS AND AWARDS

1. Won the Outstanding Graduate Teaching Assistant award in 2013-2014, School of Engineering, VCU

2. Won 1st position in Mahindra Satyam Sponsored "Aerospace Young Engineers" Awards 2010.

PUBLICATIONS

1. **V Sampath**, N D'Souza, D Bhattacharya, G M Atkinson, S Bandyopadhyay and J Atulasimha. "Acoustic-Wave-Induced Magnetization Switching of Magnetostrictive Nanomagnets from Single-Domain to Nonvolatile Vortex States." Vimal Sampath *et. al.*, **Nano Letters 16(9)**, 5681-5687(2016).(http://pubs.acs.org/doi/abs/10.1021/acs.nanolett.6b02342)

2. **V Sampath**, N D'Souza, G M Atkinson, S Bandyopadhyay and J Atulasimha. "Experimental demonstration of acoustic wave induced magnetization switching of dipole coupled magnetostrictive nanomagnets for ultralow power computing." **Applied Phys. Lett**. **109**, 102403 (2016). (http://dx.doi.org/10.1063/1.4962335).

CONFERENCE PROCEEDINGS AND TALKS

1. **V Sampath**, D Bhattacharya, N D'Souza, S Bandyopadhyay and J Atulasimha. "Experimental manipulation of magnetic states of magnetostrictive nanomagnets using surface acoustic waves" at American Physical Society, March 2016, Baltimore, MD, USA. (Talk and Abstract only)

2. D Bhattacharya, MM Al-Rashid, **V Sampath**, N D'Souza, S Bandyopadhyay and J Atulasimha. "Incoherent stress-mediated magnetization reversal in shape anisotropic multiferroic nanomagnets" American Physical Society, March 2016, Baltimore, MD, USA. (Talk and Abstract only, Co-Author)

3. **V Sampath**, N D'Souza, S Bandyopadhyay and J Atulasimha. "Preliminary experiments on SAW based magnetization switching of Nano magnets" at American Physical Society, March 2015, San Antonio, TX, USA. (Talk and Abstract only)

4. T Mandal, **V Sampath**, H Shukla and M Sinha. "Development and Testing of Atmega128 based Autopilot" in 24th National Convention of Aerospace Engineers and National Seminar on " New vistas in Aviation and Aerospace", Nov. 2010 at The institution of Engineers(India) Jaipur. (Talk only, Co-Author).

LEADERSHIP POSITIONS

1. Graduate Mechanical and Nuclear Engineers, VCU- Vice President (Apr' 13- June '14).

2. Laws of Motion, Kshitij-The largest Engineering students Technology meetup in India, IIT Kharagpur- Technology Head (July 2008- May 2009)

EDUCATIONAL OUTREACH

1. Organized 'Building Logic with Nanomagnets' workshop as part of the MathScience Innovation Center (MSiC) Grades 6-8 Student Conference, December 2012 (MSiC).

2. Mentored high school student as part of the Richmond Area Program for Minorities in Engineering (RAPME), June – August, 2013 and June- August 2014.